FROM RHYOLITE TO BASALT AND CONDUIT FLOW TO LAVA FLOW: HOW GOOD ARE OUR MODELS?

A DISSERTATION SUBMITTED TO THE GRADUATE DIVISION OF THE UNIVERSITY OF HAWAIʻI AT MĀNOA IN PARTIAL FULFILLMENT OF THE REQUIREMENTS FOR THE DEGREE OF

DOCTOR OF PHILOSOPHY

IN

GEOLOGY AND GEOPHYSICS

August 2021

By

Rebecca Lynn deGraffenried

Dissertation Committee:

Thomas Shea, Chairperson
Julia Hammer
Scott Rowland
Bruce Houghton
John Allen

Acknowledgements

This dissertation represents a labor of love, and sometimes pain, over the past four years. Without the help of numerous people, I would not have been able to persevere and be as successful as I have. First and foremost, I would like to thank my family, both immediate and extended, for all the love and support. From the time I was a four-year-old child saying I wanted to be a volcanologist until now, when I finally feel like I can call myself a volcanologist, they have always believed in me and accepted that hiking with me means stopping and looking at rocks every 15 minutes. Not all family is blood related, and there are many people who have supported me on this doctorate journey that fall into this category. My interest in bubbles in magma was foretold by some of these family friends, who gave me the nickname "Bubbles" for always blowing bubbles while waiting for someone to play with me. Without all of these people as cheerleaders for me, my journey towards becoming a volcanologist would have been much less fun.

On the science side of things, I have many people to thank for their insight and guidance. My coauthors on the various chapters, Nicolas Cluzel, Hannah Dietterich, Ryan Perroy, and Matt Patrick, have all been invaluable resources from whom I have learned a tremendous amount. In particular, I have to thank Nicolas for being an excellent host when I visited France for a month. Every single person has offered so much of their time and expertise, and I feel like I have become a better researcher through their insights. My committee members, Scott, Bruce, and John, have given a tremendous amount of time towards helping me, between all of the committee meetings and the various extra meetings to discuss concepts. They have always had encouragement and helpful comments that have helped build the various projects into a cohesive dissertation. I am so incredibly grateful for all of their contributions. Finally, I would like to

thank Alexander Marshall for his help with image processing in Chapter 4. The task was a large one, so his help was invaluable to move things forward at a reasonable rate.

Staying sane is a challenging task through graduate school, but I have had the great fortune of excellent friends to help me through the difficult times. Everyone that has been part of the magma chamber, both past and present, has been incredibly supportive and friendly. Of course, the majority of the support has come from the other people in Volcano Team Awesome. All of the time spent playing games, getting food, and chatting the time away has been an absolute life saver.

Last, but certainly not least, I have an immense amount of gratitude for my advisors, Tom and Julia. I could spend three additional pages just listing all of the things that they have done for me in the past four years. They have given me so much of their time and help. No matter how busy they were with their own work, if I had a problem, they would find time to help me. I could be confident and bold in all of my work because I knew if I ran into any stumbling blocks, I could ask for advice and bounce ideas off of them for solutions. Each of their different styles of advising has given me different tools in my researcher belt. Beyond the science aspect of advising, they also helped build a fun and inviting lab group. The social aspect of everything was just as important for my success. I feel like a capable scientist now because of all their guidance.

The work within this dissertation was funded by grants from the National Science Foundation, the Ian S.E. Carmichael award from the Geological Society of America, the Fred M. Bullard Endowed Graduate Fellowship, and the Donald Swanson Graduate Research Fellowship.

Abstract

Volcanic eruptions impact human lives in a multitude of ways, mainly dependent on eruption intensity and style. Broadly speaking, powerfully explosive eruptions produce large plumes of ash and pyroclastic density currents, whereas effusive to weakly explosive eruptions can produce scoria cones and ramparts, as well as lava domes and flows, depending on the fluidity of the lava. On either end of this explosivity spectrum, unique hazards exist that disaster management agencies must mitigate to keep nearby populations safe. As our understanding of volcanic eruptions and their underlying processes has been refined, our ability to forecast volcanic hazards has begun to improve. In this dissertation, I examine two key processes that are used to forecast impacts of volcanic eruptions: magma decompression and lava flow propagation. Magma decompression rate is a critical parameter that influences whether a magma will erupt explosively, and thus it requires accurate determination. A new, promising technique to calculate magma decompression rate utilizes small pockets of magma trapped within crystals that remained open to the host magma, called melt embayments. These embayments develop concentration gradients in dissolved volatiles (e.g., H_2O, CO_2) during decompression that can be measured. Assuming the concentration gradients are formed purely through diffusive loss of the volatiles from the embayment to the host magma, the decompression timescale (and by extension decompression rate) that the embayments experienced can be calculated. This technique is gaining use due to its relative ease of implementation, the prevalence of embayments, and the wide range of decompression rates that can be resolved, provided an appropriate diffusing volatile species is present and measured. However, this technique has not undergone any testing to verify that the current modeling standard is not introducing its own error. Therefore, I quantify the amount of error introduced into calculated timescales by modeling simplifications

numerically. Other decompression rate meters can be used in conjunction with diffusion modeling to quantify the range of decompression rates during the course of a volcanic eruption. However, this is a relatively new approach, so I conduct decompression experiments that use two decompression rate meters in the same experimental charge to evaluate whether these meters are compatible with each other. Additionally, the experiments provide insights into the assumptions needed to recover a known decompression rate. Once lava erupts on the surface, it can produce lava flows that are destructive to nearby communities, as in the 2018 eruption of Kīlauea, HI. Forecasting the path and velocity of lava flows is a crucial step to issue accurate warnings and implement effective evacuations. The 2018 Kīlauea eruption is an excellent natural laboratory to test previous forecasting methods as the data on the flows is exceptional in its temporal resolution, with daily overflights by the response team with both helicopters and drones, as well as daily overflights by commercial photographers. I utilize equations from two complimentary studies that predict lava flow length through time by calculating the evolution of various lava properties that serve to slow the flow. This study focuses on three flows during the eruption that span a range of lava composition, crystallinity, and duration to test the applicability of equations that require limited *a priori* knowledge of flow conditions. Altogether, this dissertation provides new insights to implementation of simulations of volcanic processes that will aid future modelers.

Table of Contents

List of Tables

List of Figures

Chapter 1. Introduction

Volcanic eruptions present various health and socioeconomic hazards to humans, and these hazards scale with the size and intensity of the eruption. High-silica magmas (e.g., rhyolites and dacites) tend to erupt more explosively, as during the 1980 eruption of Mt. St. Helens, WA (Cashman and Sparks, 2013). Powerful explosive eruptions involve viscous magma and produce ash columns that can impact large areas with pyroclast fallout, as well as deadly pyroclastic density currents that can inundate areas nearby the volcano (Cashman and Sparks, 2013). Low silica magmas are more fluid and often erupt effusively to weakly explosively, such as the eruptions that have occurred at Kīlauea Volcano (Hawai‘i) over the last 200 years. These eruptions tend to produce lava flows that can destroy homes and livelihoods (Cashman and Sparks, 2013; Houghton et al., 2021b). Although the hazards from these eruption styles are different, they can have devastating impacts, and it is critical to understand the factors that contribute to the style and destructiveness of eruptions in order to minimize their societal impacts.

1.1 High silica magmas

Magma degassing plays a fundamental role in determining the ultimate eruption style of high silica magmas. The magma degassing process begins as magma begins rising towards the surface. At a certain point, the magma becomes supersaturated in a volatile phase (e.g., H_2O, CO_2) and the excess volatiles are exsolved into a separate vapor/gas phase (Fig. 1.1). Bubble nucleation can be aided by the presence of crystals (i.e., heterogeneous nucleation), particularly Fe-Ti oxides (e.g., Hurwitz and Navon, 1994). The degree of supersaturation needed to nucleate the vapor bubbles (ΔP_N) depends directly on the style of nucleation. Homogeneous nucleation (i.e., nucleation without the aid of crystals) ΔP_N was experimentally determined to occur at

~100-150 MPa (e.g., Mangan and Sisson, 2000; Mourtada-Bonnefoi and Laporte, 1999; 2004), and heterogeneous nucleation ΔP_N ranges from <25 MPa (Fe-Ti oxides; Hurwitz and Navon, 1994) to ~100 MPa (feldspar; Hurwitz and Navon, 1994; Shea, 2017). Early investigations of high silica magmas suggested that bubble nucleation must occur predominantly homogeneously due to the low number density of Fe-Ti oxides and high bubble number density in many rhyolites (e.g., Mangan et al., 2004). Indeed, a late-stage homogeneous nucleation event has been thought to be a major driver for the explosivity of erupted rhyolitic magmas (e.g., Mangan and Sisson, 2000). However, this interpretation has been challenged recently; Shea (2017) suggests that the low number density of Fe-Ti oxides observed in rhyolites is due to primarily sectioning effects and the small size of most Fe-Ti oxides. This hypothesis has been supported by recent experimental studies (e.g., Caceres et al., 2020), detailed measurements of rhyolite glass with

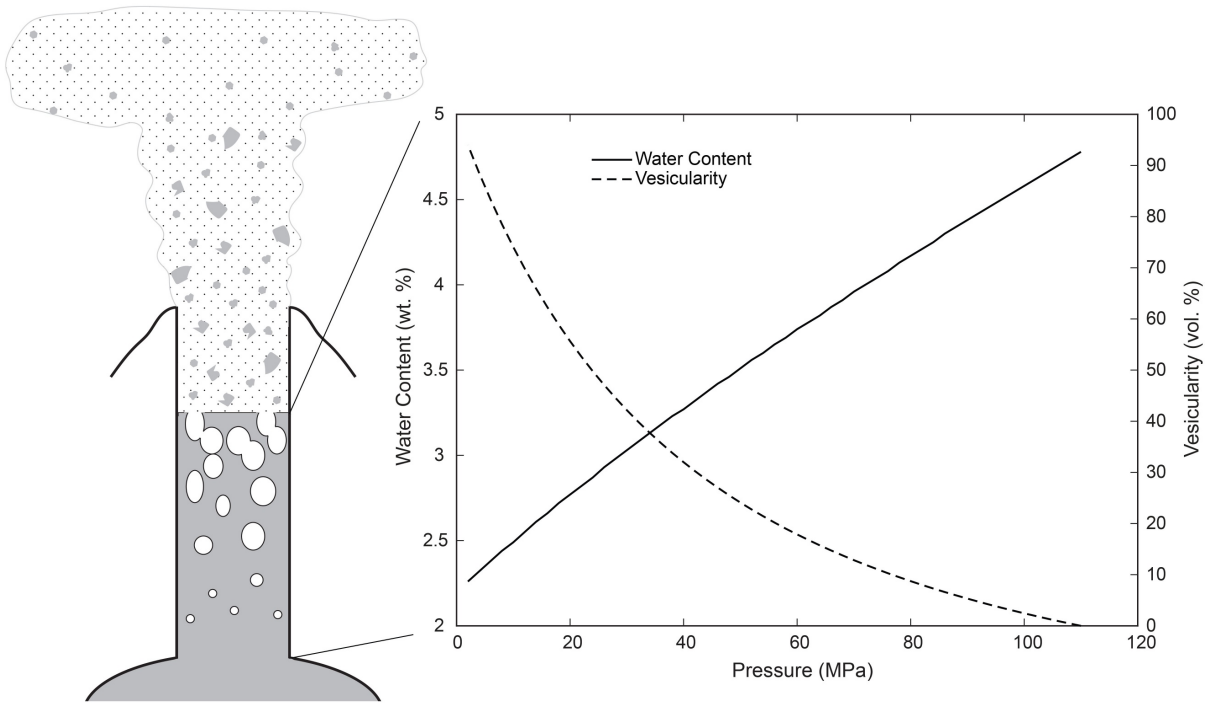

Figure 1.1. Schematic representation of changes to bulk magma vesicularity and dissolved water content during decompression and ascent of a rhyolite magma. Vesicularity increases rapidly at lower pressure, which accelerates the magma up the conduit. The vesicularity-water content relationship is calculated using the solubility relationship of Moore et al. (1998) and vesicularity model of Gardner et al. (1999), with parameters relevant to Inyo Domes, CA, outlined in deGraffenried et al. (2019)

Raman spectroscopy (e.g., Di Genova et al., 2018; 2020), and numerical studies of bubble nucleation (e.g., Hajimirza et al., 2021). Thus, it is possible that bubble nucleation predominantly occurs heterogeneously, rather than homogenously, in rhyolitic magmas.

Regardless of nucleation style, once bubbles are nucleated, continued decompression drives bubble growth through diffusive addition of volatiles and decompression-induced gas expansion (Gonnermann and Manga, 2007). Once bubbles grow large enough, they begin to impinge on one another and coalesce. Through coalescence, bubbles may create interconnected pathways along which vapor can travel and escape the system, thus relieving gas pressure that would otherwise drive explosive eruptions. Coalescence can be promoted by shearing, particularly near the conduit walls (e.g., Okumura et al., 2006; 2008), or the presence of crystals (e.g., Lindoo et al., 2017; deGraffenried et al., 2019; Colombier et al., 2020). The balance between volatile exsolution from the melt (i.e., degassing) and loss of exsolved gas from the system through permeable networks (i.e., outgassing) influences the explosivity of the associated eruption (Cassidy et al., 2018).

Magma decompression rate exerts a first-order control on magma degassing, and thus the explosivity of eruptions, as it determines the time available for degassing and outgassing. Additionally, other time-dependent reactions during decompression influence whether the magma fragments or not, such as decompression-induced crystallization of plagioclase microlites (e.g., Hammer and Rutherford, 2002). Faster decompression rates also are related to faster ascent rates, though decompression can also occur via a fragmentation wave propagating down the conduit, rather than upwards motion by the magma (e.g., Toramaru, 2006). In instances where decompression rate and ascent rate are directly correlated, however, fast decompression rates produce large strain rates on the magma, which promotes fragmentation (e.g., Webb and

Dingwell, 1990; Dingwell, 1996). Decompression rate is a critical parameter to better understand these other dependent processes and their influence on the explosive-effusive eruption transition.

1.2 Low silica magmas

Explosive Plinian to sub-Plinian eruptions are rare in low silica magmas, such as basalt, so the likely hazards associated with their eruptions are different. Instead, basaltic lavas tend to erupt in a weakly explosive manner that produces lava flows. Although lava flows are rarely hazardous to human life, fast moving lava flows can catch nearby communities unaware and result in casualties (e.g., Nyiragongo 2002 eruption; Komorowski et al., 2004). Most importantly, lava flows are immensely destructive to property and infrastructure that lie in their paths (e.g., Houghton et al., 2021b). Attempts to artificially divert lava flows in the past have had varying degrees of success (e.g., Lockwood and Torgerson, 1980; Williams and Moore, 1983; Barberi et al., 2003) but require significant resources and time to enact. Additionally, great care must be taken not to divert the lava flow to another populated area. Thus, the general course of action is just to evacuate anyone in the lava's path; any items that homeowners wish to save must be removed during evacuation. Timely and accurate evacuation orders require information on the path and velocity of lava flows, so many models have been developed to address these two key parameters.

Lava is a gravity current that follows the path of steepest descent (e.g., Favalli et al., 2005). Probabilistic models of lava flow path can be derived just using a digital elevation model (DEM) to determine the topography (e.g., SCIARA – Crisci et al., 2004; DOWNFLOW – Favalli et al., 2005). Varying degree of model complexity is available, with some iterations only taking into account the pre-existing topography (e.g., DOWNFLOW; Favalli et al., 2005) and others allowing for the effects of early emplaced lava (e.g., SCIARA; Crisci et al., 2004). Running

these types of models repeatedly produces a probability map of areas likely to be inundated by a lava flow of a given size originating from a given vent (Fig. 1.2b).

Lava flow velocity is more difficult to determine as it relies on a complex interplay between the evolution of lava material properties, lava supply rate, and the ground slope and roughness over which the lava is traveling (e.g., Griffiths, 2000). Lava material properties (e.g., viscosity, yield strength) are dependent on many factors, including melt composition, crystal content, bubble content, and temperature (e.g., Griffiths, 2000; Rust and Manga, 2002; Costa et al., 2009; Giordano et al., 2008; Mader et al., 2013). Even for these basic parameters, the influence of each on material properties is still an area of active study. For example, bubbles have a complex influence on

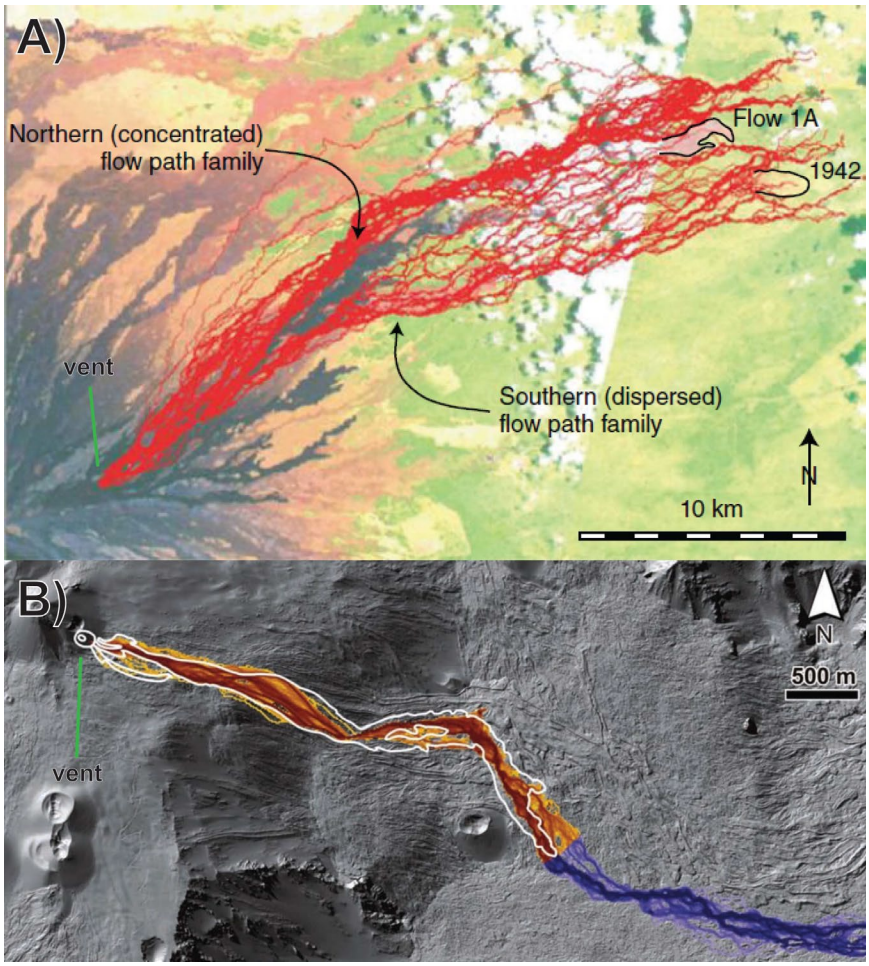

Figure 1.2. Examples of two lava flow simulations. A) Simulations that combine the thermo-rheologic calculations of FLOWGO (Harris and Rowland, 2012) with the DOWNFLOW (Favalli et al., 2005) path prediction for the 1984 eruption of Mauna Loa, HI. Each red line represents one simulation (*modified from Harris and Rowland, 2015*). B) Inundation probability forecasts for a flow from Mt. Etna, Italy using DOWNFLOW. Warmer colors indicate regions that are within the true length of the modeled flow (outlined in white) and cooler colors indicate forecasts greater than the length of the modeled flow. Darker colors within each family indicate higher probability of inundation (*modified from Favalli et al., 2011*).

viscosity that depends on their shape and size (e.g., Rust and Manga, 2002; Mader et al., 2013), though this relationship still requires clarification. Downflow cooling of lava promotes crystallization and potentially vesiculation, thereby increasing viscosity and yield strength and slowing the flow (e.g., Crisp and Baloga, 1994; Griffiths, 2000; Pistone et al., 2012; Harris and Rowland, 2015). High lava effusion rates promote longer lava flows and vice versa (e.g., Kauahikaua et al., 2003; Harris et al., 2007). However, lava effusion rate is rarely constant during an eruption and can fluctuate over timescales of minutes to days to months (e.g., Wadge, 1981; Harris et al., 2007; Bonny and Wright, 2017; Patrick et al., 2019). Recent work has started to show that the shortest timescale fluctuations in effusion rate can strongly influence flow behavior, particularly in channelized flows (e.g., Patrick et al., 2019). Effusion rate is often difficult to determine while the lava is actively flowing, but observations with unoccupied aircraft systems (UAS) can now constrain shorter timescale fluctuations in effusion rate (e.g., Patrick et al., 2019; Dietterich et al., 2021). Finally, the ground slope over which the lava flows also modulates its velocity, with steeper ground slope producing faster flows (e.g., Griffiths, 2000).

The feedbacks between changes in temperature and changes in lava properties can be incorporated in lava flow propagation models (Fig. 1.2a). Existing models include 1D simulations (e.g., FLOWGO – Harris and Rowland, 2015), 2D simulations (e.g., MAGFLOW – Vicari et al., 2007; VOLCFLOW – Kelfoun and Vargas, 2015), and more rarely, 3D simulations (e.g., LavaSIM – Hidaka et al., 2005; GPUSPH – Bilotta et al., 2015). Many of these models combine thermo-rheologic evolution of the lava with flow path prediction (Fig. 1.2a). Although 3D simulations can encompass a great deal of complexity that is present in nature, including depth and lateral variations in temperature and rheology, they require *a priori* knowledge of

many flow parameters and long computation times. 1D simulations cannot encompass the same range, but require less *a priori* knowledge of the flow and less computation time. Thus, the appropriate model for a given situation is dependent on the goal (e.g., Dietterich et al., 2017). 3D models are less useful in hazard forecast situations when information on the flow itself may be sparse, and 1D models cannot capture the full range of complexity that retrospective studies may require. The broad range of options for lava flow models offers researchers the appropriate tool for any given scenario, with new models being developed as our understanding of lava flows advances.

1.3 Outline of this dissertation

Although the two fundamental processes related to volcanic hazards outlined above (i.e., magma decompression and lava flow propagation) are present across all magma compositions, they play a different role for different magma compositions. In this dissertation, I examine the efficacy of two methods, one for calculating magma decompression rate and one for modeling lava flow propagation using both experimental and numerical approaches. Chapters 2 and 3 respectively cover a numerical and an experimental examination of petrologic techniques to calculate magma decompression rate. Chapter 4 covers a numerical application of sloping viscous theory to forecast lava flow propagation, with a natural example of the Kīlauea 2018 eruption. At the end of this dissertation, I summarize the conditions under which the two methods are the correct tools to choose, among the many available, and offer insights into the future of modeling these volcanological processes.

Chapter 2. Using Volatile Diffusion Profiles in Melt Embayments to Estimate Magma Decompression Rates: Assumptions and Inherited Errors

Published as: deGraffenried, R. & Shea, T. (2021). Using volatile diffusion profiles in melt embayments to estimate magma decompression rates: assumptions and inherited errors. *Geochemistry, Geophysics, Geosystems, 22*(5).

2.1 Abstract

Magma decompression rate has profound impacts on volcanic eruption style as it determines the time available for most kinetic processes (e.g., volatile exsolution, crystal nucleation and/or growth) that influence the explosive-effusive eruption transition. Thus, accurately quantifying decompression rate is a critical goal for understanding volcanic eruption dynamics. A recently developed technique uses crystal-hosted pockets of melt that remain open to the host magma (melt embayments) to calculate an average decompression rate. Diffusion of volatile elements (e.g., H_2O, CO_2) out of the embayment during decompression creates 'frozen' concentration gradients that can be modeled to calculate the time needed to create the gradients. This geospeedometer is increasingly used, but inherent assumptions associated with the modeling and their impact on calculated decompression rates are poorly quantified. Therefore, we have conducted a numerical investigation to assess the impact of three common model simplifications pertaining to rhyolitic magmas: 1D diffusion models, equilibrium degassing, and isothermal decompression. We find that the greatest deviation between imposed and calculated decompression rates occur when 1D models are applied to 'necked' embayments that have a constriction where the embayment joins with the far field melt. Simplifying to equilibrium degassing can also introduce modeling errors when disequilibrium conditions exist, though the prevalence of one or the other condition in nature is currently under debate. Assuming isothermal conditions introduces little error into modeled timescales. All of our modeling results are

summarized into a list of best practices to minimize error in modeled timescales due to modeling assumptions.

2.2 Introduction

Volcanic eruption style is modulated by the process of volatile (e.g., H_2O, CO_2) exsolution from ascending magma. Volatile exsolution efficiency strongly depends on composition, namely the degree of melt polymerization (e.g., Cassidy et al., 2018; Mangan et al., 2004). Highly polymerized melts, such as rhyolites, can inhibit volatile exsolution, a phenomenon typically not observed in less polymerized melts, such as basalts. However, kinetic processes can impact volatile exsolution and impact eruption style. For example, fast decompression rates can promote Plinian basaltic eruptions (e.g., Lloyd et al., 2014; Sable et al., 2006), while slow decompression rates can result in effusive rhyolitic eruptions (e.g., Castro et al., 2013; Houghton et al., 2010). The efficiency of volatile degassing is therefore primarily controlled by decompression rate, which determines the time allowed for volatile exsolution and diffusion within the melt.

Because of the link between eruption style and decompression rate, several techniques have been developed to estimate decompression rates, including numerical modeling of ascent in the conduit (e.g., Kaminski and Jaupart, 1997; Papale and Dobran, 1993; Papale et al., 1998), or texture-based rate-meters such as bubble number density (e.g., Toramaru, 1995; 2006) microlite textures (e.g., Andrews, 2014; Castro and Gardner, 2008; Couch et al., 2003; Szramek, 2016; Toramaru et al., 2008), and reaction rims on hydrous minerals (e.g., Nicholis and Rutherford, 2004; Rutherford, 2008; Rutherford and Devine, 2003; Rutherford and Hill, 1993). However, many of these techniques resolve decompression rates either during the fastest (e.g., bubble

number density) or slowest (e.g., microlite textures and reaction rims) parts of the decompression, but rarely the entire range (Shea, 2017).

Diffusion modeling of volatiles in melts can be used to target a large range of timescales, depending on the diffusivities of the diffusing species and the composition of the fluid media (e.g., Costa et al., 2020). Recent studies have exploited diffusion modeling to estimate decompression timescales using a technique called melt embayment modeling (MEM), which was first conceptualized by Anderson (1991) and formalized by Liu et al. (2007). MEM consists of fitting diffusion profiles to volatile element concentration gradients that develop in crystal-hosted, open melt inclusions (termed melt embayments; Fig. 1a). Concentration gradients between the interiors of unsealed melt embayments and the far field melt develop during decompression as volatiles exsolve from the magma. Exsolution is hindered within the embayments, and volatiles diffuse towards the more volatile-depleted host melt. Embayments that are good candidates for MEM have a bubble near the mouth that provides an interface for volatile exsolution and buffers the concentration of volatiles in the melt at the mouth. For diffusion to yield useful concentration gradients, no bubble nucleation can occur within the embayment itself, as volatiles would be lost to the interior bubble(s) instead of the exterior bubble. Bubble nucleation does occur in some embayments, but others seem to lack them entirely (e.g., Liu et al., 2007; Lloyd et al., 2014; Myers et al., 2016). Some embayments are even devoid of melt (Befus and Manga, 2019). It is currently unclear as to why bubble nucleation does not occur in all embayments (Cashman and Rust, 2016).

Model input parameters for MEM include volatile diffusivity, initial and final volatile concentrations, and a solubility law to relate concentration to pressure (e.g., Liu et al., 2007). Initial volatile concentration is typically estimated by using data from closed melt inclusions

(e.g., Humphreys et al., 2008; Liu et al., 2007; Lloyd et al., 2014; Myers et al., 2016), the highest volatile concentration measured within the embayment (e.g., Myers et al., 2018), or leaving initial pressure as a free parameter that is part of the minimization procedure during modeling (e.g., Ferguson et al., 2016; Newcombe et al., 2020a). The inherent assumption in using the highest volatile concentration in the embayment is that decompression was sufficiently rapid to preserve the initial concentration without diffusive loss. Final water concentration is usually estimated by using the volatile concentration in the residual glass (e.g., Liu et al., 2007).

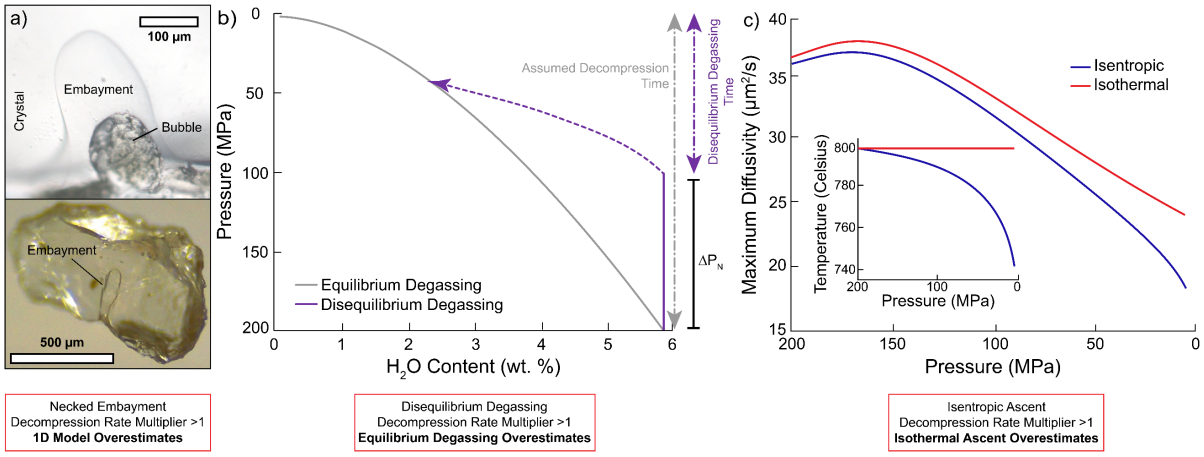

Figure 2.1. Examples of the complications present with melt embayment modeling. *a)* Examples of geometrical variety in melt embayments. The top embayment is an example of cylindrical geometry, with a preserved bubble at the mouth (modified from Myers et al., 2018). The bottom embayment is within a quartz crystal from the Bishop Tuff and displays a necked geometry with a constriction of ~40% of the total embayment width. *b)* Disequilibrium degassing and its implications for diffusion models. Diffusion models typically assume equilibrium degassing and volatile concentrations at solubility levels (gray curve), but disequilibrium degassing (purple curve) would result in less time for diffusion for the same amount of decompression as the main driving force for diffusion is absent until the supersaturation pressure (ΔP_N) is overcome. *c)* Difference in maximum diffusivity experienced over the same decompression pathway at the same decompression rate of 0.5 MPa/s for isothermal (red) and isentropic (blue) decompression. The inset shows the temperature-pressure relationship. With the difference in diffusivity over the decompression pathway, calculated decompression timescales are expected to be different between isothermal and isentropic conditions. Maximum diffusivity here reflects the maximum water content within the embayment; hence, there is a delay before the diffusivity begins to decrease as some time is required for diffusion to modify the highest water concentration.

MEM has been increasingly used in recent years to extract average decompression rates of basaltic (0.05-0.45 MPa/s; Ferguson et al., 2016; Lloyd et al., 2014; Newcombe et al., 2020a) and rhyolitic magmas (0.001-1.6 MPa/s; Humphreys et al., 2008; Liu et al., 2007; Myers et al.,

2016; 2018) using a variety of diffusing volatile species, such as H_2O, CO_2, and S. Potentially, other species with faster or slower diffusivities could be used to target an even broader range of decompression rates (e.g., Li). An important note is that decompression rate is non-linear (e.g., Su and Huber, 2017), and MEM retrieves an average decompression rate experienced by the melt embayment.

However, there are complications with the technique that have yet to be addressed. First and foremost, the current standard is to use one-dimensional diffusion models on measured profiles within complex three-dimensional objects (Fig. 2.1a). In particular, geometries that have a narrowing or "neck" at the opening are problematic as the constriction can potentially reduce the flux of volatiles leaving the embayment, and a 1D model cannot account for this. Merging diffusion fronts from 3D objects like crystals violate the infinite planar configuration assumed by 1D diffusion models (Krimer and Costa, 2017; Shea et al., 2015), and similar principles should be applicable to diffusion within melt embayments.

An additional complication that is typically not taken into account in MEM is non-equilibrium degassing. If no energetic barrier opposes nucleation of bubbles, exsolution begins as soon as the melt becomes supersaturated in a particular volatile species (equilibrium degassing) via decompression. If, however, nucleation requires large levels of supersaturation to be attained, formation of bubbles in the melt will be significantly delayed. Without bubble nucleation, volatile concentrations in the far field melt do not decrease, and there is no directed volatile diffusion out of the embayment, though random diffusion does occur regardless of concentration differences (e.g., Chakraborty, 2008; Fig. 2.1b). For high-silica melts, such as rhyolites, delayed nucleation is a possible problem, with ΔP_N =100-150 MPa of supersaturation necessary for homogeneous nucleation without the aid of crystals (i.e., Mangan and Sisson,

2000; Mourtada-Bonnefoi and Laporte, 1999). Recent studies have also demonstrated that disequilibrium degassing is possible in basalts, with ΔP_N ~45 MPa of supersaturation necessary for homogeneous nucleation (Le Gall and Pichavant, 2016a; 2016b). Timescales calculated from MEM will only record the time from bubble nucleation to quench, so failing to account for the pressure difference between storage and bubble nucleation can introduce error when the timescale is converted to a decompression rate (Fig. 2.1b). Although disequilibrium degassing can also be considered from the perspective of viscosity-hindered bubble growth (e.g., Gardner et al., 1999), we consider only the process of delayed nucleation herein.

Finally, as diffusion is a thermally activated process, it is sensitive to changes in temperature. Most models treat magma decompression as an isothermal process, but the rapid gas expansion associated with ascent in the shallow conduit can cool a rhyolitic magma as much as 200°C over 200 MPa of decompression if isentropic conditions are considered (Mastin and Ghiorso, 2001; Fig. 2.1c). The decrease in temperature associated with isentropic ascent would result in slower average diffusion rates as compared to isothermal ascent, which can influence calculated decompression rates by shortening the modeled timescale (e.g., Humphreys et al., 2008; Newcombe et al., 2020b).

Herein, we develop diffusion models that address the relative errors introduced to calculated decompression rates in simplified models. Specifically, we focus on water diffusivity in rhyolitic systems because water diffusivity and solubility are well constrained (e.g., Liu et al., 2005; Zhang et al., 2010), and rhyolitic systems are major targets of melt embayment studies (e.g., Humphreys et al., 2008; Liu et al., 2007; Lloyd et al., 2014; Myers et al., 2016). We focus on the three assumptions (1D vs 3D and simple vs complex geometry, disequilibrium vs equilibrium degassing, isothermal vs isentropic) previously described as they conceivably have

the largest impact on model results. Our results show that for the conditions studied, modeled decompression rates are most impacted by complex 3D geometry and disequilibrium degassing, with little influence from isentropic cooling. To guide future users of MEM, we provide a summary of our findings as modeling best practices to minimize error introduced by modeling assumptions.

2.3 Methods

Numerical diffusion models were developed to describe the motion of volatiles within melt embayments in silicic melts during decompression. First, we outline the general model scheme that was utilized for all the tested model simplifications (1D vs 3D, disequilibrium vs equilibrium degassing, isothermal vs isentropic). Then, we detail the differences in the models associated with each simplification tested.

2.3.1 Model Parameters

Because water diffusivity depends on its concentration (e.g., Zhang et al., 2010), all the models in this paper use the concentration-dependent version of Fick's 2nd Law, either in 1D:

$$\frac{\partial C}{\partial t} = \frac{\partial}{\partial x}\left(D\frac{\partial C}{\partial x}\right) \tag{2.1}$$

or 3D:

$$\frac{\partial C}{\partial t} = \frac{\partial}{\partial x}\left(D\frac{\partial C}{\partial x}\right) + \frac{\partial}{\partial y}\left(D\frac{\partial C}{\partial y}\right) + \frac{\partial}{\partial z}\left(D\frac{\partial C}{\partial z}\right) \tag{2.2}$$

where C is volatile concentration in wt. % (here, H_2O), t is time in seconds, D is diffusivity in $\mu m^2/s$, and x, y, z are the spatial directions in μm (Fig. 2.2). In melts, diffusivity is isotropic. Therefore, the same value of D_{H2O} was used for x, y, and z. We relate pressure and water concentration, in weight percent, via a solubility model. For the models exploring 3D geometry

and disequilibrium degassing, we used the solubility model of Liu et al. (2005). For the isentropic decompression models, we used rhyolite-MELTS (Ghiorso and Gualda, 2015; Gualda et al., 2012), which incorporates the solubility relations of MagmaSat. The saturation values of MagmaSat incorporate isentropic effects on water solubility, so they are preferred relative to the Liu et al. (2005) values.

We solved the 1D and 3D diffusion equations (Eq. 2.1 or 2.2) numerically using finite differences (forward in time and centered in space). The models were programmed to ensure that the stability criterion for explicit finite difference schemes was respected (Appendix A). Our spatial grid was equally spaced by 2-4 μm, depending on the overall duration and computational requirements of the model. For longer duration models, we used grids with fewer points but increased the spacing so that the total length of the embayment remained constant. Modeled timescales differ by ~ a maximum of 10% between the finer and coarser resolution models for the longest decompression times (Table 2.1). We assume that the initial water concentration in the outside melt and in the embayment are equal, a value that is determined by the water solubility at the initial pressure. For boundary conditions, at the embayment opening, the water concentration in the outside melt is determined by the pressure at each time step. For all models, we use fictitious points, which "reflect" back all diffusive flux, to impose no-flow boundaries at the crystal-melt interfaces.

In order to determine the independent effects of each assumption, we ran the models as a two-step process. First, a model was run with the realistic, complex conditions incorporated (i.e., 3D geometry, disequilibrium degassing, or isentropic ascent) to produce a concentration profile similar to what would be measured in a natural melt embayment. This "real" profile was then used as an output constraint for diffusion models that incorporated simplifying assumptions (i.e.,

no flux in other dimensions, isothermal ascent, and equilibrium degassing). Timescales, and thus decompression rates, from these 1D models were then compared with the known imposed decompression rate from the non-simplified models. This exercise was akin to measuring profiles in embayments and performing diffusion modeling with typical simplifying assumption, except that the true decompression rate was known here. The best-fit timescale was determined by a minimum weighted root mean squared difference (RMSD):

$$RMSD = \sqrt{\frac{1}{\sum_i^N \alpha_i}} \sum_i^N \left(\frac{\alpha_i \left(C_i - \hat{C}_i \right)}{N} \right)^2 \tag{2.3}$$

where C is the concentration value of the fitting model at index i, $\hat{C}$ is the concentration value of the "real" profile at index i, and α is a weighting factor. The weighting factor was assigned a value of 1 for the index closest to the mouth of the embayment and 0.1 for all other indices (e.g., Ferguson et al., 2016). This weighting forces the best solution to pass through or close to the water content calculated for the final pressure at the embayment mouth. Without it, modeled best-fit timescales tended to produce curves that were visually poor fits. For all fittings, we first used a coarse grid search of decompression rates, then successively narrowed in on a finer and finer grid search until the minimum RMSD was determined to the nearest second. To ensure the accuracy of our models, we checked the numerical results against the analytical solution for diffusion in a sphere (Crank, 1975) (Appendix A).

2.3.2 Effect of Geometry

Natural embayments exhibit a broad range of 3D geometries that are difficult to recreate comprehensively (e.g., Anderson, 1991; Fig. 2.1a). Instead, we tested only the influence of the key geometrical parameter of neck width. We created 5 synthetic embayments, starting with a cylindrical embayment with an opening diameter of 40 μm and successively narrowing the

opening by 20% increments (Fig. 2.2a). The geometries all included flared mouths (i.e., the location where the embayment joined with the outside melt) and curved backs, to best replicate natural embayments (Fig. 2.1a). Two additional models were tested with cylindrical geometries that had no flare at the base and with a flat back to isolate their effect on modeled decompression rates.

Decompression rates of 0.01, 0.1, 0.5, 1.8, and 6 MPa/s were imposed initially on all geometries. As tests were conducted and important shifts in decompression rate trends were identified, additional decompression rate tests were added as needed to complete the data set. All models were run with an initial pressure of 200 MPa and final pressure of 20 MPa. The relatively high final pressure was used to decrease computing time for longer duration models. All models were run with a constant temperature of 800°C.

2.3.3 Effect of Disequilibrium Degassing

All models associated with the disequilibrium tests were run as isothermal 1D models so as to isolate their effects from those of added dimensions and geometry. No general models for pressure-water concentration relationships during disequilibrium degassing currently exists, so we emulate the relationship in Figure 5 of Mangan and Sisson (2000). To simulate homogeneous bubble nucleation, water concentration was only allowed to decrease once a sufficient ΔP_N had developed (e.g., Mangan and Sisson, 2000; Mourtada-Bonnefoi and Laporte, 1999; 2004). Once nucleation started, the effective melt re-equilibration decompression rate dP_{re}/dt was faster than the overall system decompression rate dP_{sys}/dt by an exponential factor (e.g., Mangan and Sisson, 2000; Fig. 2.2b):

$$\frac{dP_{re}}{dt} = \frac{dP_{sys}}{dt} e^{0.003t} \tag{2.4}$$

where both decompression rates are in MPa/s, and *t* is time in seconds after bubble nucleation. For modeling purposes, it is convenient to calculate this as a function of pressure. However, it is

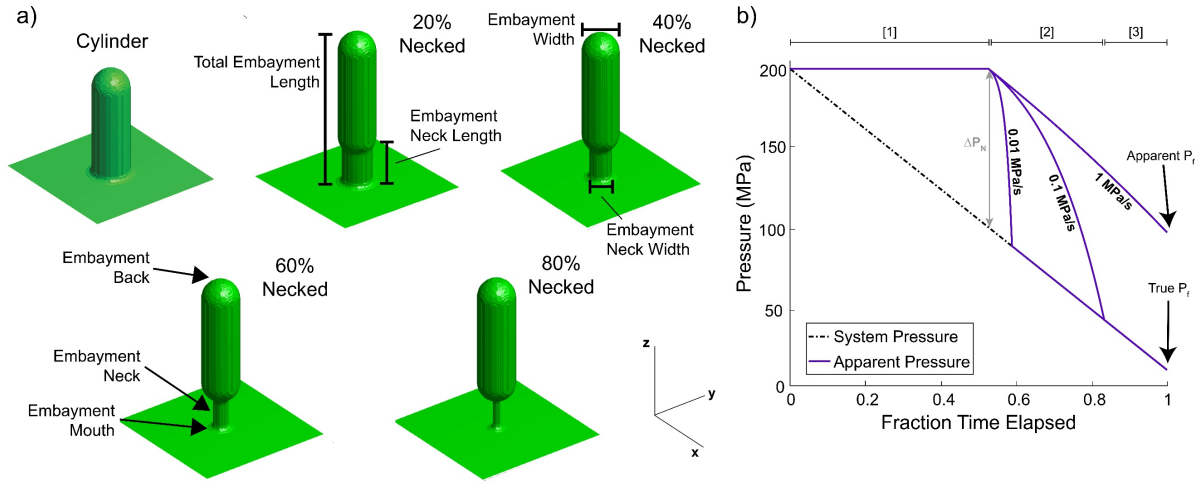

Figure 2.2. Model parameters explored for the variable geometry and disequilibrium degassing models. *a)* Base melt embayment geometries used in the 3D models and their different parts (see text). The cylinder embayment is shorter in length (240 μm) than the necked embayments (346 μm), but length is constant within a given geometry. *b)* Variations in system pressure and apparent melt pressure during disequilibrium degassing with fraction of total time elapsed, and for different decompression rates. Here, system pressure refers to the imposed lithostatic confining pressure, whereas apparent pressure refers to the pressure in the melt as calculated from water concentration, assuming equilibrium. Depending on the decompression rate, the melt water concentration may not re-equilibrate with the system pressure (e.g., 1 MPa/s curve), leading to a greater apparent final pressure (P_f) than that imposed in the model. If we consider the 0.1 MPa/s decompression pathway, region [1] is the fraction of decompression spent building up sufficient supersaturation (ΔP_N) to nucleate bubbles. Once bubbles are nucleated, water rapidly exsolves from the melt, resulting in a rapid decrease in apparent pressure until the dissolved water concentration is equal to the expected concentration at lithostatic pressure (region [2]). The pressure changes in region [2] are calculated with Eq. 2.4. Because the x-axis is "Fraction Time Elapsed" it appears as if the slowest decompression rate equilibrates rapidly. However, this is a result of more total time available to equilibrate. Once the apparent melt pressure and system pressure are equal, the two will remain concordant for the rest of the decompression (region [3]).

important to note that this apparent pressure is based on the dissolved water content within the melt; there is no actual difference in confining pressure between the embayment and the far field melt. The exponential constant of 0.003 was chosen based on the similarity of the produced pressure vs time curves to the experimental data outlined in Mangan and Sisson (2000). During the period of time in which the system is actively re-equilibrating and water supersaturation declines (e.g., region [2] of Fig. 2.2b), the concentration of water buffered by the bubble at the

mouth of the embayment equals water solubility at the pressure of the far field melt, as determined by Eq. 2.4. If the apparent pressure of the melt and the overall pressure of the system equilibrate, any continued decompression is calculated at the imposed linear decompression rate. For decompression rates sufficiently rapid that the system never re-establishes equilibrium, the apparent final pressure (i.e., the pressure corresponding to the disequilibrium water content at the mouth of the embayment) is greater than the true final pressure imposed on the system (Fig. 2.2b). In these cases, the final pressure used for fitting was based on the disequilibrium water concentration in the outside melt. This pressure based on water concentration will be referred to as the 'apparent pressure' in later discussions. In contrast, in models that imposed sufficiently slow decompression rates, the system could attain equilibrium solubility before reaching the final pressure.

We ran three series with variable initial pressures and ΔP_N values. In this paper, we use ΔP_N to refer to the supersaturation pressure needed to initiate bubble nucleation. Case 1 had an initial pressure of 200 MPa and a ΔP_N of 100 MPa, case 2 an initial pressure of 200 MPa and a ΔP_N of 150 MPa, and case 3 an initial pressure of 300 MPa and a ΔP_N of 150 MPa. All models were run to a final pressure of 10 MPa and at a temperature of 850°C. Tested decompression rates ranged from 0.01 to 10 MPa/s.

In addition to the models presented in the text, a separate set of models were run with exponential factors of 0.03 and 0.0003 to examine the influence of the re-equilibration rate on model results. As there are few previous constraints on disequilibrium degassing pathways, it is necessary to evaluate how changing the exponent by +/- an order of magnitude impacts our results. These models were all run at an initial pressure of 200 MPa and ΔP_N of 100 MPa (Fig. A-S3).

2.3.4 Effect of Isentropic Ascent

Although most embayment diffusion models assume isothermal ascent, isentropic expansion of exsolved volatiles is postulated to cause significant cooling of the magma in the shallow conduit (Mastin and Ghiorso, 2001; Newcombe et al., 2020b; Fig. 2.1c). To test the influence of this cooling on modeled timescales, we ran 1D isentropic diffusion models to produce a profile that was subsequently fit by an isothermal model. We calculated the temperature change by running rhyolite-MELTS in isentropic mode with a water-saturated rhyolitic input composition (Glass Mountain, CA; sample 1406M; Grove et al., 1997) starting at a temperature of 800°C. All crystallization was suppressed during these runs in order to isolate the effect of gas expansion. We tested three different final pressures, 20, 10, and 5 MPa, since the cooling is more rapid at lower pressures (Fig. 2.1c). The models imposed variable decompression rates ranging from 0.02 to 10 MPa/s. MELTS outputs for dissolved water content versus pressure were used to construct an empirical solubility relationship for the Glass Mountain composition:

$$C_w = 0.2746P^{0.563} \quad (2.5)$$

Here, pressure is in MPa. During fitting, the initial temperature of 800°C was used as the isothermal temperature.

2.4 Results and Interpretations

To investigate deviations in decompression rate between the groundtruth and simplified models, we introduce a "Decompression Rate Multiplier" (DRM), defined as the ratio of modeled to imposed decompression rate. A DRM of 1 indicates perfect retrieval of the imposed decompression rate, a DRM of >1 indicates a faster modeled decompression rate, and a DRM of <1 indicates a slower modeled decompression rate. For almost all of our modeling scenarios, the

fastest decompression rates produce DRMs slightly less than one (0.88-0.96). However, that difference is usually produced by a difference of no more than 3 seconds between the imposed and modeled timescales. The total length of the embayment impacts the decompression rate at which the maximum DRM occurs, so we avoid direct comparisons of DRM between models with differing lengths in our subsequent discussion.

2.4.1 Geometry

Models using a cylindrical geometry show good agreement between 1D and 3D models (i.e., DRMs are all close to or equal to 1; Fig. 2.3). In detail, the DRM decreases slightly from 1 at a decompression rate of 1.8 MPa/s to 0.92 at a decompression rate of 0.01 MPa/s (Table 2.1), indicating that the 1D model is calculating a decompression rate that is very slightly slower than the 3D imposed decompression rate.

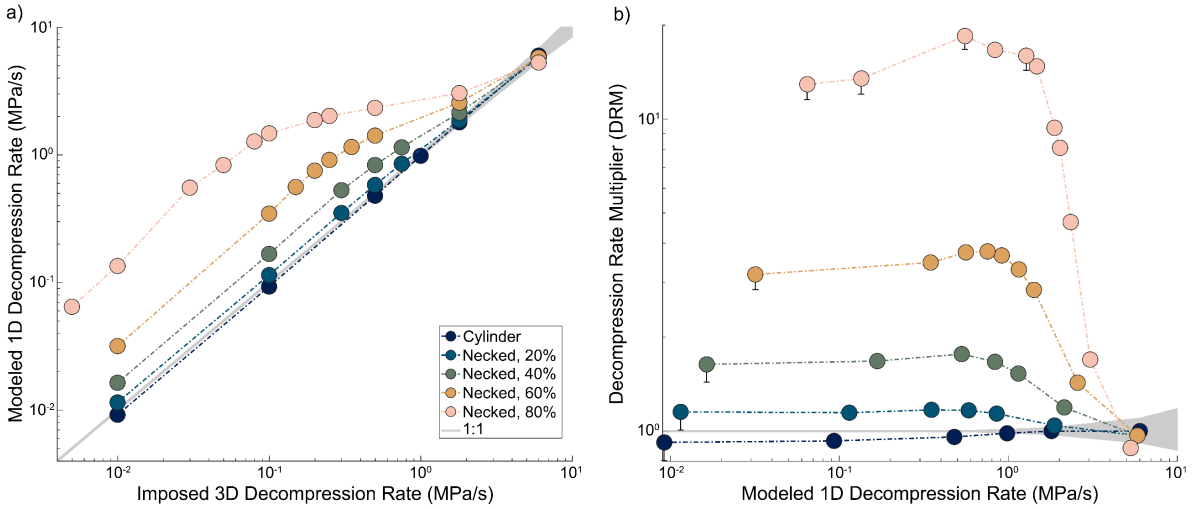

Figure 2.3. Decompression rate discrepancies in models exploring the effects of 1D vs. 3D models and variable geometry (cylindrical vs. necked). Shaded region shows the margin of numerical fitting error corresponding to ±3 seconds at different decompression rates (where it is larger than the thickness of the 1:1 line). *a)* Imposed decompression rate in 3D models and decompression rates obtained from best-fit 1D models. *b)* Modeled 1D decompression rate against the DRM (ratio of modeled decompression rate to the imposed decompression rate; i.e., the separation between the 1:1 line and a given data point in *a*). Error bars on specific data points indicate coarser spatial resolution models, and the maximum possible error imparted on the data point by the decreased resolution. For geometries with >40% neck constriction, the DRM is large (>2) for most decompression rates.

Table 2.1. Summary of variable geometry model results

Geometry[a]	Imposed dP/dt (MPa/s)	Modeled dP/dt (MPa/s)	DRM[b]
Cylinder	6	6.00	1.00
Cylinder	1.8	1.80	1.00
Cylinder	1	0.984	0.98
Cylinder	0.5	0.479	0.96
Cylinder	0.1	0.093	0.93
Cylinder	0.01	0.009	0.92
Cylinder (Flat Back)	0.1	0.100	1.00
Cylinder (Flat Sides)	0.1	0.093	0.93
20% Necked	6	5.81	0.97
20% Necked	1.8	1.88	1.04
20% Necked	0.75	0.853	1.14
20% Necked	0.5	0.583	1.17
20% Necked	0.3	0.351	1.17
20% Necked	0.1	0.115	1.15
20% Necked	0.01	0.012	1.15
40% Necked	6	5.81	0.97
40% Necked	1.8	2.14	1.19
40% Necked	0.75	1.15	1.53
40% Necked	0.5	0.833	1.67
40% Necked	0.3	0.529	1.76
40% Necked	0.1	0.168	1.68
40% Necked	0.01	0.016	1.64
60% Necked	6	5.81	0.97
60% Necked	1.8	2.57	1.43
60% Necked	0.5	1.42	2.83
60% Necked	0.35	1.15	3.30
60% Necked	0.25	0.914	3.65
60% Necked	0.2	0.753	3.77
60% Necked	0.15	0.561	3.74
60% Necked	0.1	0.347	3.47
60% Necked	0.01	0.032	3.18
80% Necked	6	5.29	0.88
80% Necked	1.8	3.05	1.69
80% Necked	0.5	2.34	4.68
80% Necked	0.25	2.02	8.09
80% Necked	0.2	1.88	9.38
80% Necked	0.1	1.48	14.75
80% Necked	0.08	1.28	15.96
80% Necked	0.05	0.833	16.67

80% Necked	0.03	0.554	18.46
80% Necked	0.01	0.135	13.49
80% Necked	0.005	0.065	12.93

[a]All listed models were run at a temperature of 800°C, initial pressure of 200 MPa, and final pressure of 20 MPa

[b]Decompression rate multiplier - see text for definition

Models using a necked geometry, regardless of the degree of constriction, all gave the same general pattern; as imposed decompression rate decreases, the DRM increases to a maximum value and then decreases. The value and position of maximum DRM is a function of the degree of constriction. For a fast decompression rate of 6 MPa/s, all tested geometries result in little to no difference from the base model. The modeled timescale is a little slower than the imposed decompression rate, but this is likely due to the slightly different shapes of the 1D and 3D profiles (Fig. 2.4a). The 3D profiles have sharper inflection points in concentration at the join between the necked region and the main body of the embayment that the 1D models cannot reproduce accurately. Models run at a decompression rate of 6 MPa/s are fast enough that the error introduced by this discrepancy is greater than any effect of geometry. Below this decompression rate, the DRM increases for all geometries, with greater decompression rate mismatch for the more necked geometries. For example, at a decompression rate of 1.8 MPa/s, the DRMs for constrictions of 20, 40, 60, and 80% at the embayment mouth are 1.04, 1.19, 1.43, and 1.69. Each of the necked geometries also displays maximum DRMs at different imposed decompression rates. The maximum DRM increases with degree of constriction, reaching 1.17, 1.76, 3.77, and 18.46 for 20, 40, 60, and 80% necked, respectively. Although DRM decreases at slower decompression rates, the DRM never re-attains the value of ~1 even for the slowest decompression rate tested (0.01 MPa/s for all geometries except 80% necked, which is 0.005

MPa/s). At these decompression rates, the final DRMs are 1.15, 1.64, 3.17, and 12.93 for constrictions of 20, 40, 60, and 80%, respectively.

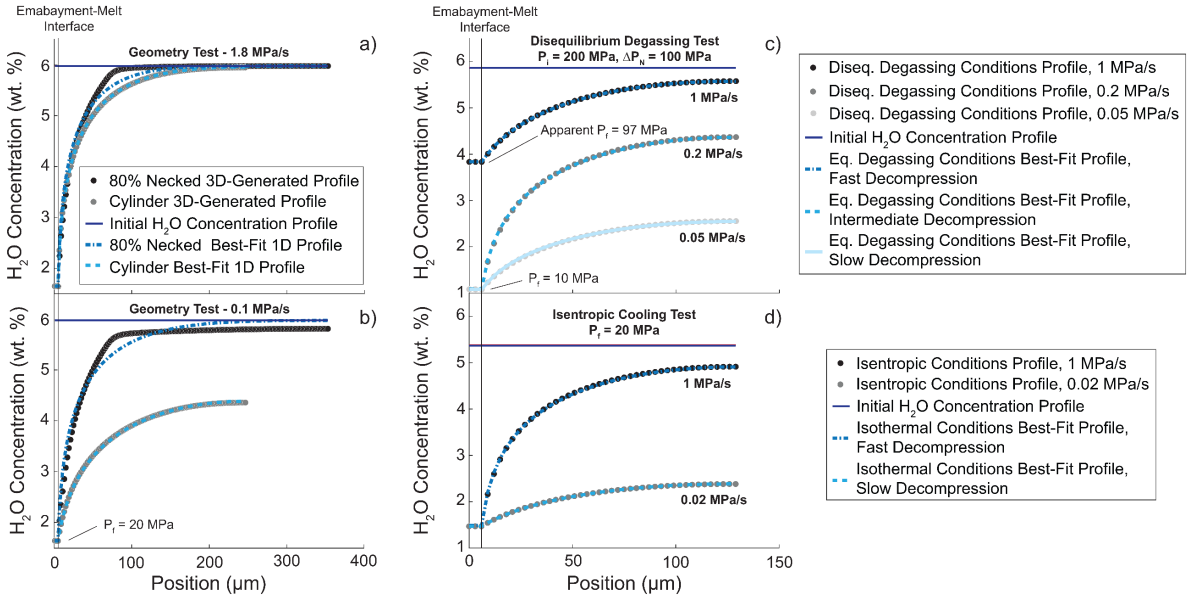

Figure 2.4. Examples of profiles generated in the "groundtruth" models and associated best-fit models for each of the tested simplifications. Water concentration in the melt outside the embayment is set to the equilibrium value with the coexisting vapor at each pressure step, hence the flat concentration at the embayment-melt interface. *a)* and *b)* show comparisons of profiles from the cylindrical and 80% necked geometries at two different decompression rates. Note the sharp inflection point present in the 80% necked geometry 3D-generated profile that the 1D model cannot replicate. In *a)*, both the cylindrical and 80% necked geometries have maintained a plateau of high water concentration, but in *b)*, the cylindrical geometry has lost the initial high water concentration, whereas the 80% necked geometry has only just begun to lose the high initial water concentration. Although this is partially due to the shorter total length of the cylindrical embayment, it is mainly associated with the buffering effect of the neck on the 80% necked geometry. Importantly, in *b)*, the shape of the 80% necked 3D-generated profile still appears to have a plateau-like shape, despite having lost the initial high water concentration. *c)* Example profiles from the disequilibrium degassing test, using case 1. For the fastest decompression rate, the apparent final pressure is greater than the imposed final pressure. The greatest difference in water concentration between the interior of the embayment and the far field melt occurs at 0.2 MPa/s. *d)* Example profiles from the isentropic decompression test, using profiles with an imposed final pressure of 20 MPa. Isothermal decompression fitting models fit the profiles well across the range of decompression rates shown.

For any given geometry, the increases and decreases in DRM are tied to the location of the diffusion front at a given point in time (Fig. 2.5). For the cylindrical geometry, the 1D model can accurately recover the 3D decompression rate (DRM of 1) until the diffusion front reaches the back of the embayment. Once the diffusion front reaches the back of the embayment, the DRM steadily decreases below 1. This decrease is attributed to the curvature at the back of the

3D embayment, where diffusive fluxes from the sides start to converge and merging diffusion fronts become apparent. With a curve at the back of the embayment, the volume of melt, and thus water, is less than if the back was flat. Therefore, the water concentration decreases faster in 3D than in 1D. The 1D model yields a decompression rate that is based on a lower total flux, resulting in a slower decompression rate.

This interpretation is supported by two additional models that test the effect of the default flared opening and the curved embayment back used for most 3D models (Table 2.1). Each of the two models removed one of these morphological features to obtain either a flat, orthogonal opening or back. At an imposed decompression rate of 0.1 MPa/s, the cylindrical model without a flared base but with a curved back yields a DRM of 0.93, identical to the DRM that was calculated for the initial flared version. However, the geometry with the flared base but a flat back resulted in a DRM of 1. Therefore, the decrease in DRM is related to interaction of the diffusion front with the curved back.

Similarly, water flux in the necked geometries is impacted by merging diffusion fronts originating from geometric constrictions and embayment-crystal interface curvature. At the fastest imposed decompression rate, there is essentially no difference regardless of the degree of necking because the diffusion front is still largely within, or close to, the constriction (Fig. 2.5). Thus, at these rates, diffusion creates gradients indistinguishable from gradients within models that utilize the idealized cylindrical geometry. However, once the diffusion front moves into the main body of the embayment, the impact of the constriction on the concentration profile becomes apparent. The 3D diffusion front is no longer flat, but instead bends as flux moves from near the outer edge of the embayment towards the opening of the neck (Fig. 2.5). For a profile taken down the middle of the 3D embayment, the water concentration plateau is maintained for

longer durations than for constriction-free embayments because fluxes from the sides partly buffer water loss (Fig. 2.4). Thus, for a 1D model performed along the same region, shorter timescales are needed in order to fit the output 3D concentration profile. The 1D model therefore yields an artificially faster decompression rate. This effect is scaled by the degree of necking because water retention increases with increasing constriction. As the diffusion front moves through the body of the embayment, the effect becomes more and more pronounced, and the DRM rapidly increases.

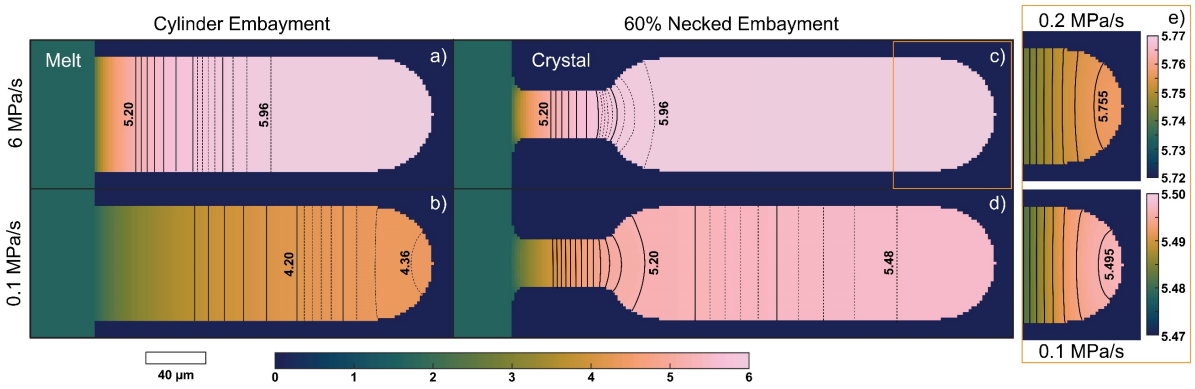

Figure 2.5. 2D slices through select 3D embayment models with key diffusion features, at the final pressure of 20 MPa. The white scale bar is equivalent for all of the panels. Contours indicate the higher range of water contents (H_2O > 5.2 wt. %, except for the slow decompression of the cylinder embayment, which is H_2O > 4.2 wt. %). Solid contours are in intervals of 0.1 wt. %, and the dashed contours are in intervals of 0.02 wt. %. For the zoomed in views of the necked embayment (orange box) the contour interval is 0.002 wt. %. In the cylindrical models (*a* and *b*), the diffusion fronts are mostly flat, except where there is an interaction with the curved back of the embayment. In the necked models (*c* and *d*), the diffusion front bends near the junction between the neck and the main body. The orange box (*e*) shows the curvature of the diffusion front associated with the shape of the embayment back. The more subtle curved diffusion front stemming from the back of the embayment (as compared to the curvature from the neck) is made apparent only by examining H_2O variations at a very fine concentration scale (colors corresponding to < 0.1 wt. % difference in these images).

To preserve realistic embayment shapes, the necked embayments also possess a curved back. Thus, similar to the cylindrical geometry, there is a decrease in DRM after attaining a maximum at a given dP/dt as the diffusion front reaches the back of the embayment. The decompression rate associated with the maximum DRM corresponds to a complex interplay between oppositely curved diffusion fronts originating from the neck and the curved back (Fig.

2.5). The maximum DRM does not occur at the time at which the diffusion front reaches the back of the embayment, but rather once the curved diffusion front from the back of the embayment extends a particular distance into the body of the embayment (Fig. 2.5). Unlike with the cylindrical geometry, the DRM does not fall below 1 once the diffusion front reaches the back of the embayment in the necked geometries. Although there is a decreased mass flux from the back of the embayment, the loss of water is reduced at the neck. Thus, the DRM decreases more gently as flux is being buffered by the constriction.

In summary, the DRM is close to 1 across the range of decompression rates tested for the cylindrical geometry, but systematically increases at almost all decompression rates as the degree of necking (i.e., amount of constriction) increases. Trends in increasing and decreasing DRM arise due to interaction of the diffusion front with the 3D embayment geometry, such as the embayment neck or the curved back.

2.4.2 Disequilibrium Degassing

Relative trends in DRM are similar for all conditions tested (Fig. 2.6). At fast decompression rates, the DRM is relatively low (~1), then steadily increases as decompression rate decreases, reaches a peak value, and decreases again.

The magnitude of the maximum DRM is a function of the proportion of the total decompression time spent overcoming ΔP_N. For cases 1 (P_i=200 MPa, ΔP_N =100 MPa) and 3 (P_i=300 MPa, ΔP_N =150 MPa) for which ΔP_N represents about half of the total decompression, the peak in DRM is of equal magnitude, with case 1 having a maximum DRM of 2.79 and case 3 having a maximum DRM of 2.61 (Table 2.2). For case 2 (P_i=200 MPa, ΔP_N =150 MPa) in which

ΔP_N represents about three-quarters of the decompression time, the peak in DRM is much greater than the other two cases, attaining a value of 7.73.

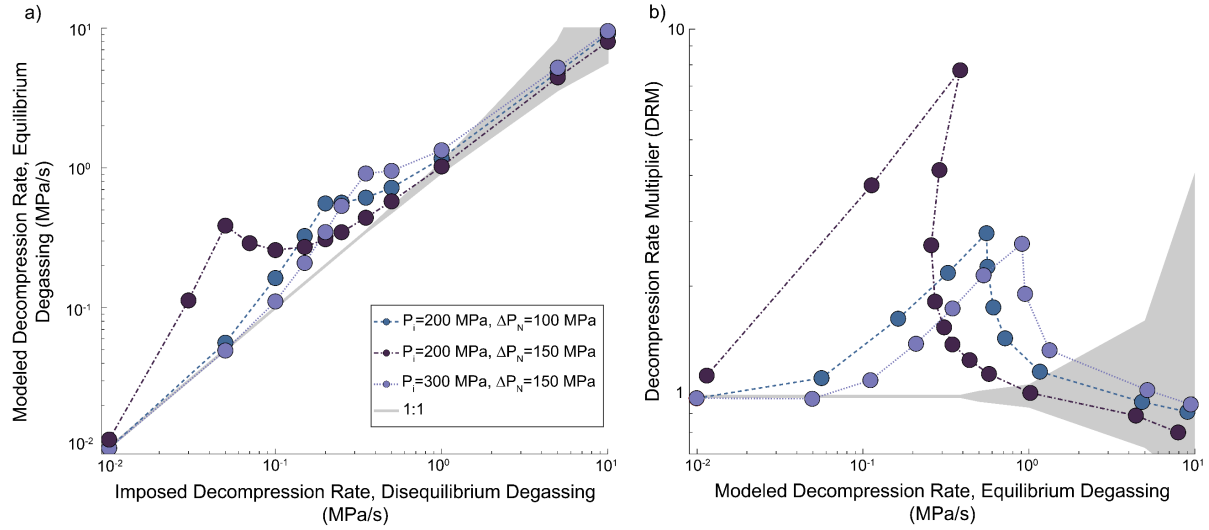

Figure 2.6. Discrepancy in decompression rates calculated assuming equilibrium degassing when degassing occurs under disequilibrium conditions. Shaded region shows numerical fitting uncertainties estimated to be within ±3 seconds of the imposed decompression rate (where it is larger than the 1:1 line). This ±3 seconds is calculated relative to the apparent final pressure when it is different from the imposed final pressure so that it matches the calculation method of the decompression rate. *a)* Comparison between decompression rates imposed in disequilibrium degassing models and best-fit decompression rates obtained assuming equilibrium degassing. *b)* Best-fit decompression rate obtained by assuming equilibrium degassing against the DRM for each model.

The decompression rate at which maximum DRM is produced is a function of both starting pressure and the relative magnitude of ΔP_N to the total decompression. For case 1, the maximum DRM occurs at an imposed decompression rate of 0.2 MPa/s. For case 2, which has the same initial pressure as case 1 but greater ΔP_N, the maximum is shifted to a slower imposed decompression rate of 0.05 MPa/s. For case 3, which has a greater initial pressure but same ΔP_N as case 2, the maximum is shifted to a faster decompression rate at 0.35 MPa/s. The location of the maximum DRM is mainly tied to the apparent pressure state of the system upon quench. The maximum DRM is produced for decompression rates that result in the apparent pressure, as determined by water content, just barely catching up to the system pressure. This scenario represents the maximum apparent pressure difference between the embayment and the system

Table 2.2. Summary of disequilibrium model results

P_i (MPa)[a]	ΔP (MPa)	Apparent Melt P_f (MPa)[b]	Imposed dP/dt (MPa/s)	Modeled dP/dt (MPa/s)	DRM[c]
200	100	109	10	9.10	0.91
200	100	108	5	4.84	0.97
200	100	97	1	1.17	1.17
200	100	81	0.5	0.721	1.44
200	100	64	0.35	0.613	1.75
200	100	38	0.25	0.565	2.26
200	100	10	0.2	0.557	2.79
200	100	10	0.15	0.326	2.17
200	100	10	0.1	0.163	1.63
200	100	10	0.05	0.056	1.12
200	100	10	0.01	0.010	0.99
200	150	160	10	8.00	0.80
200	150	160	5	4.44	0.89
200	150	158	1	1.02	1.02
200	150	155	0.5	0.577	1.15
200	150	152	0.35	0.440	1.26
200	150	149	0.25	0.347	1.39
200	150	145	0.2	0.309	1.55
200	150	139	0.15	0.272	1.82
200	150	123	0.1	0.258	2.58
200	150	94	0.07	0.290	4.14
200	150	33	0.05	0.387	7.73
200	150	10	0.03	0.113	3.76
200	150	10	0.01	0.011	1.14
300	150	157	10	9.53	0.95
300	150	154	5	5.21	1.04
300	150	126	1	1.34	1.34
300	150	81	0.5	0.952	1.90
300	150	29	0.35	0.913	2.61
300	150	10	0.25	0.535	2.14
300	150	10	0.2	0.348	1.74
300	150	10	0.15	0.209	1.39
300	150	10	0.1	0.111	1.11
300	150	10	0.05	0.049	0.99
300	150	10	0.01	0.010	0.99

[a]All models were run with an imposed final pressure of 10 MPa and temperature of 850 °C

[b]Apparent melt pressure based on water concentration

[c]Decompression Rate Multiplier - see text for definition

with the minimum amount of time to diffusively re-equilibrate (Fig. 2.4c). As decompression rate decreases further, there is more time for the embayment to diffusively re-equilibrate with this large volatile concentration difference, thus resulting in a decrease in DRM. Because the relative time needed for the apparent pressure to catch up to the imposed system pressure is dependent on both the initial pressure and the magnitude of ΔP_N, the location of the maximum DRM is a function of both parameters.

DRM is close to 1 when the system has a large difference between the external pressure and the apparent pressure, resulting in a high degree of water supersaturation in the far field melt. Presumably, this low DRM occurs because both the total time allowed for diffusion and the H_2O concentration difference between the interior of the embayment and the outside melt is relatively small (Fig. 2.4c). Both of these factors contribute to the similarity between modeled and imposed decompression rates, when the apparent final pressure of the melt is taken into account. The maximum DRM is produced when the H_2O concentration difference between the interior of the embayment and outside melt is largest, and this generally corresponds to the decompression rate that results in the apparent pressure just barely re-equilibrating with the system pressure (Fig. 2.4c). Any additional time for diffusion allows for a "smoothing out" of the remaining impacts of the disequilibrium (Fig. 2.4c). This process is reflected in the decreasing DRM, and the fact that all of the cases re-attain a DRM of ~1 at the slowest tested decompression rate.

The relative rate at which the supersaturation of water, and thus the greater apparent pressure, reaches equilibrium with the imposed system pressure is poorly constrained, so the absolute values of these results are only correct to nature if the exponential factor is actually 0.003. Since the location of peak DRM is a function of how quickly the melt water re-establishes pressure equilibrium with the system, modifying the exponential factor makes a major

difference. With bigger exponential factors, the melt water re-establishes pressure equilibrium more quickly, shifting peak DRM to faster decompression rates. With smaller exponential factors, the melt water re-establishes pressure equilibrium more slowly, shifting peak DRM to slower decompression rates (Fig. A-S3).

In summary, the magnitude of the maximum DRM increases as the ratio of ΔP_N to total decompression pressure increases. The decompression rate at which the maximum DRM occurs is a function of both initial pressure and ΔP_N; greater initial pressure shifts the maximum towards faster decompression rates, and greater ΔP_N shifts the maximum towards slower decompression rates.

2.4.3 Isentropic Ascent

Regardless of decompression rate or quench pressure range examined, isentropic decompression results in DRMs close to 1 (Fig. 2.7). For decompression rates ≤1 MPa/s, the DRM is slightly greater than 1 and increases with decreasing decompression rates. Additionally, lower quench pressures produce greater DRMs as compared to higher quench pressures. The difference between the three quench pressures for a given decompression is small, however. For example, for an imposed decompression rate of 0.02 MPa/s, the DRMs for quench pressures of 20, 10, and 5 MPa are, respectively, 1.23, 1.28, and 1.32 (Table 2.3). These values also correspond to the maximum DRMs calculated for each quench pressure, and our examined range covers most of the range of studies of decompression rate; thus we can assume that isentropic cooling has a minimal effect in almost all cases. Additionally, at even slower decompression rates, isentropic cooling is likely buffered by heat input from other sources, such as latent heat of crystallization of microlites (e.g., Newcombe et al., 2020b).

Table 2.3. Summary of isentropic model results

Imposed P_f (MPa)[a]	Apparent P_f (MPa)[b]	Imposed dP/dt (MPa/s)	Modeled dP/dt (MPa/s)	DRM[c]
20	21	10	9.42	0.94
10	11	10	9.00	0.90
5	6	10	8.82	0.88
20	21	5	4.84	0.97
10	11	5	4.73	0.95
5	6	5	4.85	0.97
20	21	1	1.05	1.05
10	11	1	1.06	1.06
5	6	1	1.07	1.07
20	23	0.5	0.527	1.05
10	13	0.5	0.537	1.07
5	8	0.5	0.539	1.08
20	21	0.1	0.114	1.14
10	11	0.1	0.117	1.17
5	6	0.1	0.119	1.19
20	21	0.02	0.025	1.23
10	11	0.02	0.026	1.28
5	6	0.02	0.026	1.32

[a]All models were run with initial pressure of 200 MPa and initial temperature of 800 °C

[b]Apparent final pressure is based on far field melt water concentration and an isothermal solubility relationship

[c]Decompression Rate Multiplier - see text for definition

The slight increases in DRM with decreasing decompression rate and decreasing quench pressure are related to the effect of temperature on diffusivity. Along the decompression path, the more time spent at lower temperature and slower diffusivity conditions, compared to the higher temperature isothermal model, the greater the discrepancy between actual diffusion and expected diffusion timescales.

In summary, the effects of isentropic cooling are relatively minimal, even at slow decompression rates. There is a slight dependence on quench pressure, with lower quench pressure resulting in greater DRM at the same decompression rate, but the difference is small.

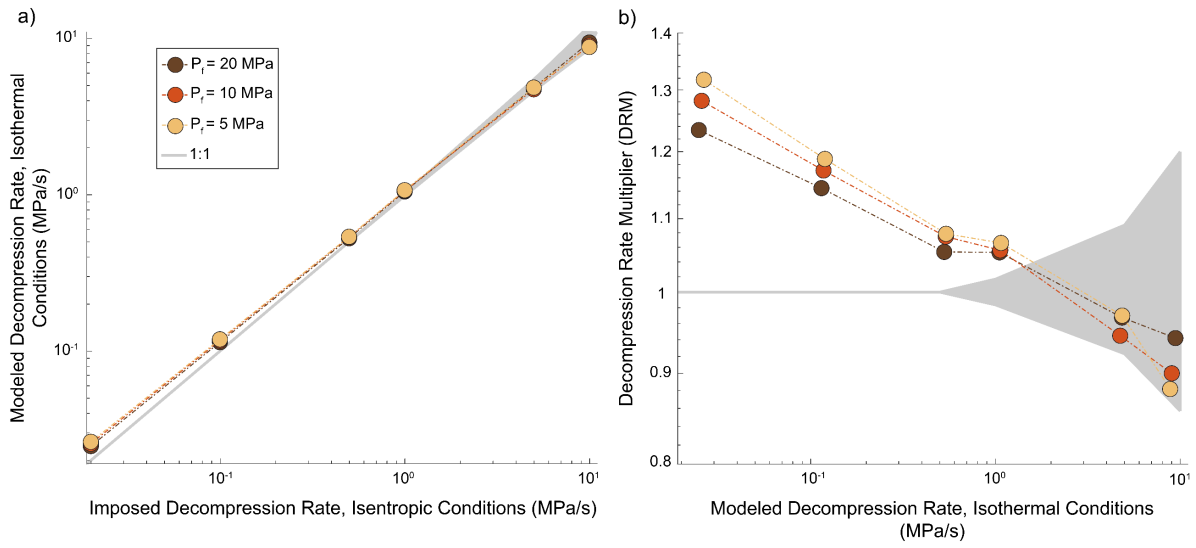

Figure 2.7. Discrepancy in decompression rates calculated assuming isothermal decompression when decompression occurs under isentropic conditions. Shaded region shows numerical fitting uncertainties estimated to be within ±3 seconds of the imposed decompression rate (where it is larger than the 1:1 line). *a)* Comparison between decompression rates imposed in isentropic conditions and best-fit decompression rates obtained assuming isothermal conditions. *b)* Best-fit decompression rate obtained by assuming isothermal conditions against the DRM for each model. Note that the y-axis scale is much smaller than the previous DRM plots as DRM is minimal in these models.

2.5 Discussion

Our modeling results demonstrate that some simplifications to melt embayment diffusion models introduce errors in the estimation of timescales and thereby decompression rates. In particular, disequilibrium degassing and 3D embayment geometry can introduce error of approximately one order of magnitude in calculated decompression rate. Isentropic decompression, on the other hand, does not seem to significantly impact modeled timescales. However, these three factors are not the only assumptions in MEM, and we further develop the impact of assumptions associated with initial conditions on calculated decompression rates. Finally, we give a list of recommendations for best practices to minimize errors introduced into timescales by model assumptions.

2.5.1 Prevalence of Disequilibrium Degassing

Disequilibrium degassing causes significant deviations in modeled timescales. The buildup of disequilibrium conditions depends chiefly on nucleation mechanism (Mangan and Sisson, 2000). Onset of homogeneous nucleation requires attainment of large supersaturation pressures in rhyolitic melts (e.g., Mangan and Sisson, 2000; Mourtada-Bonnefoi and Laporte, 1999; 2004). The prevalence of homogeneous over heterogeneous nucleation in crystal-poor rhyolites has recently come under scrutiny (e.g., Shea, 2017). For instance, rhyolitic melts involved in eruptions such as Novarupta in 1912 could not have experienced homogeneous nucleation because the supersaturation pressure necessary for homogeneous nucleation to take place exceeds the total pressure change from storage to fragmentation (Gonnermann and Houghton, 2012; Shea, 2017). It was previously suggested that crystal-poor rhyolites must nucleate bubbles homogeneously due to the lack of favorable nucleation sites (e.g., Mangan et al., 2004); however, recent work has suggested that nanometer-sized Fe-Ti oxide crystals might be more abundant than previously thought and provide sufficient nucleation sites for bubble nucleation to be dominantly heterogeneous (Burgisser et al., 2020; Caceres et al., 2020; Shea, 2017). It is impossible to say without a careful, very high-resolution petrographic examination of eruption products w hether a magma has undergone a particular style of nucleation. Shallowly stored, crystal-rich magmas that can readily nucleate and exsolve volatiles should more closely follow near-equilibrium degassing pathways. Therefore, these magmas are less likely to be impacted by modeling errors associated with disequilibrium degassing. It is possible to still use MEM even in systems that have experienced disequilibrium degassing if the degassing pathway can be defined (e.g., Gonnermann and Manga, 2005). However, resolving the nucleation mechanism debate will provide key guidance to the prevalence and severity of impact of

disequilibrium effects on decompression rates derived from embayments hosted within crystal-poor rhyolites.

2.5.2 Impacts of Initial Conditions Assumptions

The initial volatile concentration in the interior of an embayment depends on when the embayment forms. Silicic magmas can be stored at multiple levels within the crust (e.g., Cashman et al., 2017; Edmonds et al., 2019), and melt-filled embayments may form via rapid crystal growth during storage and/or ascent. The timescales and mechanisms of embayment formation have not been thoroughly studied to date, so it is unclear when in a crystal's lifespan they form. MEM assumes that the embayments formed at the storage level, and that their initial water content therefore corresponds to that depth. Recent work by Barbee et al. (2020) and Loewen et al. (2017) indicates that for rhyolites, melt-filled embayments form in quartz as a response to rapid growth, typically associated with changes in pressure and/or temperature. Thus, the initial volatile concentration within the embayments should reflect the conditions that the host quartz experienced during rapid growth. However, rapid growth could occur at any depth. Thus, the appropriate initial water content may not always be obvious.

Determination of the timing of embayment formation is essential to ascertain initial model conditions. Two approaches are typically used to recover initial depth and water content: (1) use the maximum water content measured in melt inclusions and assume it records the initial pressure and depth of embayment formation (e.g., Humphreys et al., 2008; Liu et al., 2007; Lloyd et al., 2014; Myers et al., 2016) or (2) use the maximum water content measured in the embayment as representative of the initial pressure (e.g., Myers et al., 2018). However, there are occasionally differences between these two values, even in the same crystals (Myers et al., 2016; 2018). Under the assumption that melt inclusions did not leak and faithfully recorded volatile

concentrations at depth, our modeling results can shed light on the possible reasons for discrepant melt inclusion and embayment water contents. Potentially, the initial melt inclusion water concentration is correct, and diffusion was sufficiently long that the plateau lost its initial value. Interestingly, the initial H_2O value in our models can be lost while still maintaining a plateau-like inner concentration profile, particularly for the necked geometries (Fig. 2.4b). Thus, the presence of a plateau alone does not guarantee preservation of initial water concentration.

So far, our treatment of the profiles obtained from the groundtruth models assumes that the initial, higher, H_2O concentration is known, even when it is not preserved within the embayment. This is the equivalent scenario where melt inclusions can be used to estimate initial volatile concentrations even if the highest value within the embayment is lower (e.g., embayment was formed at a shallower depth than the melt inclusions). To test the alternative scenario (i.e., using the highest volatile concentration in the embayment as the initial volatile concentration), we re-ran 1D models with a different approach for all of the 3D models in which the initial high water content was lost. This time, we calculated the saturation pressure associated with the highest water concentration in the embayment rather than a known initial value. The 1D model was then run with that lower calculated initial pressure, and the best fitting decompression rate to the groundtruth 3D model was recalculated (Table 2.4). Essentially, this assumes no knowledge of the imposed decompression rate and starting pressure, instead using values that are calculated from model fits and water content, much like typical applications of MEM. We find that for all cases, the DRM is greater than 1, and compounds the error associated with geometry (Fig. 2.8). Thus, using a starting pressure that is less than what the system actually experienced can lead to significant additional overestimation of decompression rate; even geometries that are mostly unaffected by complex 3D fluxes, such as the cylinder, can yield erroneous decompression rates.

These results are consistent with the findings of Myers et al. (2018). Their 1D models tested melt inclusion water content and maximum embayment water content as starting

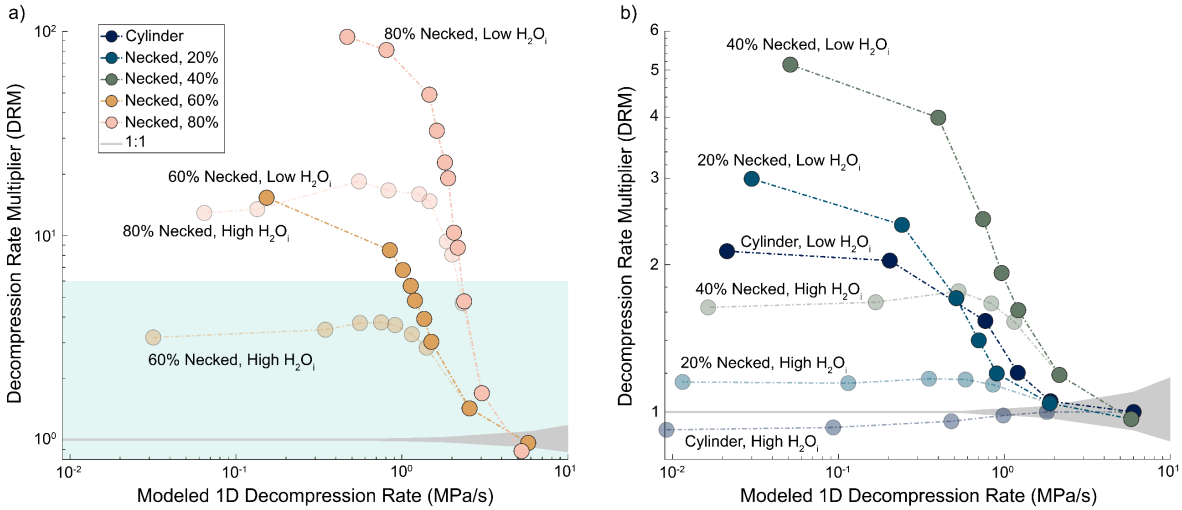

Figure 2.8. Changes to modeled 1D decompression rate vs. DRM trends when different assumptions are made about the starting pressure of the diffusion models. The light blue shaded region in *a* shows the extent of *b*. The gray shaded region shows numerical fitting uncertainties estimated to be within ±3 seconds of the imposed decompression rate (where it is larger than the 1:1 line). Each darker colored line has the corresponding model results using the correct starting pressure (as in Fig. 2.3b) shown in lighter color for reference. For all geometries, once the high H_2O concentration in the back of the embayment begins to decrease, there is a corresponding increase in DRM when using the H_2O concentration in the embayment to infer the initial modeling conditions. The calculated decompression rate between the two scenarios in their study varied by as much as an order of magnitude in some cases. Ferguson et al. (2016) and Newcombe et al. (2020a) treated starting volatile concentration as a free parameter in their models, and found that for a majority of their models, the best solution required a higher concentration than the highest measured value in their modeled embayments. Thus, using high volatile concentration plateaus in embayments as starting conditions can be problematic. If the initial high water content was lost via diffusion, even without a clear visual loss of plateau, using that water content as a proxy for starting pressure can increase DRM by a factor of 2-3 for geometries well-approximated by 1D models and by a factor of as much as 10 for geometries poorly approximated by 1D models.

Table 2.4. Summary of different starting conditions models

Geometry[a]	Max Embayment Water (wt. %)	P_i (MPa)	Imposed dP/dt (MPa/s)	Modeled dP/dt (MPa/s)	DRM[b]
Cylinder	5.94	198	1.8	1.89	1.05
Cylinder	5.83	192	1	1.20	1.20
Cylinder	5.55	175	0.5	0.767	1.53
Cylinder	4.36	115	0.1	0.204	2.04
Cylinder	2.73	50	0.01	0.021	2.13
20% Necked	5.94	198	0.75	0.899	1.20
20% Necked	5.87	193	0.5	0.700	1.40
20% Necked	5.71	184	0.3	0.513	1.71
20% Necked	5.07	150	0.1	0.241	2.41
20% Necked	3.27	69	0.01	0.030	3.00
40% Necked	5.95	198	0.75	1.21	1.61
40% Necked	5.89	195	0.5	0.962	1.92
40% Necked	5.77	188	0.3	0.743	2.48
40% Necked	5.24	159	0.1	0.399	3.99
40% Necked	3.47	77	0.01	0.051	5.13
60% Necked	5.93	197	0.5	1.51	3.03
60% Necked	5.88	194	0.35	1.37	3.91
60% Necked	5.82	191	0.25	1.20	4.82
60% Necked	5.76	187	0.2	1.14	5.68
60% Necked	5.66	182	0.15	1.02	6.79
60% Necked	5.50	173	0.1	0.850	8.50
60% Necked	3.89	94	0.01	0.154	15.4
80% Necked	5.96	199	0.5	2.39	4.77
80% Necked	5.93	197	0.25	2.19	8.74
80% Necked	5.91	196	0.2	2.07	10.35
80% Necked	5.81	190	0.1	1.91	19.10
80% Necked	5.76	188	0.08	1.83	22.83
80% Necked	5.63	180	0.05	1.63	32.65
80% Necked	5.50	173	0.03	1.47	49.04
80% Necked	4.88	140	0.01	0.812	81.10
80% Necked	4.35	115	0.005	0.470	94.06

[a]All models have the same final pressure of 20 MPa

[b]Decompression Rate Multiplier - see text for definition

Because relative timing of inclusion and embayment formation can be difficult to determine, we suggest measuring water content at the back of many embayments with similar length but variable geometries to determine if it is suitable to use as a constraint for starting

conditions. As seen in our 0.01 MPa/s runs, the maximum water content in the back of the different embayment geometries varied from 2.7 wt. % in the cylindrical embayment to 4.9 wt. % in the most necked embayment (Table 2.4). These embayments all have similar lengths and experienced the same diffusion timescale, so the discrepancy in water content is only a function of the different geometries. In the case of similarly sized embayments with variable maximum water contents, these water contents should be treated with caution as a starting condition. For the faster decompression rates in which the diffusion front has not reached the back of the cylindrical embayment (as evidenced by a DRM of ~1), the maximum water content at the back of each embayment geometry is the exact same. Thus, measuring water content in multiple similarly sized embayments can offer guidance about starting conditions. Longer embayments are also more likely to preserve the initial maximum water content. When present, concentrations of CO_2 and/or S can provide additional constraints on the formation pressure of the embayment (e.g., Ferguson et al., 2016; Lloyd et al., 2014; Newcombe et al. 2020a). Alternatively, starting conditions can be left as a free parameter during modeling, with guidance from melt inclusion measurements.

One additional complication with starting conditions that we did not address in this study is the influence of any pre-exsolved volatile fraction on degassing. Both Ferguson et al. (2016) and Newcombe et al. (2020a) incorporate a pre-existing exsolved volatile fraction in their models, which impacts the exsolution of the pre-existing volatiles from the embayment into the associated vapor bubble at the mouth of the embayment. For the basaltic systems that these studies examine, CO_2 profiles were the most impacted by the inclusion or exclusion of these exsolved volatiles. Generally, increasing the fraction of exsolved volatiles shifted the best-fit decompression rate to faster rates (Ferguson et al., 2016). For both Ferguson et al. (2016) and

Newcombe et al. (2020a), fits to their profiles were improved by inclusion of exsolved volatiles in the models. Thus, whether a magma contained exsolved volatiles prior to decompression should be an important consideration for future modelers.

2.5.3 Recommendations for Best Modeling Practices

Based on the modeling results and discussion presented in the previous sections, we will summarize here the best modeling practices for future users of MEM to avoid introducing modeling errors.

(1) 1D models can be used reasonably (DRM <2) for all geometries when the diffusion front is still close to the necked region. The decompression rate value to which that corresponds will depend on the diffusivity of the volatile of interest and the length of the necked region.

(2) 1D models can be used reasonably (DRM <2) for all decompression rates as long as the constriction on the embayment is ≤40%.

(3) 1D models cannot be used for embayments with constrictions >40% if the diffusion front is within the main body of the embayment.

(4) MEM should not be used for eruptions in which the magma has undergone disequilibrium degassing, unless a disequilibrium degassing pathway can be defined. Determination of equilibrium vs disequilibrium degassing is a critical first step when selecting eruptions with which to use MEM.

(5) Initial volatile concentration is difficult to determine, but surveying the highest concentration in several embayments and/or measurement of other volatiles can provide guidance as to whether melt inclusion values or embayment values are the better choice.

2.6 Conclusions

Melt embayment modeling (MEM) is gaining popularity as a method to calculate magma decompression rate, a historically difficult parameter to determine despite its importance for eruption dynamics. This study examined the impact of diffusion model simplifications on calculated decompression rate, relative to the true decompression rate. We tested the impact of isentropic ascent, disequilibrium degassing, and 3D embayment geometry. Our results indicate that isentropic ascent can be simplified as isothermal ascent with relatively little consequence. Disequilibrium degassing is an important but poorly defined parameter, though the overall role it plays in explosive eruptions is currently not well constrained. Most importantly, embayment 3D geometry can impart large errors in decompression rates calculated from 1D models if the embayment has a constriction near the mouth.

Chapter 3. Experimental Examination of Coordinated Decompression Rate Meters

3.1 Abstract

Quantification of magma decompression rate for volcanic eruptions is a high priority as decompression rate plays a major role in modulating volcanic eruption style. Many of the tools to calculate decompression rate from natural samples leverage textural and petrologic "fingerprints" left behind in the form of vesicles, crystal textures, and concentration gradients of volatiles (e.g., H_2O, CO_2). These meters are suitable for quantifying either fast or slow decompression rates, and typically are used to infer an average decompression rate, despite the knowledge that decompression is almost never constant during ascent to the surface. In the past, decompression rate meters have largely been used independently of each other, but recent advances have advocated use of multiple decompression rate meters in the same study to quantify better the range of decompression rates that occur during an eruption. In the present study, I conduct high pressure/high temperature decompression experiments that utilize two decompression rate meters (bubble number density and diffusion modeling) within the same experimental charge to examine whether the two rate meters reproduce the same decompression conditions and to assess what assumptions must be made to reproduce the known imposed decompression rate. The results indicate that both decompression rate meters can generally reproduce an experimentally imposed constant decompression rate, though the bubble number density-derived rate is more sensitive to heterogeneities within the starting material. Generally, assuming homogeneous nucleation resulted in the closest approximation of the known (imposed) decompression rate. Diffusion modeling results are also sensitive to the timing of bubble formation, as bubbles are needed for volatile concentration gradients to form. These experiments are the first step towards assessing the use of multiple decompression rate meters to characterize magma ascent

characteristics within a single eruption. Further studies should target experiments with variable decompression rate to determine whether the two decompression rate meters record different values, as eruptions are expected to experience non-constant decompression rates.

3.2 Introduction

Magma decompression rate is a critical parameter that modulates volcanic eruption style (Cassidy et al., 2018; Cashman and Sparks, 2013). It influences many processes that occur in the conduit, such as magma degassing and outgassing (e.g., Cassidy et al., 2018), decompression-induced crystallization (e.g., Hammer and Rutherford, 2002), and the strain rate needed to cross the glass transition (e.g., Webb and Dingwell, 1990; Dingwell, 1996). Many models of conduit dynamics rely on accurate estimates of decompression rate in order to produce meaningful results (e.g., Diller et al., 2006; Clarke et al., 2007). Due to the importance of decompression rate, several methods to estimate it have been developed. Some of the more common methods utilize bubble number density (Toramaru, 1995; 2006), hydrous mineral reaction rims (Nicholis and Rutherford, 2004; Rutherford, 2008; Rutherford and Devine, 2003; Rutherford and Hill, 1993), microlite textures (Andrews, 2014; Castro and Gardner, 2008; Couch et al., 2003; Szramek, 2016; Toramaru et al., 2008), and numerical modeling of ascent in the conduit (Kaminski and Jaupart, 1997; Papale and Dobran, 1993; Papale et al., 1998). Each is generally suited to resolve either fast or slow decompression rates, but not the entire range (Shea, 2017).

Magma decompression is almost never constant; exsolution of volatiles as a fluid phase during decompression increases the buoyancy of the magma and results in acceleration at lower pressures (Gonnermann and Manga, 2007; Su and Huber, 2017). Therefore, different decompression rate meters can be leveraged to probe different stages of decompression during an eruption (e.g., Myers et al., 2021). This integrated approach is a relatively new approach, as

many previous studies have only used one decompression rate meter, but it offers greater insights into shifts in eruption dynamics. Diffusion modeling is well-suited to probing the earlier, slower stages of decompression, whereas bubble number density tends to reflect the final, faster stages of decompression (e.g., Shea, 2017).

The flexibility of diffusion modeling allows its use in many contexts to probe decompression timescales. Previous studies have used diffusion of volatiles in melt inclusions (e.g., Myers et al., 2019), melt embayments (e.g., Ferguson et al., 2016; Humphreys et al., 2008; Liu et al., 2007; Lloyd et al., 2014; Myers et al., 2016; 2018; Newcombe et al., 2020a), and crystals (e.g., Barth et al., 2019; Newcombe et al., 2020a) to calculate magma decompression rate. By changing the species of interest, a wide range of timescales can be targeted (e.g., Chakraborty, 2008; Costa et al., 2020). However, many of the errors associated with the assumptions tested in Chapter 2 are common to other diffusing systems, and these errors can obfuscate decompression rate trends in natural systems.

Bubble number density (BND) as a decompression rate meter has undergone much scrutiny and subsequent refinement since its initial proposal by Toramaru (1989). However, many questions still surround the use of this meter, particularly with respect to the style of bubble nucleation. As described in Chapter 2, bubbles can nucleate either homogeneously or heterogeneously, or even a combination of the two. The dominant style of nucleation significantly impacts the rate retrieved from BND (e.g., Shea, 2017; Hajimirza et al., 2021). Therefore, an experimental examination of this technique, in which an imposed decompression rate is a known parameter, is useful in probing the impacts of homogeneous vs heterogeneous nucleation on calculated decompression rates.

In this chapter, I conduct high pressure/high temperature decompression experiments on rhyolitic melts to assess the decompression rates retrieved by diffusion modeling and BND within the same experimental charge. The experiments are designed to contain regions in which bubbles are present before decompression, as well as regions in which bubbles are not present before decompression. The former is achieved by loading powdered starting material into Al_2O_3 tubes with pre-determined hole diameters of 250 or 500 μm; this setup is also intended to be analogous to melt embayments. Bubble free regions are achieved by including solid, vesicle-free obsidian cores of the same composition as the powder on either end of the alumina tubes. My results indicate that nucleation within the obsidian cores is predominantly homogeneous, though occasional heterogeneities within the starting obsidian influences nucleation. Diffusion-retrieved decompression rates are highly sensitive to the timing of bubble formation. Additionally, although the initial goal was to simulate melt embayments within the alumina tubes, the 2D distribution of bubbles within the "embayments" are unlike those found in natural embayments, and these bubbles also influence retrieved decompression rates. These combined results have implications for the application of these two decompression rate meters to natural products.

3.3 Methods

High pressure/high temperature decompression experiments were conducted at both the University of Hawai'i at Mānoa (UHM) and Laboratoire Magmas et Volcans, Université Clermont, Auvergne, France (LMV). The main difference between the two facilities is that the LMV facilities allow for a rapid quench of samples and contain an apparatus for computer-controlled decompression, which is optimal for slow decompression rates (<0.2 MPa/s). Products of all experiments were analyzed at UHM using reflected light microscopy for BND and bubble textures and Raman spectroscopy for water measurements.

3.3.1 Experiment Methods

The decompression experiments were conducted using rhyolitic obsidian from Güney Dağı, Turkey (<1 vol. % crystals and 76.51 wt. % SiO_2; Mourtada-Bonnefoi and Laporte, 2002), both in powdered form and as cores, as well as alumina (Al_2O_3) tubes with boreholes of set inner diameter (500 and 250 μm). Powder was loaded into the larger diameter boreholes by carefully pouring powder (~50 μm grain size) and periodically tapping to compress the powder. The smaller diameter boreholes were loaded with powder (<10 μm grain size) with the aid of a vacuum pump. The alumina tubes loaded with powder were then nested into larger diameter alumina tubes to provide additional stability during the experiment (Fig. 3.1). This nested tube setup was then capped with cores of obsidian on both ends to prevent powder from leaving the synthetic embayments. The assembly was then carefully loaded into 4 mm Ag or $Ag_{70}Pd_{30}$ tubes with enough deionized water to saturate both the powder and the cores. Capsules were welded closed on both ends

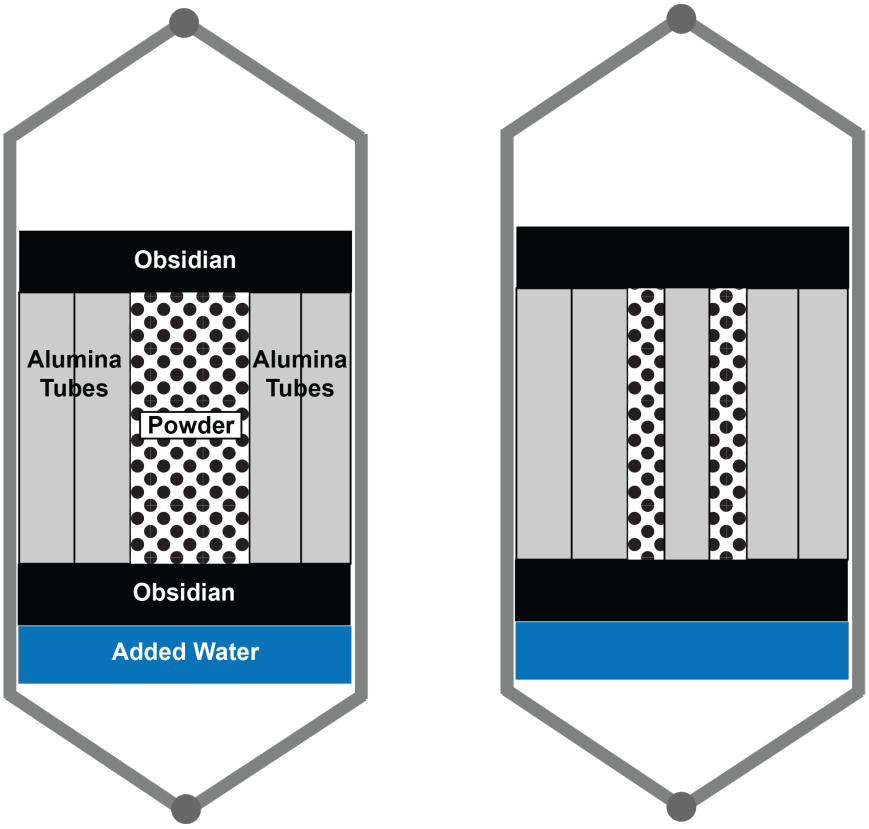

Figure 3.1. Schematic of different experiment capsule setups. The different regions are labeled with the material of which they are comprised, and is the same for both setups. The difference between the two setups is the diameter of the alumina tube holes.

using an arc welder, and the welds were tested by heating the capsules at 150 °C for at least 15 minutes. For capsules saturated on a gas-pressurized line, the welded 4 mm capsules were loaded into 5 mm $Ag_{70}Pd_{30}$ outer capsules, which were packed with a mixture of Ni and NiO powder, as well as water, to buffer the experiments to the NNO buffer. This outer capsule was also welded closed and checked for leaks using the same method. At the end of experiments, the buffer mixture was examined to ensure that neither powder was completely exhausted.

Leak-free capsules were loaded into either Nimonic or Waspalloy cold-seal pressure vessels. Capsules saturated on the water-pressurized line had a Ni rod inserted into the vessel with them to buffer the experiments to the NNO buffer. Experiments were cold-pressurized to 200 MPa with either water or N_2, then heated to 800 °C. Pressure was monitored during heating to ensure that it did not exceed 200 MPa. Experiments were held at 800°C and 200 MPa for five days to ensure homogeneous distribution of water in all starting material. Then experiments bound for decompression at LMV were quenched with compressed air and water. When necessary, inner capsules were extracted from the outer buffer capsules, and all capsules were weighed to ensure no holes occurred during saturation. Experiments that were decompressed at UHM were not quenched prior to decompression. Instead, at the end of the saturation period, pressure was

Table 3.1. Summary of experiments and conditions

Experiment Name	Embayment Diameter (µm)	dP/dt (MPa/s)	P_i (MPa)	P_f (MPa)	Quench Facility
RDGD250-4	500	0.5	200	50	LMV
RDGD250-8	500	0.01	200	50	LMV
RDGD250-13	500	0.2	200	50	UHM
RDGD250-14	500	0.5	200	50	UHM
RDGD250-15	500	1	200	50	UHM
RDGD125-2	250	0.5	200	50	UHM
RDGD125-3	250	0	200	200	LMV
RDGD125-7	250	0.01	200	50	LMV
RDGD125-12	250	1	200	50	UHM
RDGD125-13	250	0.2	200	50	UHM

carefully bled from the system at the desired rate by hand using a leak valve and a stopwatch. Once the pressure reached 50 MPa, the experiments were quenched with compressed air and water. Typical quench times were ~30-45 seconds after decompression ceased. Pressure was modulated during the quench to ensure it did not drop below 50 MPa before the pressure vessel was submerged in water. The relatively high quench pressure was chosen to ensure that the hydration bubbles in the embayment did not grow so large as to displace all of the melt from the embayment.

Decompression experiments that were carried out at LMV were loaded into a Nimonic pressure vessel fitted with a rapid quench assembly, and heated and pressurized with N_2 to 800 °C and 200 MPa. Experiments were held at these conditions for 15 minutes to resorb any bubbles or crystals that formed during the previous quench. After the hold period, experiments were decompressed, either by hand or by an automated program, at different rates to a final pressure of 50 MPa and quenched rapidly. For decompressions by hand, pressure was carefully bled from the system via a leak valve and timed to ensure the correct rate of bleeding. For decompressions by automated program, a computer controlled a series of valves that automatically removed a given volume of pressurizing gas at varying time intervals (Mourtada-Bonnefoi and Laporte, 2004). The automatic decompression was preferred for longer duration decompressions as the program provided more reproducible decompression pathways. Once the desired final pressure was reached, the experiment was quenched by dropping the experiment into a water-cooled region of the pressure vessel, cooling below the glass transition temperature in <2 seconds (~200 °C/s). Quenched glasses were carefully extracted from the 4 mm capsules and prepared for subsequent analyses (Table 3.1).

3.3.2 Analytical Methods

Raman spectroscopy was used to measure water both inside the embayments and in the vesiculated obsidian. I double-polished the experimental products to minimize spectral interference of the parasitic crucible Al_2O_3 peak with the water (molecular H_2O) peak from the hydrous rhyolite glass. Water concentration was determined by using the ratio of area under the water (3000 – 3800 cm^{-1}) peak to the area under the aluminosilicate structure (200 – 1270 cm^{-1}) peak (Le Losq et al., 2012; Shea et al., 2014). This method accounts for fluctuations in the laser between different analyses as it uses a ratio rather than the absolute magnitude of the peaks.

Raman analyses were conducted at the University of Hawai‘i at Mānoa, using a Witec Alpha300R confocal microscope and green (i.e., 532 nm wavelength) laser. Spectra were collected at 1 μm spots over five iterations with 20 second counting time per iteration. Processing of spectra was done with the “SpeCTRa” (Spectral Correction Tools for Raman) Matlab code (Shea et al., 2014). This code allows for background subtraction and calculation of peak areas. Generally, five spots in the obsidian regions of experiments were collected. For experiments with optimal melt-filled embayments, profiles were collected starting at a melt-vapor interface and ending at either another melt-vapor interface, or when a plateau in water concentration was recorded. Inter-bubble profiles in the obsidian region were chosen between similarly-sized bubbles to ensure that the bubbles nucleated at similar times. For both inter-bubble and embayment transects, the glass below the polished surface was examined to ensure no nearby bubbles could influence water content. Profiles were collected with step sizes of 5-20 μm, depending on the total length of the profile.

The vesiculated obsidian core regions were polished and imaged on a microscope using reflected light. Obsidian core pieces that detached from the alumina during extraction were polished to produce radial sections, and series of images were captured during iterative polishes

to expose different regions of the obsidian. Obsidian pieces that remained attached to the alumina were cut and polished length-wise with the alumina, and only the final exposure of bubbles was imaged after polishing the alumina appropriately for Raman analysis. Generally only one or two magnifications were used to image the samples as bubble sizes did not vary significantly. Captured images were processed in Adobe Photoshop such that vesicles were a different grayscale value from the glass and crystals. Where visible, coalesced bubble walls were redrawn to "decoalesce" bubbles in the processed image so that BNDs are not reduced by coalescence. Processed images were loaded into FOAMS (Shea et al., 2010) to calculate BND, vesicularity, and modal bubble size. Only bubbles that were larger than 10 μm in diameter were counted in the analysis. Following Toramaru (2006), decompression rate (*dP/dt*) in Pa/s is calculated from BND (N_v) in m^{-3} using:

$$N_v = 34 n_0 \left(\frac{16\pi\sigma^3}{3k_B T P_{sat}^2}\right)^{-2} \left(\frac{V_{H2O} P_{sat}}{k_B T}\right)^{-1/4} \left(\frac{P_{sat}^2 k_B T n_0 D_{H2O}}{4\sigma^2 \left|dP/dt\right|}\right)^{-3/2} \quad (3.1)$$

where n_0 is the initial number of water molecules per unit volume melt, k_B is the Boltzmann constant, D_{H2O} is water diffusivity in $m^2\ s^{-1}$, V_{H2O} is the volume of a water molecule in m^3, σ is the melt-vapor interface surface tension in $N\ m^{-1}$, P_{sat} is the H_2O saturation pressure in Pa, and T is temperature in K.

3.3.3 Diffusion Modeling

Diffusion modeling was conducted by solving the concentration-dependent version of Fick's Second Law in 1D using a finite differences approach described in Chapter 2. The best-fit profile was determined using the same weighted RMSD approach as in Chapter 2. I assumed water homogenously distributed throughout the melt at the equilibrium water concentration at

experiment initial pressure, according to the solubility model of Liu et al. (2005). At the final pressure, the water concentration at the bubble edge(s) was assumed to be equal to the equilibrium value, and that value was used in the RMSD calculation. For profiles that had bubbles at both ends, the boundary condition was set such that each melt/vapor interface index in the finite differences calculation had a water concentration equal to the equilibrium saturation value for a given pressure step. Diffusion then proceeded in both directions over the duration of the model, with diffusivity calculated using the model of Ni and Zhang (2008). For profiles with a water concentration plateau and a vapor bubble at only one end, the vapor bubble boundary was the same as previously described, and the index at the end of the plateau was set at the value of the adjacent index at each time/pressure step. Thus, the plateau could decrease in value, given a sufficiently long diffusion time.

3.4 Results and Interpretations

3.4.1 Vesicularity and water content in the obsidian

Vesicularity within the obsidian region of the experiments is too low compared to values predicted at equilibrium for all decompressed experiments (Fig. 3.2a). In general, the degree to which the measured vesicularity differs from the expected equilibrium value is a function of decompression rate. Faster decompression rates tend to produce a larger deviation from equilibrium, and vice versa (Table 3.2). The experiment that was quenched without decompression has a minor population of very small bubbles, but they account for <1 vol. %. However, these vesicles have important implications for the experiment results, as discussed later.

Experiments are all supersaturated with regard to water (Fig. 3.2b). As with vesicularity, faster decompression tends to produce higher degrees of water supersaturation (Table 3.2). One

experiment, RDGD125-13, has anomalously low vesicularity as compared to the other experiments with similar or faster decompression rates, though its dissolved water content is correspondingly greater. The modal bubble size is also much smaller than the other experiment with a similar decompression rate (Table 3.2). Potentially, nucleation was later for this sample, resulting in smaller bubbles and higher dissolved water content.

Table 3.2. Water and vesicularity measurement results

Experiment	Imposed dP/dt (MPa/s)	P_f (MPa)	Dissolved Water (wt. %)[a]	Vesicularity (vol. %)	BND (mm^{-3})	Modal Bubble Size (mm)	N[b]
RDGD250-4	0.5	50	n.d.[c]	22	16562	0.035	482
RDGD250-8	0.01	50	n.d.	23	1199	0.022	133
RDGD250-13	0.2	50	4.1 (0.6/0.6)	21	338	0.137	153
RDGD250-14	0.5	50	5.1 (0.5/0.4)	21	287	0.139	171
RDGD250-15	1	50	5.3 (1/0.4)	7.8	163	0.087	184
RDGD125-2	0.5	50	3.8 (0.5/0.3)[d] 4.5 (0.2/0.4)[e]	15	2159	0.055	242
RDGD125-3	0	200	5.6 (0.2/0.3)	0	0	n/a	n/a
RDGD125-7	0.01	50	n.d.	28	235	0.137	156
RDGD125-12	1	50	5.3 (0.2/0.2)	11	82	0.109	107
RDGD125-13	0.2	50	5.4 (0.6/0.3)	6.6	211	0.087	153

[a]Values in parentheses are (+/-) the range of values measured in each experiment

[b]Number of bubbles measured

[c]n.d. - no data

[d]Water content measurement in bubble-rich region (Fig. 3.3b)

[e]Water measurement in bubble-poor area (Fig. 3.3b)

3.4.2 Bubble and crystal textures

The glass is generally crystal-poor, though small oxides are numerous in all samples, regardless of any outside influence on quench rate from the decompression facility. Experiments decompressed at UHM have rare small (<5 μm) feldspar crystals, likely from cooling-induced crystallization during the slower quench.

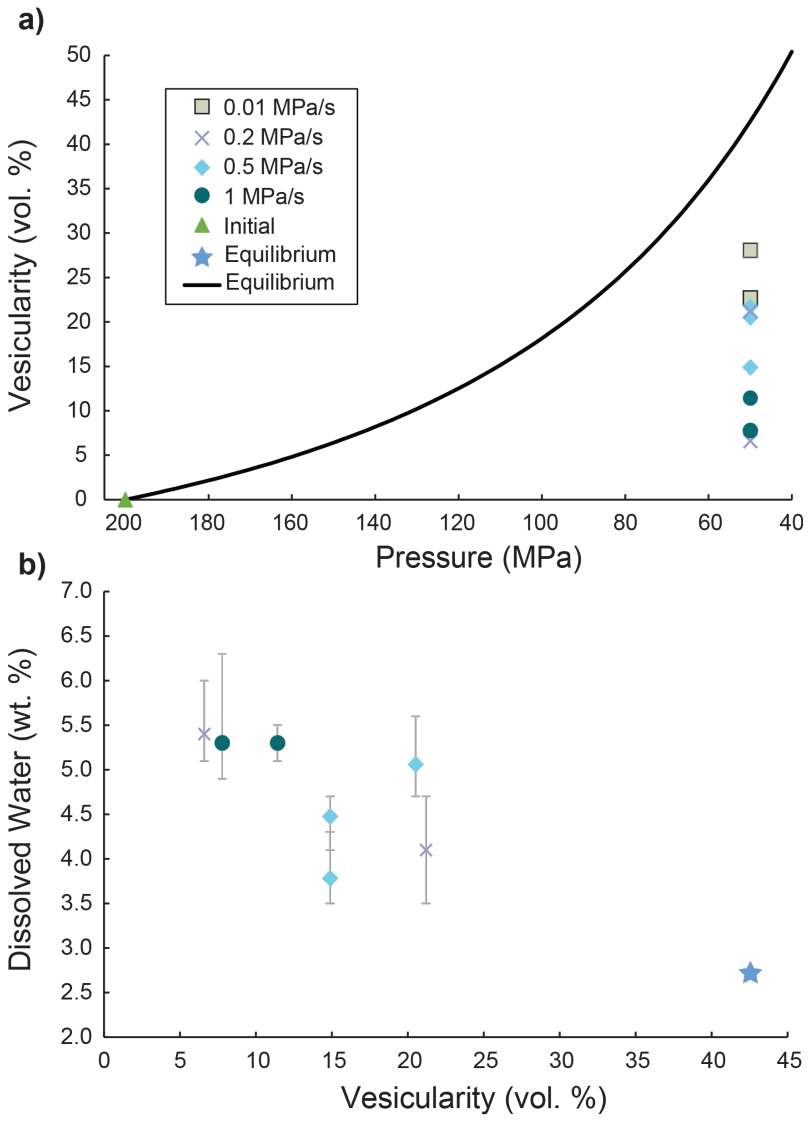

Figure 3.2. Plots of dissolved water content and vesicularity measured in the experiments. *a)* vesicularity tends to be higher in experiments with slower decompression rates, though all experiments measured have lower vesicularity than the equilibrium value. The equilibrium vesicularity line is calculated using the model of Gardner et al. (1999). *b)* dissolved water content is generally higher in experiments with lower vesicularity and is a function of decompression rate. However, all experiments are supersaturated with respect to the expected equilibrium water content and vesicularity at 50 MPa. Error bars show the spread of water contents measured within a sample. The two data points at 15 vol. % vesicularity are two measurements made in the bubble-rich (lower water content) and bubble-poor regions (higher water content) of the experiment shown in Fig. 3.3b

Bubble textures differ between regions that have powder-derived melt (i.e., the embayment) and regions that have obsidian-derived melt (Fig. 3.3e). The obsidian regions start out largely vesicle-free, whereas embayment regions start out with hydration bubbles, as well as air pockets where powder did not fully pack into the embayment. Because the embayment vesicles are present at the start they are generally larger than later nucleated bubbles in the obsidian region. Additionally, many of the hydration bubbles

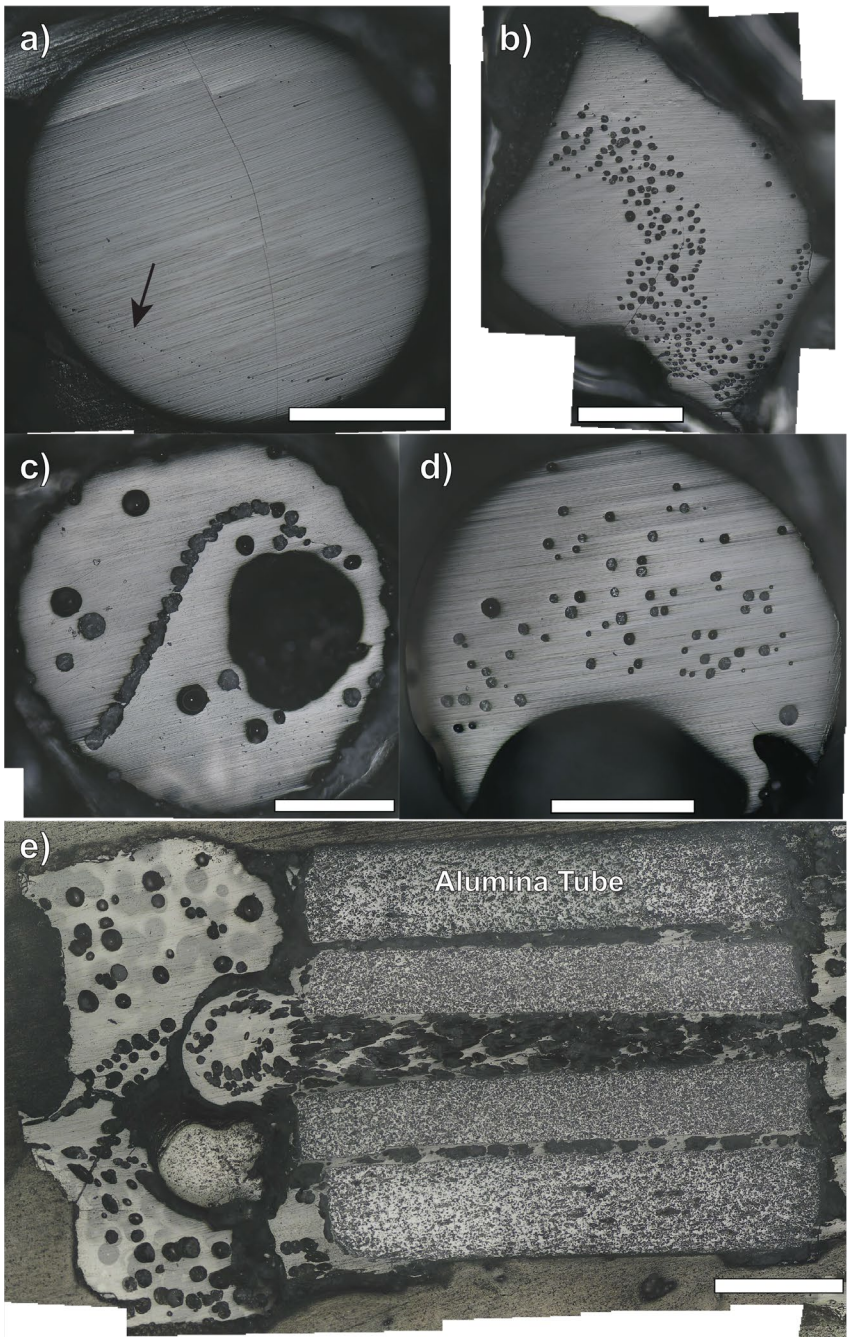

Figure 3.3. Examples of different textures present in the experiments. *a) – d)* are radial sections that show bubble textures in the obsidian, whereas *e)* shows the different textures in the embayment and the obsidian from experiment RDGD250-14. *a)* shows the experiment that was quenched with no decompression. Black arrow points to incipient bubble chain. *b)* Shows the "uneven distribution" bubble texture, *c)* shows the "bubble chain" texture, and *d)* shows the "even distribution" texture. In both *c)* and *d)* a very large bubble can be observed, though it is only observable in *d)* as the void space that creates the crescent moon shape of the glass. The scale bars in each image are 1 mm.

are elongated and coalesced, presumably from expanding against the rigid alumina wall.

Within the obsidian region, three different distributions of bubbles are observed. Most of the experiments have a random distribution of bubbles, and bubbles have no discernable tendency to group in a region of the sample (e.g., Fig. 3.3d). One experiment has an uneven distribution of bubbles in which bubbles are clustered in a region of the obsidian (e.g., Fig. 3.3b). Finally, some experiments also display bubble curtains

in which long chains of coalesced bubbles are observed, with few bubbles outside the chain(s) (e.g., Fig. 3.3c). Almost all of the experiments also have a single very large vesicle in the obsidian region. It is difficult to quantify the exact size of the vesicle as it causes the shape of the obsidian to become irregular, so polishing perpendicular to it is challenging. The scale of the bubble is also generally larger than can be captured by the lowest magnification objective on the used microscope. However, vestiges of this bubble can occasionally be seen in the polished surfaces (Fig. 3.3). Potentially this large vesicle results from the large amount of void space (i.e., ambient air) typically within the embayment region escaping during decompression. This large vesicle was excluded from the sample area and not counted during BND calculation.

3.4.3 Bubble number density and subsequent derived decompression rates

Bubble number densities in the experiments span several orders of magnitude, ranging from the order of 10^1 to 10^4 mm^{-3} (Table 3.2; Fig. 3.4). For experiments that experienced the same decompression rate, the variation in BND between experiments is typically less than an order of magnitude. The only exception is the experiments decompressed at 0.5 MPa/s; these experiments vary in

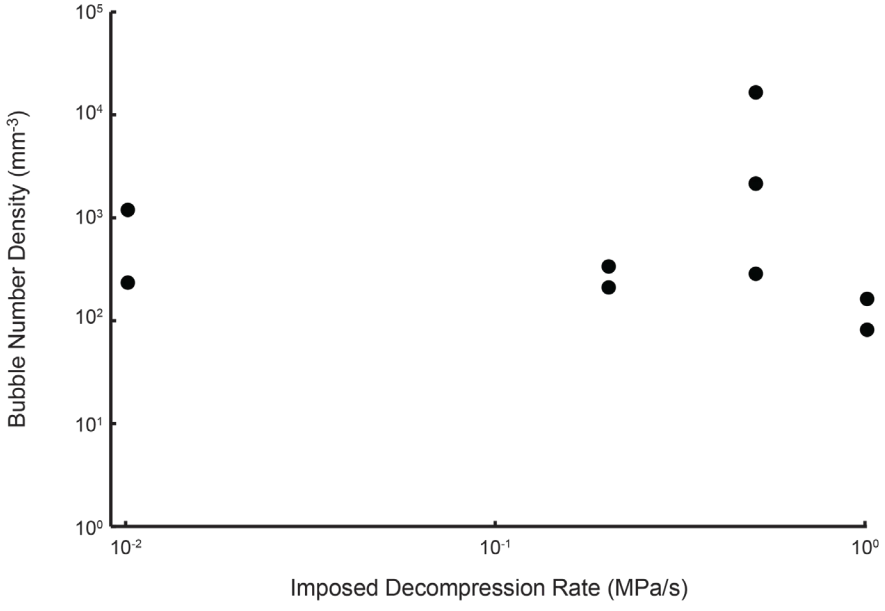

Figure 3.4. Relationship of measured BND with decompression rate. Most of the decompression rates display similar BNDs for the same decompression rate, with the exception of experiments decompressed at 0.5 MPa/s. The experiments decompressed at 1 MPa/s are also systematically lower in BND than the other decompression rates.

BND by more than two orders of magnitude. In principle, faster decompression rates should produce greater bubble number densities. However, the fastest decompression rate (1 MPa/s) produces the smallest BNDs in the experiment suite (Fig. 3.4). The two experiments that experienced the fastest decompression rate are also the two experiments that have bubble chains, so it seems that the bubble texture impacts BND. Thus, the results of the BND-derived decompression rate calculations are grouped by the observed bubble texture. Although the decompression rates experienced by these experiments span three orders of magnitude, there is not significant variation in BND between rates. Potentially, this could be the result of similar processes that produce the different textures, or this could be the result of too few bubbles within the experimental charge to resolve the differences.

Table 3.3. Bubble textures and BND-derived decompression rates

Experiment	Imposed dP/dt (MPa/s)	Bubble Texture	Heterogeneous dP/dt (MPa/s)[a]	Homogeneous dP/dt (MPa/s)[b]
RDGD250-4	0.5	random distribution (many small bubbles)	0.247	3.950
RDGD250-8	0.01	random distribution	0.043	0.686
RDGD250-13	0.2	random distribution	0.018	0.295
RDGD250-14	0.5	random distribution	0.017	0.264
RDGD250-15	1	bubble curtain	0.011	0.181
RDGD125-2	0.5	uneven distribution	0.063	1.015
RDGD125-3	0	bubble curtain	0.000	0.000
RDGD125-7	0.01	random distribution	0.014	0.231
RDGD125-12	1	bubble chain	0.007	0.115
RDGD125-13	0.2	random distribution	0.013	0.215

[a]Uses σ=0.02 N m^{-1}

[b]Uses σ=0.08 N m^{-1}

To examine the dominant bubble nucleation style within the experiments, BND-derived decompression rate for each experiment is calculated using a surface tension appropriate for titanomagnetite-assisted nucleation (σ=0.02 N m^{-1}) and homogeneous nucleation (σ=0.08 N m^{-1}).

The different surface tension values produce decompression rates that differ by almost exactly an order of magnitude for each experiment (Table 3.3). Calculated decompression rates range from 0.007 to 4 MPa/s, a greater range than used in the experiments.

Experiments that experienced the slowest decompression rate (0.01 MPa/s) are better fit by the heterogeneous nucleation surface tension value, though the rate is always overestimated, regardless of assumed nucleation style (Fig. 3.5). As described above, the experiments that experienced the fastest decompression rate have the lowest BND values, so neither surface tension value (and thus nucleation style) reproduces the imposed decompression rate; the decompression rate is wholly underestimated. Both experiments decompressed at 0.2 MPa/s

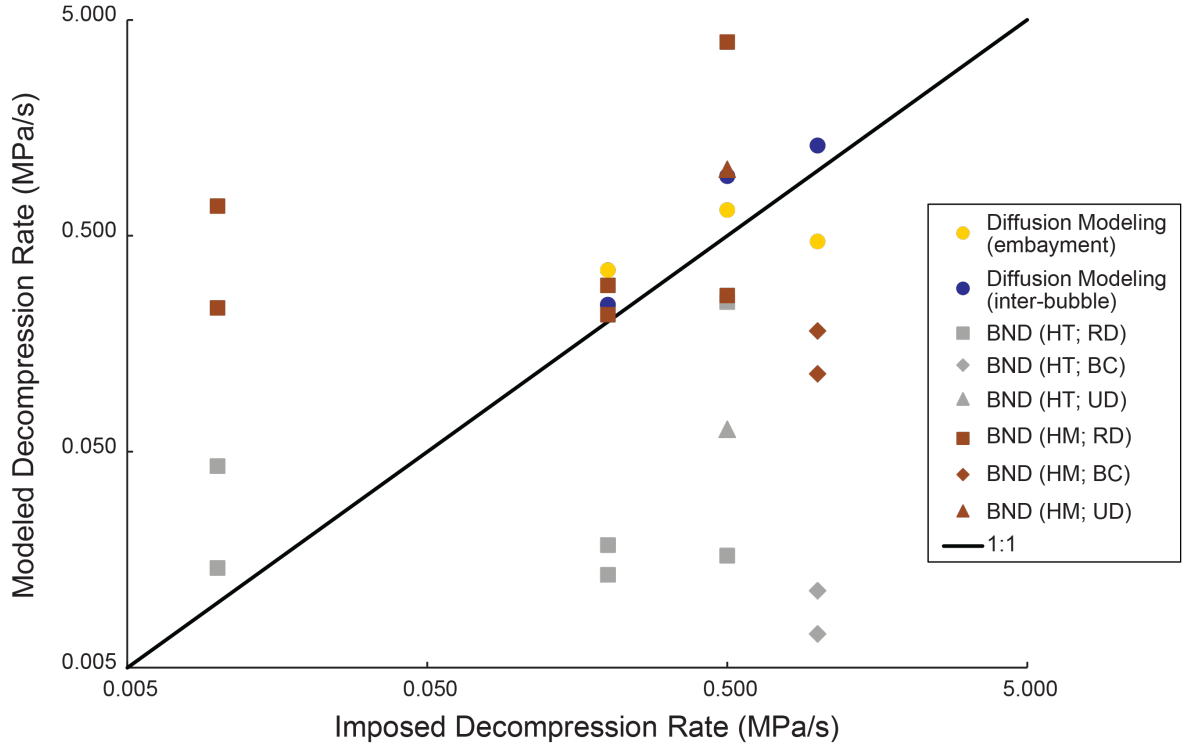

Figure 3.5. Plot of imposed decompression rate vs modeled decompression rate for the different methods used in this study. Results are differentiated between assumed nucleation style, observed bubble texture, and type of diffusion profile. BND = bubble number density, HT = assumed heterogeneous nucleation (i.e., σ=0.02 N m^{-1}), HM = assumed homogeneous nucleation (i.e., σ=0.08 N m^{-1}), ED = even distribution of bubbles, BC = bubble chains, and UD = uneven distribution.

decompression yield BNDs that are consistent with homogeneous nucleation. Two of the three experiments decompressed at 0.5 MPa/s contain BNDs that are neither perfectly consistent with fully heterogeneous or fully homogeneous nucleation; thus, they potentially experienced heterogeneous nucleation, but not assisted by titanomagnetite when considering the bubble textures (Table 3.3). One of these experiments has an uneven distribution of bubbles, so it is likely that the bubbles nucleated on some heterogeneity within the obsidian, but it was not as energetically favorable as titanomagnetite. The final experiment conducted at 0.5 MPa/s decompression was not well-approximated by either surface tension value; the modeled decompression rates are lower for both nucleation modes. Although two of the experiments that experienced 0.5 MPa/s decompression had a similar texture of evenly distributed bubbles, the modal bubble size between them is very different. The experiment with smaller bubbles has a larger BND, whereas the experiment with larger bubbles has a smaller BND. These two experiments were also performed at two different facilities, so the differences between the two could be related to differences in the facilities. At LMV, experiments were not fugacity-buffered during decompression, only hydration, so slight oxidation from H^+ loss from the capsule could have facilitated the nucleation of titanomagnetite partway through decompression. This would then have facilitated the nucleation of a large number of small bubbles.

3.4.4 Diffusion modeling and subsequent derived decompression rates

Three experiments contained optimal locations for profiles both within the embayment and in the obsidian. These experiments cover three of the four decompression rates in this study, excluding the 0.01 MPa/s rate. Most of the profiles showed some amount of disequilibrium with respect to the water concentration measured nearest the bubble edge (Fig. 3.6). Embayment profiles tended to be undersaturated relative to the imposed final pressure, whereas inter-bubble

profiles in the obsidian region tended to be supersaturated. However, collecting spectra directly on the bubble edge was challenging, so modeling proceeded with the assumption of equilibrium directly at the bubble wall, as described in the Methods.

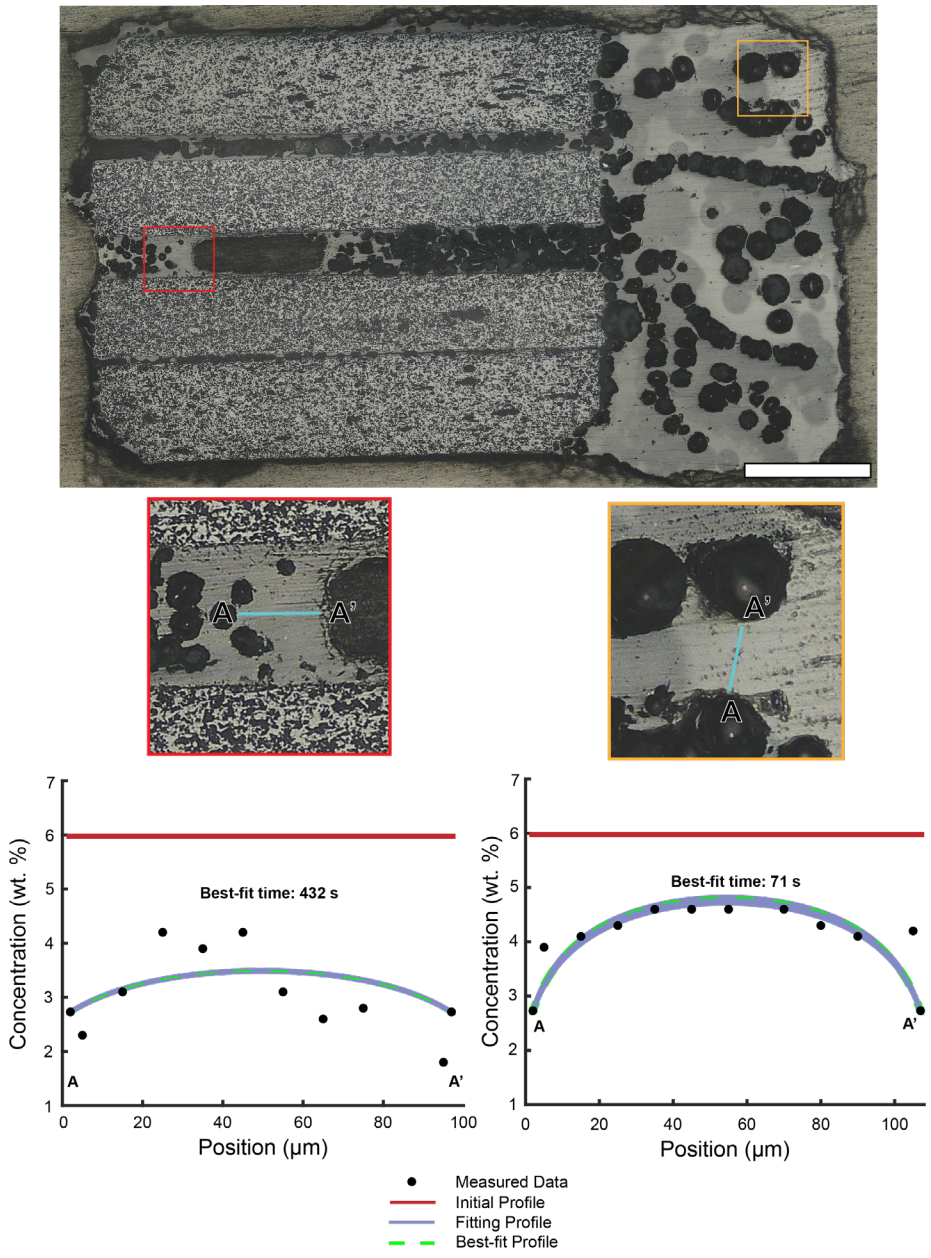

Figure 3.6. Example of measured profiles and their location within the sample for experiment RDGD250-13. The fitting profiles that are +/- 5 seconds from the best fit time are also shown on the plots. Data points at each edge of the profile are the assumed water concentration, if the edge of the bubble is at equilibrium. Scale bar is 1 mm.

Modeled decompression rates within embayments are generally quite close to the imposed decompression rate (Table 3.4). The largest difference between the modeled and the imposed decompression rates occurs for experiment RDGD250-15, with a modeled decompression rate that is slower by a

factor of two. The other two experiments have slight overestimations of the imposed decompression rate. Likely the deviation in RDGD250-15 is a result of the 2D distribution of bubbles. Although the profile has a plateau in water concentration, there are chains of bubbles along the walls of the embayment that likely influence the diffusion of water. The 1D modeled rate is likely longer than the imposed rate due to extra diffusive loss to the bubble chains that is not accounted for in the 1D model.

Table 3.4. Diffusion modeling results

Experiment	Transect Type	Imposed dP/dt (MPa/s)	Total Imposed Decompression Time (s)[a]	Modeled timescale (s)	Modeled dP/dt (MPa/s)	Corrected Modeled dP/dt (MPa/s)[b]
RDGD250-13	embayment	0.2	780	432	0.35	n/a
RDGD250-13	inter-bubble	0.2	780	71	2.11	0.24
RDGD250-14	embayment	0.5	337	228	0.66	n/a
RDGD250-14	inter-bubble	0.5	337	18	8.33	0.94
RDGD250-15	embayment	1	170	319	0.47	n/a
RDGD250-15	inter-bubble	1	170	13	11.5	1.31

[a]Timescale includes time needed to quench sample, as well as decompression time

[b]Corrected decompression rate for when bubbles nucleated, assuming P_N=67 MPa

The modeled timescales from the inter-bubble profiles are significantly shorter than the corresponding timescales from the embayment profiles for all three experiments (Table 3.4). This is to be expected with the experiment design, given that the bubbles within the embayment should have existed at the very start of the decompression, whereas bubbles in the obsidian required some amount of time (and decompression) to form. Without the presence of bubbles, concentration gradients would not develop. Assuming that the bubbles formed at the start of decompression, or soon thereafter, yields unrealistically fast decompression rates (2-11 MPa/s) that are significantly different from the imposed rates.

Alternatively, decompression rate can be calculated relative to the pressure of bubble nucleation. Based on the results from the BND modeling, the experiments used for diffusion

modeling likely experienced homogeneous nucleation. This interpretation is complicated for RDGD250-15, as the bubble chain texture appears to have influenced nucleation. However, the inter-bubble profile was collected between bubbles not visibly associated with a bubble chain, thus, these bubbles likely experienced homogeneous nucleation similar to the other experiments. Therefore, I use the surface tension (σ) value of 0.08 N m^{-1} relevant to homogeneous nucleation with classical nucleation theory to approximate the nucleation pressure of the bubbles, and the corresponding initiation pressure for diffusion (e.g., Hirth et al., 1970; Cluzel et al., 2008; Shea, 2017):

$$J = J_0 exp\left(-\frac{16\pi\sigma^3}{3k_B T(P_B^* - P_M)^2}\varphi\right) \tag{3.2}$$

$$J_0 = \frac{2n_0^2 D_{H2O} V_{H2O}}{a_0}\sqrt{\frac{\sigma}{k_B T}} \tag{3.3}$$

Where J is nucleation rate, k_B is the Boltzmann constant, T is temperature, P_B* is the pressure in the bubble, P_M is the pressure in the melt, φ is the geometrical term that defines nucleation mechanism (for homogeneous nucleation, φ=1), n_0 is the concentration of water molecules per volume melt, D_{H2O} is the diffusivity of water at the melt-bubble interface, V_{H2O} is the volume of a water molecule in the melt, and a_0 is the separation between water molecules in the melt. Nucleation pressure (P_N) is determined by solving for the P_M at which the BND, as calculated by summing J at each pressure step for a decompression pathway, is equivalent to that measured in each experiment. For the three experiments, the difference in measured BND produces a difference in P_N of <1 MPa, so an intermediate value of 67 MPa is used for all three experiments as P_N. Calculating decompression rate as the difference between P_N of 67 MPa and quench

pressure of 50 MPa yields modeled decompression rates that are much more consistent with the imposed decompression rates (Fig. 3.5).

3.5 Discussion

3.5.1 Comparison with previous nucleation experiments and natural samples

Measured BNDs, vesicularity trends, and water supersaturation trends are similar to those obtained in other experimental studies by Cluzel et al. (2008) and Mourtada-Bonnefoi and Laporte (2004). For similar decompression rates and quench pressure, their BNDs range from 10^1-10^3 mm^{-3}, vesicularity ranges from 10-40 vol. %, and dissolved water ranges from 3-5 wt. %. They used the same starting material in their studies, as well as similar decompression rates. Thus, I assume the results of this study are robust and suitable for further interpretation.

The obtained BNDs, vesicularity trends, and water supersaturation trends are also similar to those found in other bubble nucleation studies in high silica melts (e.g., Gardner et al., 1999; Mangan and Sisson, 2000; Mangan et al., 2004). However, the fastest decompression rate (1 MPa/s) does not produce a similar order of magnitude of BND as the other studies, likely related to the influence of the bubble chain texture, as further discussed below. Except for these anomalous results, the measured BNDs overlap with the lower estimates of other studies.

Comparing with natural erupted rhyolite products, the BNDs and vesicularities are quite low (e.g., Klug and Cashman, 1994; Houghton et al., 2010; Myers et al., 2021). Potentially this is related to the high quench pressure of the experiments as compared to typical fragmentation pressures for eruptions. If homogeneous nucleation is the dominant mechanism in these experiments, as is suggested by the best-fit surface tension value in the BND decompression rate calculation (Fig 3.5), then late-stage nucleation should occur at lower pressure (e.g., Mangan and Sisson, 2000). Given the large degree of water supersaturation still present in the melt at 50 MPa,

it is possible that the experiments were interrupted during the main pulse of bubble nucleation. Further decompression of the experiments could have resulted in more nucleation that would have driven BNDs to values closer to those measured in natural products.

3.5.2 Influence of starting material on experiments

Powder as a starting material has long been known to produce different vesicle textures during decompression as compared to solid obsidian because pores in the powder favor the formation of hydration bubbles (e.g., Gardner et al., 1999; Preuss et al., 2016). Hydration bubbles form from trapped air and added water between powder grains that remain even when the powder forms a melt (Gardner et al., 1999; Larsen and Gardner, 2000). The pre-existing bubbles facilitate diffusive loss of water, rather than the energetically-challenging nucleation of new bubbles. Preuss et al. (2016) noted that in their experiments, hydration bubbles tended to disappear when the experiments were held at initial conditions >96 hours. Although the experiments in this study were held at initial conditions for 120 hours, hydration bubbles were still evident in the embayment regions (Fig. 3.3). Potentially, the cap of obsidian on either end of the embayment region prevented migration of hydration bubbles out of the embayment, as is the proposed mechanism for hydration bubble loss in Preuss et al. (2016). Alternatively, the high viscosity of the rhyolite melt in this study hindered bubble escape, as compared to the lower viscosities of the phonolite and trachyte melts used in the Preuss et al. (2016) experiments. However, in this study, the pre-existing bubbles were necessary to evaluate the impact of timing of bubble formation on diffusion modeling results. Certainly, diffusion timescales calculated from inter-bubble profiles are sensitive to the timing of bubble formation as the gradients do not form until the bubbles are present. As shown in Chapter 2, embayment profile timescales are also sensitive to timing of bubble formation.

Although solid obsidian cores are generally preferable to powder as starting material for bubble nucleation studies, nucleation can still be influenced by pre-existing heterogeneities within the obsidian itself, such as microcrystals or healed fractures (e.g., Shea, 2017). In these experiments, the bubble chain texture is likely an inherited feature from heterogeneities in the obsidian, rather than a primary nucleation phenomenon. An incipient bubble chain can be seen in the lower left corner of the experiment that experienced no decompression (Fig. 3.3). Examples were also noted in secondary electron images in Mourtada-Bonnefoi and Laporte (2002) and (2004). The products of experiments with this bubble texture were also bubble-poor in the glass regions not cut by the bubble chain(s). Thus, new bubble nucleation is likely influenced in these experiments by the presence of these chains. Potentially, they form an efficient route for gas escape and decrease the supersaturation of water in the melt enough that nucleation is not favored. Had the experiments been decompressed to lower pressures, the additional supersaturation could have been sufficient for nucleation to occur.

Heterogeneities within obsidian cores are often annealed out by superliquidus treatment (i.e., heating the experiment to >150-200°C above the intended experimental temperature) prior to holding the experiment at starting conditions (e.g., Mangan and Sisson, 2000; Iacono Marziano et al., 2007; Cichy et al., 2011). However, this superliquidus treatment is likely altering the silicate melt structure and influencing the results of subsequent nucleation studies (Shea, 2017). The fact that superliquidus treatment changes melt structure is most evident in crystal nucleation experimental studies (e.g., Walker et al., 1978; Donaldson, 1979; Sato, 1995; Pupier et al., 2008; Leonhardi et al., 2015). A relationship between duration of superliquidus treatment and bubble nucleation behavior was noted by Gardner et al. (1999), though no detailed studies have been conducted to date.

3.5.3 Nucleation style and requirements for accurate decompression rate retrieval

The power of experimental studies is that many of the parameters which are unknown in natural studies, such as decompression rate, are known and thus can be utilized to infer properties that otherwise require introducing simplifying assumptions, such as dominant nucleation style. In this study, bubble nucleation appears to be predominantly homogeneous, which governs the assumed surface tension for calculating decompression rate from BND and subsequently the P_N for the inter-bubble diffusion profile. However, given the noticeable presence of oxides in these experiments, a researcher who had no knowledge of the decompression rate would be likely to choose to assume heterogeneous nucleation (e.g., Hurwitz and Navon, 1994; Shea, 2017). Potentially, the number density of oxides was not sufficient in most experiments to impact the macro-scale observed BND, and thus nucleation proceeded homogeneously. More work is thus needed to quantify the number density of titanomagnetite crystals required to push nucleation into the heterogeneous regime, as well as relative timing of titanomagnetite and bubble formation during eruptions (e.g., McCartney et al., 2020). Recent work from Burgisser et al. (2020) shows that the critical threshold of titanomagnetite number density needed to impact bubble nucleation must be $>10^{11}$ m^{-3} for slow ascent (0.005 m/s), and this critical threshold is greater for faster ascent rates. Resolving these questions will provide guidance for future researchers that employ these decompression rate meters, and provide critical constraints on style of bubble nucleation that can drastically change the calculated decompression rate (Fig. 3.5).

3.5.4 Implications for disequilibrium degassing mechanisms

One of the fundamental questions leftover from Chapter 2 is how the water concentration changes in the melt during disequilibrium degassing. These experiments have very likely

experienced disequilibrium degassing, so the inter-bubble profiles can be leveraged, along with the disequilibrium degassing code developed in Chapter 2, to investigate the disequilibrium degassing pathway in these experiments. For this test, rather than solving for the best-fit

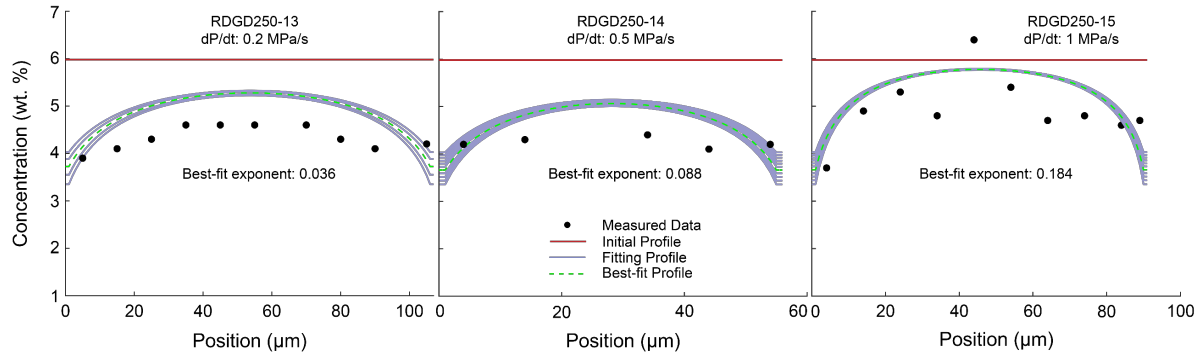

Figure 3.7. Inter-bubble profile fitting results when accounting for disequilibrium conditions. The best-fit exponent to Eq. 2.4 increases with increasing decompression rate. Fitting profiles shown are ±0.005 from the best-fit value.

decompression rate, instead the profile was fit to find the best-fit "catch-up exponent" in Eq. 2.4. The forced fit of the equilibrium water value at the two edges of each profile was removed for this test, and nucleation pressure was assumed to be the same as calculated previously (P_N = 67 MPa).

The best-fit catch-up exponent increases as decompression rate increases, for the three decompression rates tested (Fig. 3.7). This contrasts with how the catch-up exponent was treated in the Chapter 2 modeling, where the exponent was assumed to be constant across all decompression rates. Additionally, the values of the exponent (0.036 – 0.184) are all greater than the exponent values tested, even the variable exponent results presented in Appendix A (Fig. A-S3). Assuming that water re-equilibration does follow an exponential decay pattern, these results imply that the kinetics of water exsolution during disequilibrium degassing is sensitive to decompression rate, with faster exsolution at faster decompression rate. This presents an interesting future avenue of additional exploration. More experiments with different quench pressures would be useful to also investigate whether the catch-up exponent changes with

pressure, even at the same decompression rate. Potentially, experiments of this nature could be used to construct a whole disequilibrium degassing relationship for this composition, as a function of decompression rate and pressure. This is a relationship that is currently lacking in the literature, with just one example at the time of writing this dissertation (Gonnermann and Manga, 2005).

3.5.5 Additional experimental needs

These experiments represent the first attempt to utilize coordinated decompression rate meters with the same experimental charge. In general, both decompression rate meters are able to retrieve similar decompression rates that are within one order of magnitude of the known imposed decompression rate, given several assumptions associated with bubble nucleation mechanism. The next steps are to conduct similar decompression experiments but with variable decompression rates. Logically, the next step to advance our understanding would be non-linear decompression, with an initial slow decompression that becomes faster to match the typical variation inferred for eruptions (e.g., Gonnermann and Manga, 2007; Su and Huber, 2017). This requires some refinement of the experimental technique presented in this study, though. For instance, a method to overcome the extreme growth of the hydration bubbles at quench pressures <50 MPa is needed, as variable decompression rate would need to go to lower pressures to produce meaningful differences in decompression timescale. Additionally, lower quench pressures would assess the impact of a late-stage bubble nucleation event better (e.g., Mangan and Sisson, 2000) on recorded BNDs.

3.6 Conclusions

Magma decompression rate is a non-linear parameter over the duration of ascent to the surface, and refined representation of eruption dynamics requires a more nuanced examination of

the range of decompression rates in a given eruption. Currently popular decompression rate meters are potentially well-suited to this task, as BND typically records the fastest part of the decompression, and diffusion modeling of magmatic volatiles typically records the slowest part of the decompression (e.g., Shea, 2017; Myers et al., 2021). This study used decompression experiments that were designed to utilize both decompression rate meters within the same experimental charge in order to provide the first comparison of these two meters, with known imposed decompression rates, given that the decompression rate is the same for both. My results indicate that both meters can retrieve similar and useful decompression rates, though BND results are highly sensitive to assumed nucleation style and heterogeneities within the starting material. Further work is needed to constrain better nucleation mechanisms in order to increase the resolution of the decompression rate actually retrieved by BND, as it is currently only consistently resolved within an order of magnitude. Diffusion modeling results are also sensitive to timing of bubble formation, particularly when bubble formation is late in the decompression, as is the case for homogeneous nucleation. Further testing of this approach should utilize non-linear decompression rates to test whether BND truly records the faster decompression while diffusion modeling records the slower decompression rate.

Chapter 4. Evaluating Lava Flow Propagation Models with a Case Study from the 2018 Eruption of Kīlauea, HI

In review as: deGraffenried, R., Hammer, J., Dietterich, H., Perroy, R., Patrick, M., & Shea, T. Evaluating lava flow propagation models with a case study from the 2018 eruption of Kīlauea, HI. *Submitted to: Bulletin of Volcanology.*

4.1 Abstract

The 2018 lower East Rift Zone (LERZ) eruption of Kīlauea, Hawai‘i provides an excellent natural laboratory to test models of lava flow propagation. During early stages of eruption crises, the most useful lava flow propagation equations utilize easily determined parameters and require few *a priori* assumptions about future behavior of the flow. Here, we leverage numerous observations of lava flows collected over the duration of the eruption crisis at Kīlauea in 2018 to test simple lava flow propagation models. These models track the 1D propagation of the flows according to three main rheological stopping forces: bulk viscosity, yield strength, and growth of a surface crust. We calculate the predicted changes in length through time of three 2018 flows that vary in bulk composition, crystal content, and total flow length. Cooler flows that were crystal-rich tended to be limited by crust strength, though early propagation could be controlled by bulk viscosity. We find that variations in effusion rate significantly impact flows that were short-lived; flows that were produced during steady-state effusion were readily approximated by average values for the entire flow. Thus, accurate knowledge of variations in effusion rate are critical to accurate lava flow propagation forecasting.

4.2 Introduction

Lava flows are a major hazard during basaltic eruptions. Although the risk of loss of human life to lava inundation is typically low, particularly for well-monitored volcanoes, lava flows can cause major damage to buildings and infrastructure. This is exemplified by the 2018

eruption of Kīlauea on its lower East Rift Zone (LERZ), during which 716 structures were damaged, and millions of dollars were spent to rebuild highways buried by lava (Neal et al., 2019; Houghton et al., 2021b). Therefore, it is important to understand how lava flows propagate, in terms of path, velocity, and length. The path is perhaps the easiest parameter to forecast, given topographic data of suitable resolution and accuracy as lava flows behave as gravity currents and follow the route of steepest descent (Favalli et al., 2005). However, the ability to predict flow front velocity and final length with useful accuracy for a broad range of conditions remains difficult (Harris et al., 2016; Dietterich et al., 2017).

Lava flows are complex systems that are influenced/controlled by many factors, both internal (e.g., viscosity) and external (e.g., substrate slope). Studies of actively flowing lava provide holistic views of emplacement processes, and field data comprise the gold standard for evaluating the efficacy of simple physical characerizations of flow dynamics. However, variables controlling lava flow advance tend to be correlated, making it difficult to isolate their effects. Understanding the influence and relative importance of individual variables is critical for hazard forecasting (e.g., Walker et al., 1973; Rowland and Walker, 1990; Griffiths, 2000). Thus, one branch of research has utilized analytical viscous flow theory (e.g., Huppert 1982a; 1982b; Lister, 1992; Takagi and Huppert, 2010) and lava analogs flowing in controlled experimental environments. For example, studies have successfully applied viscous flow equations to describe the balance of forces controlling flow front velocity and ultimately, flow length of polyethylene glycol (PEG) wax and PEG wax-solid particle slurries emplaced in both subaerial and submarine settings (e.g., Fink and Griffiths, 1992; Cashman et al., 2006; Kerr et al., 2006; Lyman and Kerr, 2006). These quantitative descriptions of flow dynamics are suitably tuned to describe the propagation of PEG and PEG-solid particle slurry flows. However, their utility in forecasting the

advance rate and lengths of lava flows has not been thoroughly evaluated. One of the initial goals of this project was to evaluate whether wax is a suitable analog material for lava. However, we found this question difficult to evaluate directly as deviations in behavior could be attributed to either fundamental differences in the materials themselves or natural complexities that influence lava flows but not wax flows. For example, wax studies do not use variable effusion rate, but effusion rate can vary significantly during an eruption (e.g., Harris et al., 2016; Bonny and Wright, 2017). Instead, in this study, we evaluate sloping viscous theory as a method to calculate lava flow length evolution with time, considering that it adequately described wax flow propagation.

Two sets of equations that describe 1D flow propagation, or how flow length evolves through time, were developed by Lyman and Kerr (2006), "LK", and Castruccio et al. (2013), "CEA", using the same physical description of lava. The equation sets differ regarding the time-dependency of input parameters and the treatment of the mass flux source. The diverse and high-frequency observations of the early LERZ events permit quantitative comparison of these viscous flow models. We take a hierarchal approach to testing whether *a priori* knowledge of input parameter time-dependency is needed to recover the observed time-length data, and secondly, to determine the level of specificity that is needed to characterize each parameter in the equation sets. Our objectives are to (1) discover the extent to which these simple equations can be used to describe accurately lava flow propagation and (2) infer the rheologic parameters that dominated the propagation of select lava flows during the LERZ eruption.

We start by quantifying key aspects of three lava flows from the early part of the LERZ eruption and use these measurements to test the equation sets' ability to match the observed flow length as a function of time ("time-length data"). We chose the likely volume-limited (Guest et

al., 1987) flows emanating from early fissure 8, fissure 17, and the fissure 20/22 complex because they span the full range in rheology exhibited in the 2018 sequence (Neal et al., 2019; Soldati et al., 2021), and they also most closely resemble the wax experiments. We approach the fundamental efficacy question by presuming the validity of the equation sets and back-solving for the variable effusion rate relationships that most closely conform to the time-length data. We then consider the plausibility of the resulting flux curves in the context of other observations and a theoretical understanding of effusive eruption dynamics.

4.2.1 2018 Kīlauea LERZ eruption summary

Drawing from the eruption chronology detailed in Neal et al. (2019), the 2018 eruption commenced on May 3rd, after a period of precursory activity that involved overflow at two lava lakes, the collapse of the Puʻu ʻŌʻō cone, propagation of earthquakes downrift, and opening of ground cracks in the vicinity of the impending eruption. This activity was caused by pressurization of the magmatic plumbing system and subsequent failure of a blockage beneath Puʻu ʻŌʻō that allowed magma to travel farther downrift (Patrick et al., 2020; Roman et al., 2021). During the first two weeks of the eruption, the lava that erupted was relatively viscous and formed pads that rarely traveled more than tens of meters from the source vents. The high viscosity, cooler temperatures, and evolved bulk composition, relative to lava that had been erupting from Puʻu ʻŌʻō, suggested that the lava that erupted during the first two weeks was sourced from leftover stored magma from previous LERZ eruptions (Gansecki et al., 2019). This phase included the first observed discharge of andesite from Kīlauea. Fissure eruption durations during this early phase were generally short.

On May 18th, a shift in the temperature and composition of the magma supplied to the vents changed the behavior of the lava flows and the longevity of individual fissures. Fresher,

hotter magma began to erupt at higher effusion rates (Gansecki et al., 2019; Dietterich et al., 2021), which produced fast-moving lava flows that rapidly reached the coast. This phase of the eruption was generally dominated by fissure reactivation, though a few new fissures opened. One of the early vents, fissure 8 (and the cone subsequently named Ahu‘ailā‘au), reactivated on May 27th and was the main center of eruptive activity by May 28th. This long-lived fissure fed a large, channelized flow that ultimately reached the ocean (Patrick et al., 2019). Most eruptive activity ceased on August 4th. Although not directly addressed in this paper, the LERZ eruption was accompanied by summit collapse events that also ceased when lava effusion ceased (Anderson et al., 2019).

4.2.2 Lava flow models

In this study, we examine two sets of equations that describe the same analytical theory of three rheologic regimes as stopping forces for lava flows. These two equation sets differ in two ways: (1) ability to vary input parameters through time and (2) method of calculating lava mass flux. The three rheologic regimes we examine are limited by: viscosity, yield strength, and crust development.

The first equation set, utilized by Lyman and Kerr (2006; “LK”), assumes a constant value for all input parameters. The three equations that govern length (L) in m vs time (t) in s for viscosity limited, lava yield strength limited, and crust strength limited flows are given by, respectively:

$$L_{visc} = C_1 \left[\frac{g\Delta\rho sin\beta q^2 t}{\eta}\right]^{\frac{1}{3}} \quad (4.1)$$

$$L_{ys} = C_2 \frac{qg\Delta\rho sin\beta}{\sigma_0} \quad (4.2)$$

$$L_{crust} = C_3 \left(\frac{q^2 \rho g \sin \beta}{\sigma_c \sqrt{\kappa t}} \right)^{1/2} \quad (4.3)$$

where g is acceleration due to gravity in m s^{-2}, $\Delta\rho$ is the density difference between the lava and air in kg m^{-3}, β is ground slope, q is volumetric flow rate normalized to flow width in m^3 m^{-1} s^{-1}, η is bulk viscosity in Pa s, σ_0 is bulk yield strength in Pa, σ_c is crust yield strength in Pa, κ is thermal diffusivity in m^2 s^{-1}, and C_1, C_2, and C_3 are constants. A summary of all symbols and their units can be found in Table 4.1. Kerr and Lyman (2007) utilized Equations 4.1 and 4.3 to infer material properties of the 1988-1989 Lonquimay, Chile andesite lava flow, and concluded that flow propagation was predominantly controlled by the crust.

Table 4.1. Summary of variables

Symbol	Meaning	Units
L	length	m
W	width	m
g	gravitational acceleration	m s^{-2}
ρ	lava density	kg m^{-3}
β	ground slope	degrees
q	normalized volume discharge rate	m^3 s^{-1} m^{-1}
t	time	s
η	viscosity	Pa s
σ_0	yield strength	Pa
σ_c	crust yield strength	Pa
κ	thermal diffusivity	m^2 s^{-1}
V	volume discharge rate	m^3 s^{-1}
B	empirical constant	Pa
C	empirical constant	K^{-1}
T_0	liquidus temperature	K
T_e	eruption temperature	K
φ	crystal fraction	n/a

In contrast, the second equation set, utilized by Castruccio et al. (2013; "CEA") to describe several historic lava flows, is parameterized to allow input parameters to vary at each

calculation interval. These equations use the same governing physical laws as the LK calculations. However, Castruccio et al. (2013) used the equations to derive lava material properties, given knowledge of the other parameters, rather than solving for flow length given the knowledge of material properties. The length of the flow is computed as a summation of the contribution of each calculation interval. The equations that govern the three rheologic regimes are:

$$L_{visc} = C_1 \sum_{i=1}^{n} \left(\frac{V_i^2 \rho g \sin \beta_i \, t_i}{\eta W_i^2} \right)^{1/3} \tag{4.4}$$

$$L_{ys} = C_2 \sum_{i=1}^{n} \left(\frac{V_i \rho g \sin \beta_i}{\sigma_{0i} W_i} \right) \tag{4.5}$$

$$L_{crust} = C_3 \sum_{i=1}^{n} \left(\frac{V_i^2 \rho g \sin \beta_i}{W_i^2 \sigma_{ci} \sqrt{\kappa t}} \right)^{1/2} \tag{4.6}$$

Here, instead of a single q term, there are instead V (effusion rate in $m^3 s^{-1}$) and W (flow width in m).

Thus, the LK and CEA equation sets incorporate a similar physical description of fluid flow but differ in the treatment of volume flux. This is a consequence of differing lava source geometries. The LK equation set was derived to describe flowing wax released all at once into a tank from a single slot-shaped opening. Thus, the mass flux term used in these equations normalizes the full volume by the width of the tank; neither flux nor supply structure can vary in time. In contrast, the CEA equation set treats the volume supply as incremental, potentially varying in time, and allows changes in flux to be accompanied by changes in flow width. Our adaptation of these variables for application to LERZ flows is discussed in the Methods section.

4.2.3 Lava Flows Selected for Study

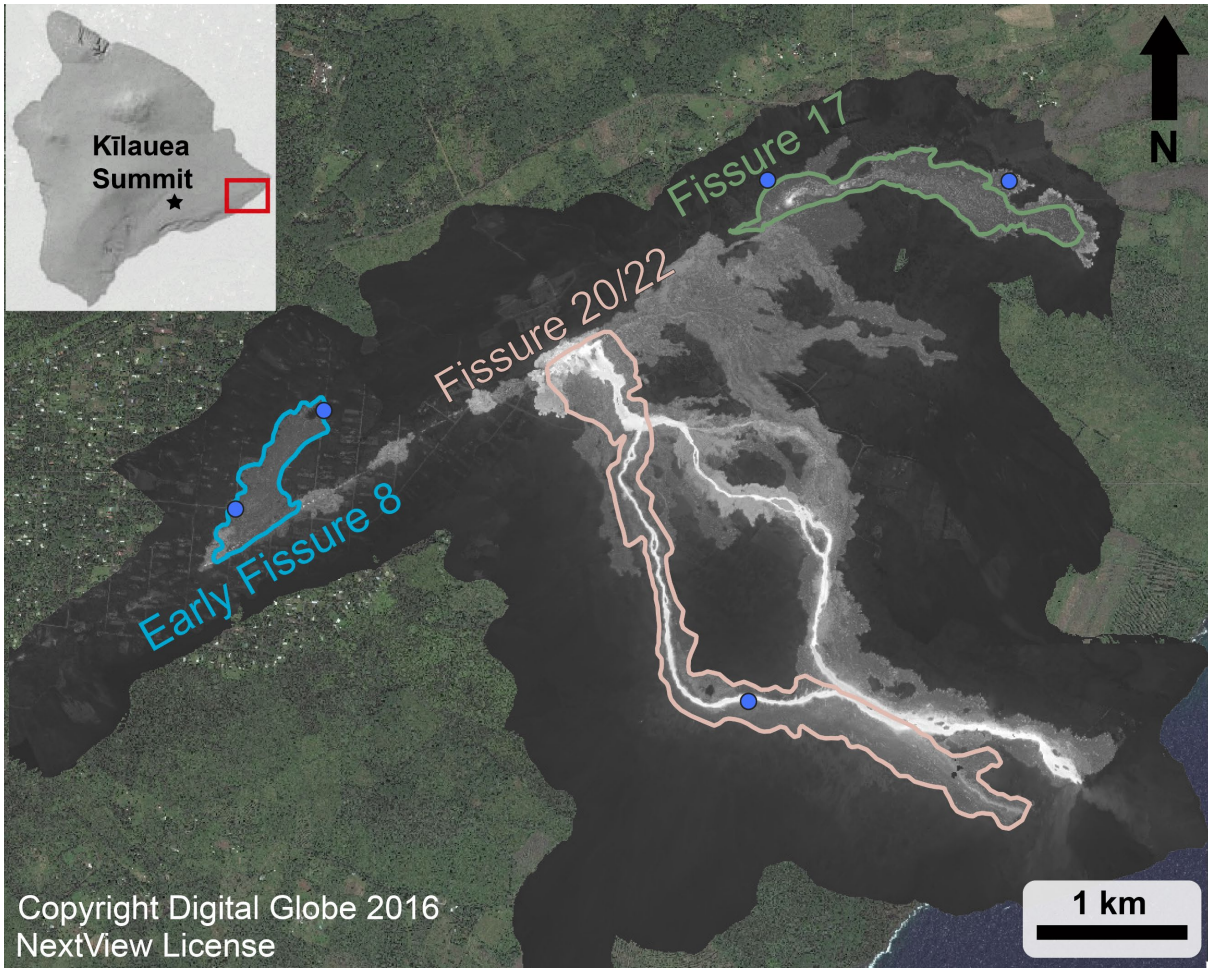

Figure 4.1. Map of the three studied flows and associated samples used for textural analysis. The black and white area is the extent of the thermal map (see "Data Sources"). Temperature in the thermal image is displayed as gray-scale values, with the brightest pixels indicating the hottest areas. The base is a copyrighted color satellite image (used with permission) provided by DigitalGlobe. Flow outlines represent the final extent considered for each flow, and blue dots are the collection locations of each sample. Our use of the shorter length for F17 is described in the "Key flow attributes" section. The base thermal image is of the lava flow field as of May 21, 2018. The outline for EF8 is from May 7, the outline for F17 is from May 15, and the outline for F20/22 is May 21. Red box on the inset map of the Island of Hawai'i shows the extent of the map.

We selected three lava flows that span a range of composition, particle content, and distance traveled (Fig. 4.1). Here, we use the term "particle" to indicate both bubbles and crystals. The early fissure 8 (EF8) flow, from the first sluggish phase of the eruption (phase 1; ~4-5 wt. % MgO), is a crystal-rich lava with a relatively evolved liquid (Gansecki et al., 2019). We note that we use the qualifying term "early" on this flow to differentiate it from the

voluminous flow produced when the fissure reactivated (phase 3; >6 wt. % MgO). The fissure 17 (F17) flow is the most viscous due to its evolved composition (<4 wt. % MgO) and crystallinity (Gansecki et al., 2019). The final flow is from the flow field produced by fissures 20 and 22 (F20/22) during a transitional period of increasing effusion rate and magma temperature (phase 2; 4.5-6 wt. % MgO). We treat these fissures as one system because there was significant overlap between the flows produced by these fissures, and it is difficult to determine the contributions of each fissure to the flow. This flow field, sourced from fresh magma supplied ~2 weeks after the eruption started, is crystal-poor and lowest in viscosity of the three flows (Gansecki et al., 2019). Note that we conclude our calculations of F20/22 propagation once it reaches the ocean, rather than when propagation ceases.

4.3 Methods

4.3.1 Data sources

Imagery of the flows comes from three sources: (1) still-shots captured from a helicopter (2) composite ortho-rectified images, 'orthomosaics', assembled from drone overflight imagery and (3) thermal orthomosaics from helicopter overflight imagery. The drone imagery was captured and processed following Turner et al. (2017). The thermal imagery was captured and processed following Patrick et al. (2017). Although the thermal imagery contains information on temperature variations within the flow, this information was only used qualitatively to identify flow features. Absolute temperature of each flow was obtained petrologically, discussed below.

Samples were collected both syn- and post-eruption (Fig. 4.1). All samples for EF8 were collected during emplacement, and additional samples are not available; the flow was buried entirely by the reactivated fissure 8 flow. Only a medial sample was used for F20/22 as the proximal and distal samples were unsuitable to characterize the lava flow. The proximal samples

available were scoriaceous, and thus only representative of fragmented material, particularly with respect to the relative proportion of vesicles. Distal samples were overprinted by lava-water interactions at the ocean entry, and samples could have come from any of the three adjacent flows that entered the ocean at close proximity. Syn-eruptive quenched samples were collected by the USGS. Post-eruptive samples were collected during a helicopter field campaign, and the collected samples were chosen to be the glassiest available. Glassier samples are more representative of the crystallinity of the flow during emplacement and are less influenced by groundmass crystallization once the flow halts and cools.

4.3.2 Macro-scale feature characterization

The still-shots were collected at oblique angles to the ground surface, so the images were corrected for look angle by georeferencing using QGIS (version 3.4.5). Reported error in flow front location is the maximum error in the final georeferenced image location (Appendix B).

A primary vent location for measurements of flow length was selected for each flow on the basis of constant effusion and centralized location to flow propagation (Fig. 4.2). All subsequent measurements of flow length were conducted relative to that point, following the flow route as discerned by flow features, such as channels, rather than straight-line distances to the flow front. Flow width measurements were made as close to the active flow front as possible, but where the width is not changing rapidly. The ground slope between images was also calculated along the flow path, using the USGS National Elevation Dataset 1983 10 m DEM.

Total flow volumes were also calculated from aerial imagery. Surface area of the flow was measured in QGIS then multiplied by average flow thickness (Tables 4.3-4.5). Average flow thickness was determined from field measurements and a digital surface model of the F17 flow constructed from drone imagery (Fig. A-S2). Volume was corrected for vesicularity by

approximating 25 vol. % vesicularity across all three flows, as an intermediate value between all flows (Table 4.2), such that all volumes are dense rock equivalent (DRE) volumes. Mean output

Table 4.2. Microfeatures of the three flows

Flow	EF8[c]	F17[d]	F20/22[e]
SiO_2	51.57	56.94	52.08
TiO_2	4.26	3.18	3.94
Al_2O_3	12.77	12.25	12.73
FeO*	13.46	12.26	13.55
MnO	0.19	0.2	0.2
MgO	4.56	2.79	4.81
CaO	8.71	6.74	9.04
Na_2O	2.98	3.33	2.79
K_2O	0.97	1.61	0.8
P_2O_5	0.56	0.81	0.41
SO_3	0.03	0.05	0.05
Cl	0.01	0.04	0.01
Total	100.08	100.22	100.41
Temperature (°C)[a]	1117	1071	1121
Melt Viscosity (Pa s)[b]	791	8031	657
Melt Density (kg/m^3)[f]	2726	2657	2724
Initial Crystal Content (vol. %)	26.5	24.1	8.3
Initial Vesicle Content (vol. %)	2.8	11.0	53.0
Initial Crystal Aspect Ratio	2.6	2.1	2.9
Final Crystal Content (vol. %)	80.1	45.6	8.3
Final Vesicle Content (vol. %)	3.8	1.1	53.0
Final Crystal Aspect Ratio	1.9	2.1	2.9

[a]Temperature calculated using Beattie (1993)

[b]Viscosity calculated using Giordano et al. (2008), assuming 0.2 wt. % water

[c]Samples used are: KE62-3231 for composition and temperature, KE62-3228-1A for initial crystal content, and kil2018_F8s4 for final crystal content

[d]Samples used are: KE62-3261 for composition and temperature, KE62-3252 for initial crystal content, and KE62-3345 for final crystal content

[e]Samples used are: KE62-3244 for composition and temperature, KE62-3340 for initial crystal content, and KE62-3334 for final crystal content

rate (Harris et al., 2007) was calculated by dividing the DRE volume by the time at which the measured length vs time curve flattened, indicating no additional flow propagation (Fig. 4.3). Without more robust estimates of effusion rate variations in time for the flows of interest, we choose to use this estimation of average effusion rate for our modeling as it requires the fewest assumptions.

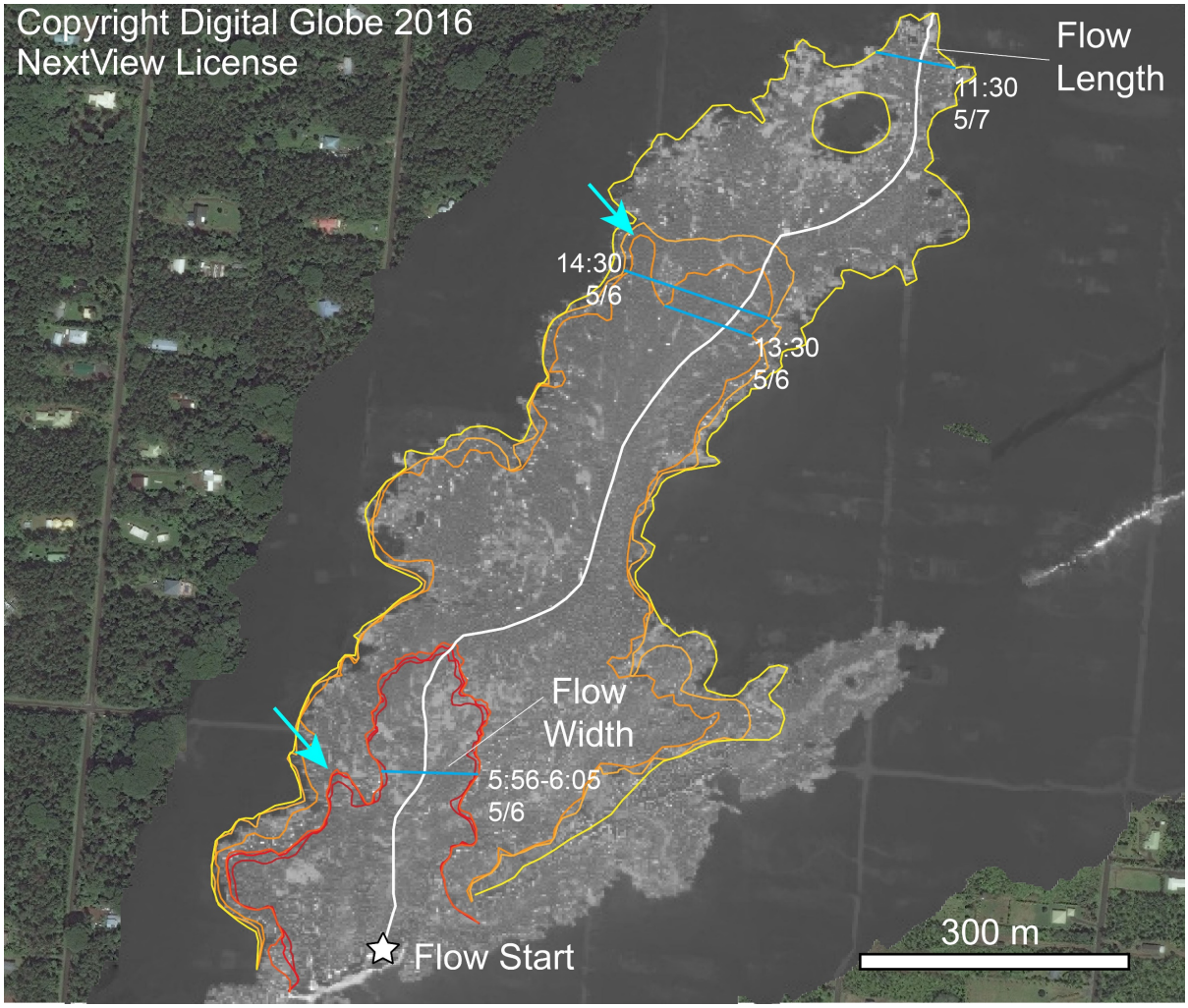

Figure 4.2. Example of flow outline and its evolution during the early fissure 8 flow. Colored outlines indicate the shape of the flow at a given time (HST), and the blue lines indicate the flow width at the time next to the line. The line labeled "Flow Length" shows the measured path of flow length over the duration of the flow, following the observed flow paths in the studied imagery. Light blue arrows point to rapidly advancing lobes that are explained in the Discussion section. The base thermal image is from May 7.

4.3.3 Micro-scale feature characterization

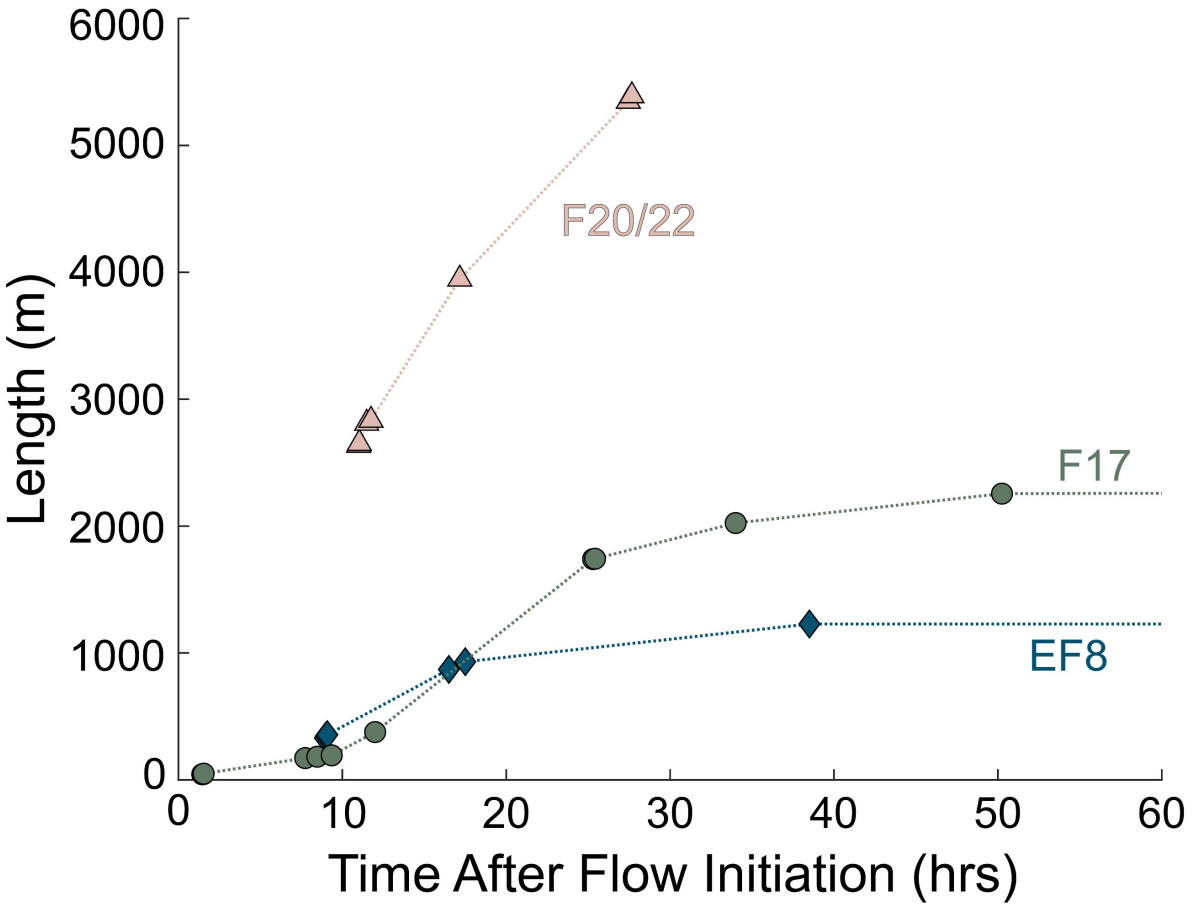

Figure 4.3. Plot of flow length versus time data for each flow. Error bars for flow front location are smaller than the symbols (Appendix B). The lines extend from the final point for EF8 and F17 to indicate that the flow may have continued expanding slightly for a time, but the main propagation was finished at the time of the last plotted point. In contrast, the F20/22 line is truncated at the last point to indicate the ocean entry and cessation of flow propagation over land. Although not explicitly plotted here, all flow lines could be extended to intersect zero length at the start of the flow propagation.

Back-scattered electron (BSE) images were collected from thin sections of each sample using the JEOL Hyperprobe JXA-8500F electron microprobe located at the University of Hawai‘i at Mānoa (Fig. 4.4). Image collection at variable magnifications followed the methodology in Shea et al. (2010). Glasses were analyzed by wavelength-dispersive spectroscopy on the same instrument, with an accelerating voltage of 15 keV, a current of 10 nA, and spot size of 10 μm. Time-dependent intensity corrections were applied for Na when

necessary. Two basaltic glass standards, VG2 and A99, were measured as unknowns during analysis to check for accuracy and evaluate drift.

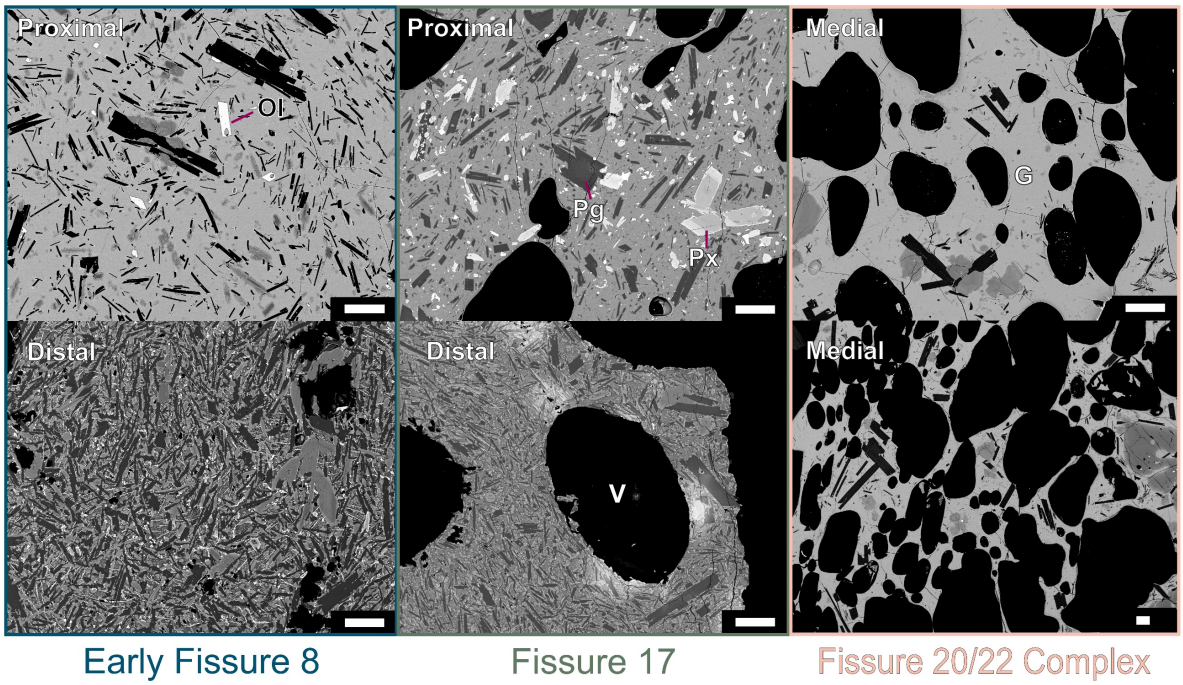

Figure 4.4. Representative back-scattered electron images from the five samples used to measure flow microtexture. The scale bar in all of the images is 100 μm. Distances (proximal, medial, and distal) refer to relative distances from the vent. Although the absolute grayscale values are different between the images, the relative grayscale of the different phases is the same. Ol = olivine, Pg = plagioclase, Px = pyroxene (orthopyroxene and clinopyroxene were not differentiated), V = vesicle, and G = glass.

BSE images were subsequently processed in Adobe Photoshop and imported to NIH ImageJ to measure the area and aspect ratio of particles. Only particles >5 pixels in area were included in measurements. These measurements were conducted separately; the area measurement included all particles in the image, whereas the aspect ratio measurement excluded crystals touching the edge of the image (Hammer et al., 1999; Muir et al., 2012). Vesicles were all approximated as spheres, so their aspect ratios were not measured.

4.3.4 Modeling

Our modeling used a two-pronged approach, with each prong corresponding to the equations from either the LK or CEA equation set (Figure 5). As a subset within each prong,

particles were treated with differing levels of complexity, with respect to assumed shape (e.g., spherical vs. parallelepiped) and particle types (e.g., crystals and/or vesicles) incorporated into

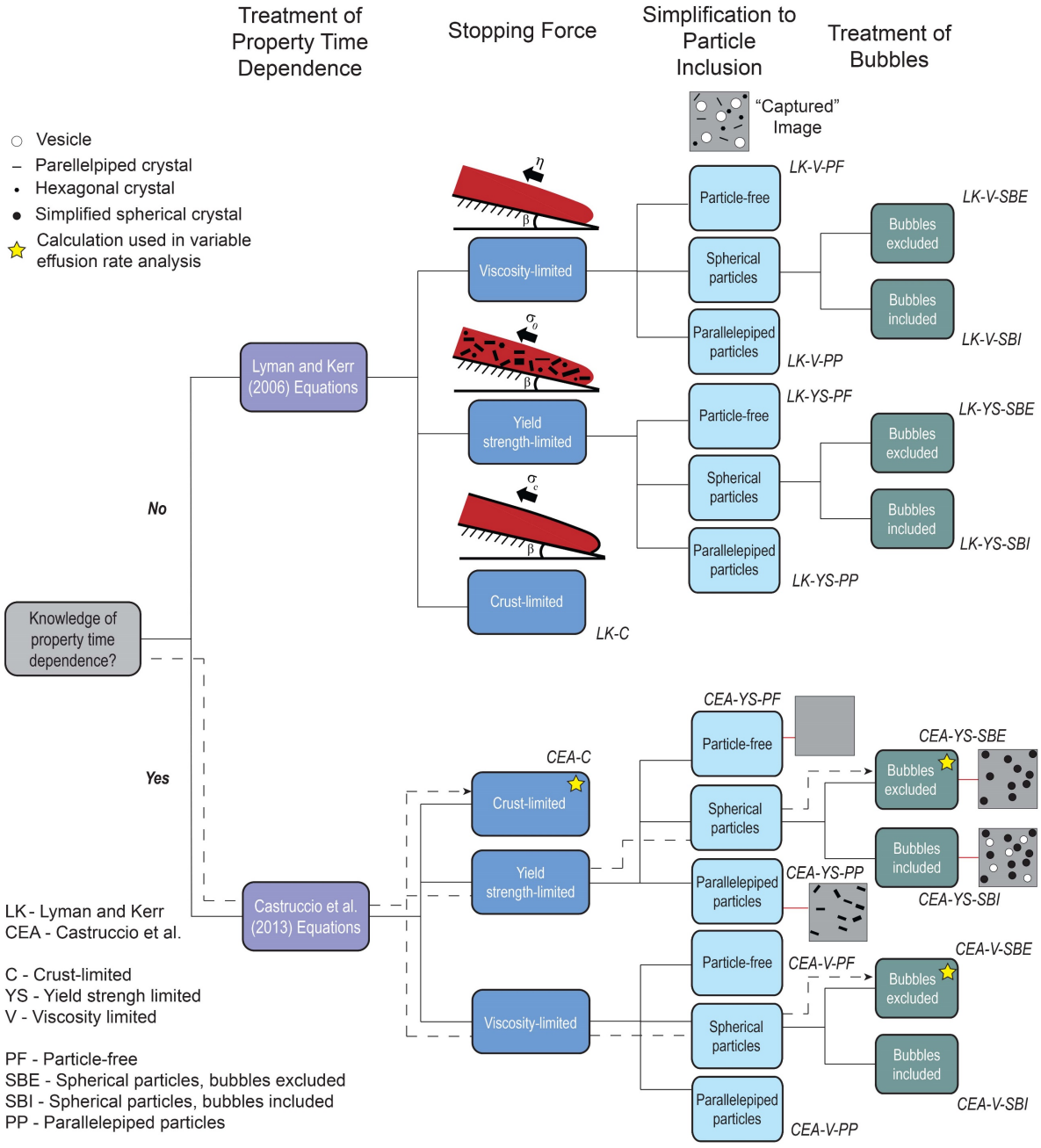

Figure 4.5. Flow chart illustrating the calculation approach in this study. Schematic flows in the "Stopping Force" column represent the forces stopping the flows (after Castruccio et al., 2013). The schematic BSE images in the "Simplification to Particle Inclusion" column shows the treatment of particles for each calculation type, and it is the same between both the LK and CEA calculations. Abbreviations next to each terminus indicate the scenario, and are used later in the text. Dashed line and stars indicate the paths used for calculations associated with variable effusion rate in the Discussion section.

the calculations (Figure 5). We use the term "scenario" to refer to a specific calculation branch, whereas "model" refers to the process of calculating the length vs. time curves. Measurements from the BSE images informed our characterization of particle abundance and crystal shape.

Glass composition was used to calculate initial liquid viscosity (Giordano et al., 2008), liquid density (Iacovino and Till, 2019), and eruption temperature (Beattie, 1993) (Table 4.2). Water content for viscosity and density was assumed to be 0.2 wt. %, though this is likely a slight overestimation based on typical Hawaiian basalt lava flow water contents of ~0.1 wt. % (Seaman et al., 2004). However, volatile contents from erupted products at Kīlauea have been as high as 0.3 wt. % (Ferguson et al., 2016); thus, our melt viscosity values are likely an underestimation, but the difference in melt viscosity between 0.1 and 0.2 wt. % water is less than a factor of two. We treat the flows as isothermal and do not consider any changes to the dissolved volatile content during propagation, so any changes to the material properties of the lava are a function of particle content. Relative viscosity incorporating solid particles was calculated using the model of Costa et al. (2009), using fit parameters from Cimarelli et al. (2011) that most closely matched the measured crystal aspect ratios as well as the spherical particles. Calculated capillary numbers for our samples are <0.1, so we incorporate bubbles into our calculations, where appropriate, as solid spherical particles (Mader et al., 2013; Appendix B).

Effusion rate for the CEA equations was maintained as a volume per unit time parameter. However, mass flux was treated differently for the LK equations. Instead of separate volume and width terms, the LK equations use the volumetric flow rate normalized to a constant width (i.e., the flume width in the experiments; "q" of Lyman and Kerr, 2006). The analogous physical parameter in the natural setting is the length of the fissure. Thus, q is calculated as the V term in the CEA equations divided by the fissure's length, as measured in aerial photos.

Treatment of F17 introduces additional complexities. The fissure increased in length for several hours after the initial opening and was heterogeneous in terms of eruption style; fountaining occurred at one end and Strombolian explosions at the other. In principle, it is possible to discretize the fissure into small segments and then estimate the contributions to the flow from each segment. However, determining productive/unproductive segments of the fissure is unnecessarily complex, yielding little difference in calculated final length. Specifically, it increases the number of sources of uncertainty and would be impractical to execute during a crisis. We adopt the fissure's full length as the reference length, noting that this assumption decreases q, which produces a shorter calculated final flow length. Final length in the context of our modeling refers to the predicted flow length at the time we consider as the "end" of a given flow.

Yield strength of natural silicate melts remains poorly constrained, with measurements ranging from 10^1 Pa (Robert et al., 2014) to 10^4 Pa (Fink and Zimbelman, 1990) for basalts; we follow the approximation that incorporates both temperature and crystallinity employed by an existing lava flow propagation model, FLOWGO (Harris and Rowland, 2012). The yield strength of the basaltic liquid is approximated as a function of eruption temperature relative to the liquidus, and crystals can be incorporated by adding a term that accounts for their effect of increasing yield strength with increasing abundance (Dragoni, 1989; Pinkerton and Stevenson, 1992):

$$\sigma_0 = B\left[e^{C(T_0 - T_e)} - 1\right] + [6500\varphi^{2.85}] \quad (4.7)$$

Here, B and C are empirical constants of 0.01 and 0.08, respectively, T_0 is liquidus temperature, T_e is eruption temperature, and φ is crystal fraction. This equation assumes all crystals are 1 mm long on their longest axis and have tabular shapes with axis length ratios of 10:5:1. This

approximation likely overestimates the impact of crystals on yield strength for our samples as most crystals were <1 mm. However, a more accurate 3D determination of crystal size distribution and aspect ratio would be a time-consuming exercise in the context of an emergency response effort. In our case, the overestimation of yield strength by approximating the crystals as 1 mm could be by as much as an order of magnitude (Pinkerton and Stevenson, 1992), but as seen in our modeling results, even the maximum possible value of yield strength does not impact flow propagation in most cases.

The effective strength of the crust can be estimated, to an order of magnitude, from the flow width using the empirical equation of Kerr et al. (2006):

$$\sigma_c \sim \frac{1}{W}\left[\frac{(g\Delta\rho)^5(\cos\beta)^5 V^7 \eta^3}{\kappa^4}\right]^{1/8} \tag{4.8}$$

The mass flux (V) used for this calculation is the mean output rate for each flow.

4.4 Results

4.4.1 Key flow attributes

The initial opening of EF8 occurred on May 5, and lava began erupting from the fissure at ~21:00 HST (Houghton et al., 2021a). The flow ceased moving by 11:30 HST on May 7 after achieving a final length of 1230 m (Table 4.3).

F17 began erupting on May 13 at 4:30 HST (HVO Staff, 2018). Although the fissure kept erupting for over a week, we consider the flow to have finished its initial advance by 6:45 HST on May 15. After this time, the fissure was weakly fountaining, and any additional lengthening of the flow occurred as localized "ooze-outs" around the edge of the flow. On May 18, when fresh magma reached the LERZ system (Gansecki et al., 2019), there was a noticeable increase in fountain height and thus volumetric output of lava, and lava extruded from the edges of the

Table 4.3. Physical measurements for early fissure 8 flow

Fissure Start Time: 5/5, 21:00 HST; Flow Start Coordinate 299665E, 2153040.1N

Image Type	Date	Time (HST)	Time After Fissure Start (s)	Flow Length (m)	Flow Width (m)	Flow Front Velocity (m s^{-1})	Ground Slope (degrees)	Crust Yield Strength (x10^5 Pa)
Still Shot	6-May	5:56	32160	330	114	0.010	0.9	2.8
Still Shot	6-May	6:00	32400	346	115	0.068	2.4	2.8
Still Shot	6-May	6:05	32700	356	116	0.032	2.8	2.8
Drone Image	6-May	13:30	59400	870	112	0.019	0.8	2.9
Thermal Image	6-May	14:30	63000	931	185	0.017	1.1	1.7
Thermal Image	7-May	11:30	138600	1228	107	0.004	1.9	3.0
Thermal Image	9-May	17:30	333000	1228	107	0.000	0.0	3.0

Other physical parameters

Fissure Length (m)	Flow Thickness (m)	Flow Area (m^2)	DRE Flow Volume (x10^5 m^3)	q (m^3 m^{-1} s^{-1})	Q (m^3 s^{-1})
117	2 ±2	343375	5.15 - 10.30	0.0318	3.7162

Table 4.4. Physical measurements for fissure 17 flow

Fissure Start Time: 5/13, 04:30 HST; Flow Start Coordinate: 303363.8E, 2155371N

Image Type	Date	Time (HST)	Time After Fissure Start (s)	Flow Length (m)	Flow Width (m)	Flow Front Velocity (m s^{-1})	Ground Slope (degrees)	Crust Yield Strength (x10^5 Pa)
Still Shot	13-May	5:57	5220	44.2	57.1	0.008	2.9	39.7
Still Shot	13-May	5:59	5340	44.7	58.5	0.004	3.1	38.8
Still Shot	13-May	6:01	5460	44.9	58.7	0.002	2.1	38.7
Still Shot	13-May	6:02	5520	48.7	62	0.063	2.1	36.6
Drone Orthomosaic	13-May	12:14	27840	171.5	306.4	0.006	2.1	7.4
Drone Orthomosaic	13-May	12:58	30480	182.2	363.3	0.004	2.1	6.3
Drone Orthomosaic	13-May	13:51	33660	193.0	360.6	0.003	2.1	6.3
Thermal Orthomosaic	13-May	16:30	43200	376.6	135.3	0.019	0.6	16.8
Still Shot	14-May	5:48	91080	1740	151.4	0.028	2.4	15.0
Still Shot	14-May	5:55	91500	1742	154.5	0.006	2.4	14.7
Thermal Orthomosaic	14-May	14:30	122400	2024	121.1	0.021	2.2	18.7
Thermal Orthomosaic	15-May	6:45	180900	2256	237.6	0.004	1.3	9.6
Thermal Orthomosaic	22-May	6:45	785700	2337	n.m.[a]	n.m.	n.m.	n.m.

Other physical parameters

Fissure Length (m)	Flow Thickness (m)	Flow Area (m^2)	DRE Flow Volume (x10^6 m^3)	q (m^3 m^{-1} s^{-1})	Q (m^3 s^{-1})
491	6 ±4	528144	2.38 - 3.96	0.0267	13.1379

[a]n.m. - not measured

Table 4.5. Physical measurements for fissure 20/22 complex flow

Fissure Start Time: 5/19, 00:00; Flow Start Coordinate: 302088.46E, 2154419.36N

Image Type	Date	Time (HST)	Time After Fissure Start (s)	Flow Length (m)	Flow Width (m)	Flow Front Velocity (m s^{-1})	Ground Slope (degrees)	Crust Yield Strength (x10^5 Pa)
Still Shot	19-May	6:05	21900	2636	130	0.120	7.8	16.1
Still Shot	19-May	6:07	21720	2651	141	0.122	4.3	15.0
Still Shot	19-May	6:34	23340	2810	181	0.098	4.3	11.6
Still Shot	19-May	6:50	24300	2834	177	0.025	4.5	11.9
Thermal Orthomosaic	19-May	12:15	43800	3946	123	0.057	4.6	17.2
Drone Orthomosaic	19-May	22:32	80820	5347	119	0.038	5.0	17.7
Drone Orthomosaic	19-May	22:45	81600	5392	86	0.057	13.2	24.1

Other physical parameters

Fissure Length (m)	Flow Thickness (m)	Flow Area (m^2)	Flow Volume (x10^5 m^3)	q (m^3 m^{-1} s^{-1})	Q (m^3 s^{-1})
306	3 ±1	597326	34.62 - 46.12	0.1385	34.7566

flow at a higher rate. However, the analytical theory we are applying is relevant to initial propagation, rather than expansion by break-outs, so we do not model this behavior. At the end of the initial advance, the flow achieved a length of 2260 m; subsequent expansion increased the flow length to 2340 m before all activity at the fissure ceased (Table 4.4).

F20/22 opened at around 18:30 HST on 5/17 (C. Parcheta, pers. comm.), and the first 24 hours or so of the fissure's eruptive life was characterized by lava ponding near the fissure. A small flow propagated along the northern rampart of the fissure during the day of May 18, but the main, ocean-bound flows started on May 19, around 00:00 HST based on thermal satellite observations from the Visible Infrared Imaging Radiometer Suite (VIIRS) and estimates of flow front velocity (Appendix B). Approximately 22 hours later, the eastern branch of the flow reached the ocean after traveling 5400 meters (Table 4.5).

The three selected lava flows differ with respect to SiO_2 wt. %, temperature, crystal content, vesicularity, and average effusion rate (Tables 2-5). The F20/22 flow represents the most fluid and voluminous of the flows, with low SiO_2 (52.1 wt. %) and crystallinity (8.3 vol. %), and high vesicularity (53 vol. %), temperature (1121 °C), and average effusion rate (34.8 m^3 s^{-1}). The F17 flow is the most viscous of the flows, with high SiO_2 (56.9 wt. %) and crystallinity (24.1-45.6 vol. %), and low vesicularity (1.1-11 vol. %) and temperature (1071 °C). The F17 flow was longer than the EF8 flow, reflecting the higher average effusion rate (13.1 m^3 s^{-1}) and longer duration. The EF8 flow is less viscous than the F17 flow, due to the lower SiO_2 (51.6 wt. %) and higher temperature (1117 °C), though the crystal content (26.5-80.1 vol. % for EF8) and vesicularity (2.8-3.8 vol. % for EF8) are similar. However, the low average effusion rate (3.7 m^3 s^{-1}) and short duration ensured that the flow was relatively short.

4.4.2 Modeling results

Following Lyman and Kerr (2006), the "dominant" restraining force regulating flow advance is that which predicts the shortest length for a given time. Changes to the flow properties through cooling and crust growth produce transitions in dominant restraining force through time and space. We present the results of first the LK equations then the CEA equations. Two criteria are used to assess whether a set of calculations describes a flow well: (1) whether the calculation matches the final flow length and (2) whether the calculation produces the observed time-length curve.

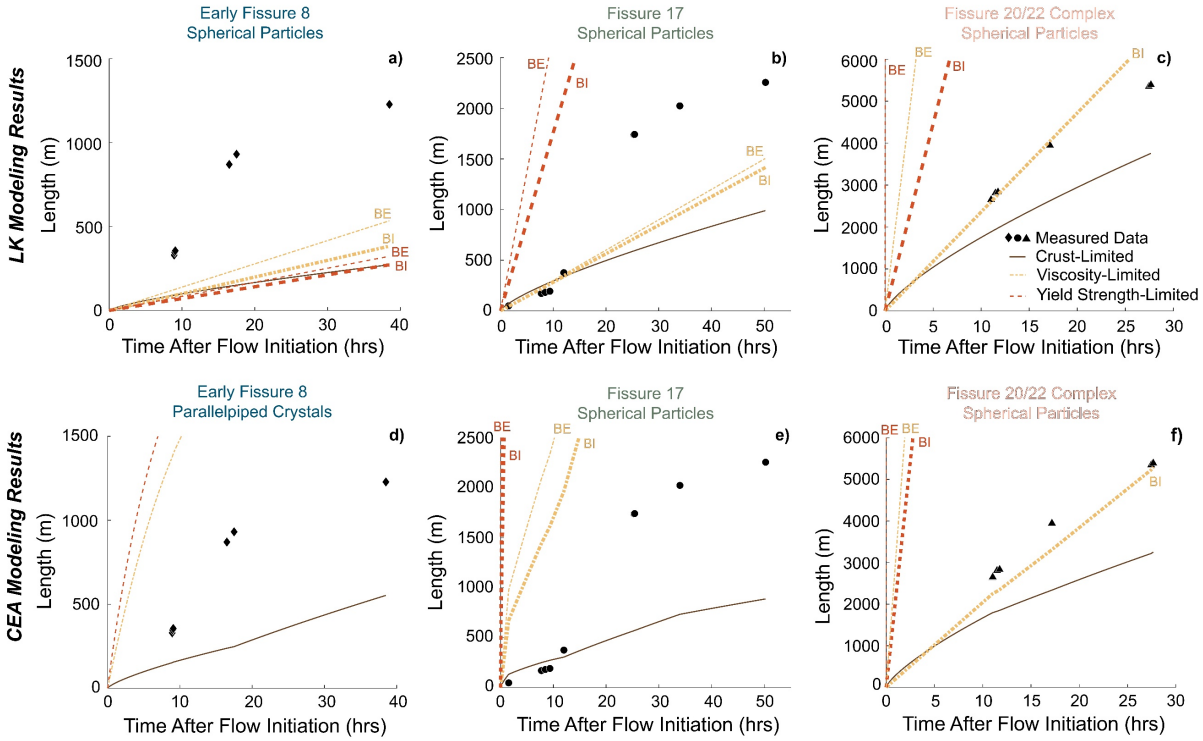

Figure 4.6. Best-fitting results for the calculations for each flow, labeled with the particle treatment. Thicker lines represent calculations that incorporated vesicles (BE = bubbles excluded, BI = bubbles included) into the total particle fraction. The final lengths of all flows are underpredicted, even for these best-fitting scenarios.

4.4.2.1 Early fissure 8

For the LK calculations, dominant restraining force is strongly dependent on whether particles are incorporated (Fig. 4.6; Fig. B-S3). In the crystal-free calculations, crust is the

dominant stopping force, predicting a final length of 272 m; this greatly underpredicts the final flow length of 1230 m. Incorporation of particles into the calculations results in a more complex interplay between the different regimes, particularly when considering the inclusion/exclusion of bubbles as solid particles in the yield strength regime calculation. If bubbles behave as solid particles, then yield strength is the dominant regime for the entirety of the flow, though the final flow length is the same as that predicted by the crust regime (Fig. 4.6). If bubbles do not behave as solid particles, and thus are excluded from the calculation, then yield strength is the dominant regime for the first ~20 hours of the flow and then crust dictates the propagation of the final half of the flow (Fig. 4.6). For calculations incorporating parallelepiped crystals, viscosity controls flow propagation. Final flow length is predicted as 188 m, even shorter than the crust calculation. On the basis of overall fit, as determined by the root mean square deviation (RMSD) calculated at each measured point, the best fitting set of calculations is produced using the spherical particles assumption, but all calculations greatly underpredict final flow length (Table 4.6). None of the calculations generate a curve that is similar to the time-length data.

The CEA calculation results are less dependent on particle treatment (Fig. 4.6; Fig. B-S4). For all calculations, crust is the dominant regime and predicts a final length of 553 m. Although this is still an underprediction of the final flow length, it is less so than the LK model. Both viscosity and yield strength overpredict the final flow length, even with the incorporation of particles. The best fit solution is obtained from the calculations that incorporate parallelepiped crystals. None of the models track the flow propagation in time adequately (Table 4.6).

4.4.2.2 Fissure 17

The general shape of the time-length curve is sigmoidal, and the LK models do not replicate its shape (Fig. 4.6). However, the first 10 hours of the flow are better approximated

Table 4.6. Modeling results

Constant Effusion Rate - LK Equations

	Crust		Viscosity							
			Crystal-Free		*Spherical Particles*		*Spherical Particles - Includes Bubbles*		*Parellelepiped Crystals*	
Fissure	Final Length (m)	RMSD	Final Length (m)	RMSD	Final Length (m)	RMSD	Final Length (m)	RMSD	Final Length (m)	RMSD
EF8	272	611	3929	1270	535	502	383	574	188	670
F17	990	702	10407	3273	1416	575	1506	541	499	934
F20/22	3756	1764	57182	24739	51676	22002	6526	1021	50655	21494

Constant Effusion Rate - CEA Equations

	Crust		Viscosity							
			Crystal-Free		*Spherical Particles*		*Spherical Particles - Includes Bubbles*		*Parellelepiped Crystals*	
Fissure	Final Length (m)	RMSD	Final Length (m)	RMSD	Final Length (m)	RMSD	Final Length (m)	RMSD	Final Length (m)	RMSD
EF8	553	488	17639	7777	3261	1635	2724	1313	2037	983
F17	888	726	20138	7766	9575	3538	7090	2249	7383	2635
F20/22	3253	1960	89915	41533	81257	37174	5300	1353	79652	36366

Variable Effusion Rate - CEA Equations

	Crust		Viscosity				Yield Strength			
			Spherical Particles		*Spherical Particles - Includes Bubbles*		*Spherical Particles*		*Spherical Particles - Includes Bubbles*	
Fissure	Final Length (m)	RMSD	Final Length (m)	RMSD	Final Length (m)	RMSD	Final Length (m)	RMSD	Final Length (m)	RMSD
EF8	1221	27	6594	3917	5429	3182	8984	5235	7319	4074
F17	2272	88	18322	7691	13516	5274	130140	65388	75294	35894
F20/22	5154	874	110290	52000	7194	818	22113000	11705844	77049	37016

Table 4.6. Continued

Constant Effusion Rate - LK Equations

	Yield Strength							
	Crystal-Free		*Spherical Particles*		*Spherical Particles - Includes Bubbles*		*Parellelepiped Crystals*	
Fissure	Final Length (m)	RMSD	Final Length (m)	RMSD	Final Length (m)	RMSD	Final Length (m)	RMSD
EF8	1157100	588232	323	604	272	628	323	604
F17	373030	155478	13773	4683	8847	2621	13773	4683
F20/22	183730000	91423813	7082800	3520813	24679	8596	7082800	3520813

Constant Effusion Rate - CEA Equations

	Yield Strength							
	Crystal-Free		*Spherical Particles*		*Spherical Particles - Includes Bubbles*		*Parellelepiped Crystals*	
Fissure	Final Length (m)	RMSD	Final Length (m)	RMSD	Final Length (m)	RMSD	Final Length (m)	RMSD
EF8	10465000	4664615	3679	1645	2991	1161	3679	1645
F17	1040600	489569	50572	27732	26972	12733	50572	27732
F20/22	362590000	190944284	13978000	7357286	48704	21868	13978000	7357286

(Fig. 4.6; Fig. B-S3). The dominant regime is dependent on the method of particle incorporation into the calculations. For the particle-free calculations, the dominant regime for the total duration of the flow is the crust regime, with a predicted final flow length of 990 m. This underpredicts the true final flow length of 2260 m. Once particles are incorporated, viscosity becomes the limiting factor, with the relative dominance of the regime determined by particle shape (i.e., spherical vs parallelepiped). For spherical particles, viscosity-limited flow is the dominant regime for the first ~12 hours and then crust becomes the limiting regime (Fig. 4.6). Viscous flow incorporating spherical particles also is the closest visual fit to the initial propagation of the F17 flow. However, there is little difference between bubble-bearing calculations and crystal-only calculations. Once parallelepiped crystals are incorporated, viscous flow is the dominant regime for the duration of the flow. This regime even further underpredicts final flow length, with a final length of 499 m (Table 4.6). Regardless of particle incorporation, yield strength calculations greatly overpredict flow length, though the fit is improved by increasing complexity of crystal shape (Table 4.6).

With the CEA model, the dominant regime across all times and crystal shapes is the crust regime with a final flow length of 888 meters (Fig. 4.6; Fig. B-S4). Like the LK calculations, the initial propagation of the flow is modeled reasonably well, though the rapid increase in length that started ~10 hours after the flow initiates is not replicated. Regardless of particle shape, both yield strength and viscosity regimes greatly overpredict flow length (Table 4.6).

4.4.2.3 Fissure 20/22

Because the physical properties (e.g., flow width, ground slope) of the fissure 20/22 flow did not vary greatly through time or space, the LK and CEA results are very similar (Fig. 4.6; Figs. S3-S4). For both equation sets, crust strength is predicted to be the dominant regime for the

whole flow in all scenarios, except for calculations that incorporate bubbles as spherical particles. The final length for the LK crust calculation is 3756 m, and the final length for the CEA crust calculation is 3253 m; both are significant underpredictions of the measured flow length of 5400 m (Table 4.6).

Including bubbles into the spherical particle calculations produces curves that predict the initial ~5 hours of the flow is dominated by viscous flow then switches over to a crust-dominated flow regime. The viscous flow regime calculation produces a final flow length within 100 m of the measured value (5300 m vs 5400 m) for the CEA calculations, though flow propagation is generally underestimated. For the LK calculations, flow propagation is visually well modeled until the inflection point in the time-length data at ~17 hours. The final flow length is overestimated in the LK viscous flow regime at 6526 m (Table 4.6).

4.5 Discussion

Although our modeling of flow propagation does not describe the lava flows from EF8 and F17 adequately, general trends in dominant regimes based on composition and crystallinity are comparable to previous studies (Kerr and Lyman, 2007; Castruccio et al., 2013). The poor fit for the EF8 and F17 flows likely stems from the fact that effusion rate and even vent location was not constant during these flows, yet we treated them as such. Previous work highlights the significant impact of effusion rate on lava flow propagation (e.g., Walker et al., 1973; Harris et al., 2007; Tarquini and de' Michieli Vitturi, 2014; Harris and Rowland, 2015). Therefore, we explore the impact of allowing effusion rate to vary through time in additional calculations. The results of these additional calculations, coupled with the initial constant effusion rate calculations, offer insights into three-phase flow. However, the tested equation sets are not comprehensive in accounting for conditions in nature; many other natural complexities have a

demonstrated influence on lava flow propagation, such as irregular topography and surface roughness (Rumpf et al., 2018; Richardson and Karlstrom, 2019), interactions with trees (Chevrel et al., 2019; Biren et al., 2020), and natural obstacles that cause flows to branch (Hamilton et al., 2013; Dietterich and Cashman, 2014; Dietterich et al., 2015). Innovations in technology, such as unoccupied aircraft systems (UAS), can provide aid to improve observations of lava flows and provide constraints on important parameters, such as effusion rate (Patrick et al., 2019; Dietterich et al., 2021).

4.5.1 Comparison with other lava flows

For all of the flows considered using equation sets, the crust is a dominant restraining force during some or all of the propagation (Fig. 4.6). The flows from EF8 and F17 are also predicted to have early stages dictated by viscosity or yield strength when using the LK equation set. However, as our model of yield strength is likely an overestimate, it is more likely that viscosity plays the dominant role in the early propagation of EF8. For the F20/22 flow, both the CEA and LK equation sets predict that the early part of flow propagation is dominated by bubble-bearing viscosity which then transitions to crust-limited.

The dominance of crust in determining flow propagation for the more evolved lavas erupted from EF8 and F17 is consistent with results from Kerr and Lyman (2007) and Castruccio et al. (2013). Both Kerr and Lyman (2007) and Castruccio et al. (2013) find that the propagation of the andesitic lava flow from Lonquimay in 1988-1989 is fit best by crust strength as the dominant restraining force. Additionally, Castruccio et al. (2013) finds that the more crystal-rich basaltic flows from Etna, Italy in 2001 and 2006 are fit best by an initial phase in which bulk viscosity restrains the flow that later transitions to a phase in which crust strength restrains the flow. Both of these cases (Lonquimay and Etna) are most analogous to the EF8 and F17 flows,

and we note similar restraining forces inferred for these flows, although the flow propagation itself was not well-fit with our modeling conditions.

Best modeling results were achieved with the flow from F20/22. Although the interplay of forces predicts that crust determines the final flow length, the data were reasonably well-fit by the viscosity-limited regime that includes bubbles for both LK and CEA calculations. This is consistent with results from Castruccio et al. (2013). They find that basaltic flows with high effusion rate and low crystal content from Pu‘u ‘Ō‘ō (episodes 11 and 17) are fit well by viscosity-limited flow.

4.5.2 Influence of time-variable effusion rate

If we assume that the equations themselves adequately describe the physics of lava flow propagation, then the general misfit of the earlier modeling must be attributed to our treatment of effusion rate or to limiting assumptions for the source parameters. To test whether varying effusion rate could improve the fit of the initial calculations, we back-solved iteratively for instantaneous discharge rate curves (Harris et al., 2007) that adequately fit the time-length data. The plausibility of the derived effusion rate curves was evaluated by comparison with qualitative observations of the imagery and similarity to previously observed patterns of effusion rate through time (Wadge, 1981; Bonny and Wright, 2017). Changes in effusion rate with time often

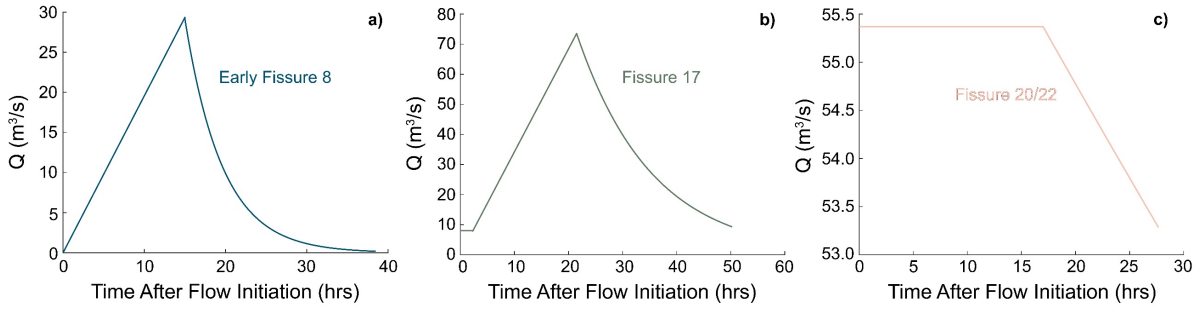

Figure 4.7. Variable effusion rate curves constructed for each flow. The criteria used to construct these curves are based on qualitative observations of the flows and described in detail in Appendix B. These relationships were subsequently used to calculate length versus time relationships for each flow.

reflect changes to magma supply at depth and pressure changes within the magma reservoir (Wadge, 1981; Anderson and Poland, 2016; Bonny and Wright, 2017). This "Wadge-type" effusion rate curve (i.e., rapid initial increase to a maximum, then subsequent exponential decrease) was used for the EF8 and F17 flows as it reflects the proposed mechanism during phase 1 of the eruption of ejecting magma from pressurized pockets (Gansecki et al., 2019), and pressure within the magma pocket decreasing as the supply is erupted (Wadge, 1981; Harris et al., 2000). Many eruptions exhibit more complex patterns in effusion rate (Bonny and Wright, 2017), but this idealized pattern requires the fewest assumptions while still fitting the data. Potentially, the F20/22 overall effusion pattern follows a similar trend, but for the window of time we consider, the best fit to the data is achieved through an essentially constant effusion rate. The effusion rate trends are generally within previously estimated values for the different eruption phases, with phase 1 effusion rates ~3-6 m^3/s increasing to ~65 m^3/s during phase 2 (Plank et al., 2021; Dietterich et al., 2021). It is important to note that these studies collected total rates are for all active fissures, and the temporal resolution is lower than what we are trying to resolve.

For this test, the best-fitting scenarios from the initial calculations were used to calculate length versus time. Insufficient data are available to create robust effusion rate curves with time. However, there are qualitative differences in effusion rate, both variance through time and total output, apparent from the images (Appendix B). Incorporating these curves (Fig. 4.7) into the model calculations produced qualitatively good fits to the time-length data.

The Wadge-type effusion rate curve was able to produce the sigmoidal shape of the time-length curves for the EF8 and F17 flows that the constant effusion rate was unable to replicate (Fig. 4.8). However, only the crust regime is capable of fitting the data. With the additional flux

at earlier times in the flows' propagations as compared to the constant effusion rate case, the viscosity and yield strength regimes greatly overpredict flow length. The calculations for F20/22 deviated slightly from the calculations for EF8 and F17 due to the relative fit produced by incorporating bubbles into the viscous flow regime in the initial calculations. We find that the first ~10 hours of the F20/22 flow are predicted to be dominated by viscous flow, and the rest of the flow propagation is dominated by the crust. The slight decrease in effusion rate is needed to replicate the inflection point in the slope of the data at ~17 hours.

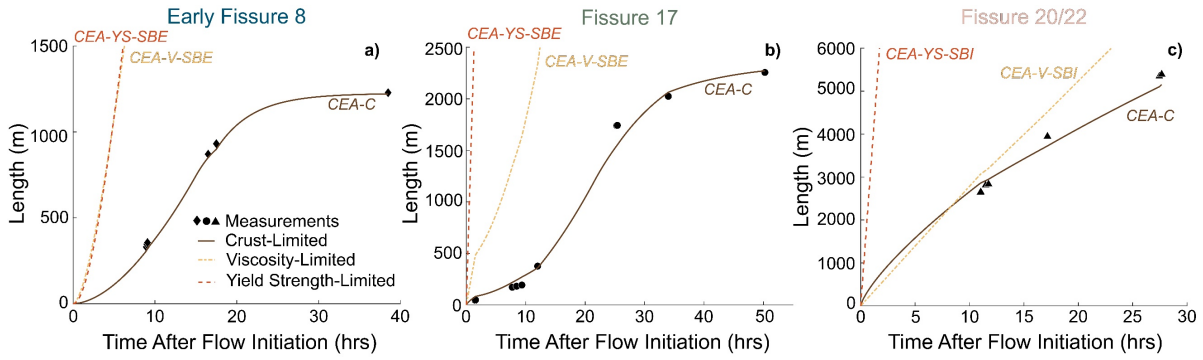

Figure 4.8. Calculated length vs time curves for each flow using the variable effusion rate relationships displayed in Fig. 4.7. Abbreviations next to each curve indicate the scenario in Fig. 4.5 used to calculate the line. Note that the conditions used for F20/22 are slightly different than those used for EF8 and F17 Variable effusion rate is able to reproduce the sigmoidal shape of the measured data.

Although we find that incorporating a variable effusion rate improves the modeling results, this approach requires the inherent assumption that the equations themselves were adequate to describe the flows, an assumption we were unable to test without better estimates of effusion rate variations. Most importantly for hazard management, a constant effusion rate simplification tended to produce an underestimate of flow length. For flows from Mauna Loa, Rowland et al. (2005) find that using double the average effusion rate, or half the initial effusion rate for cases that start with very high effusion, produces good fits to length data. However, this was tested on longer-lived effusion than either EF8 or F17, so this approximation would be more

relevant for the F20/22 case. Measurements of changing effusion rate during an eruption are needed for truly reliable flow propagation models for short-lived effusion.

4.5.3 Implications for controls on three-phase flow propagation

Our calculations demonstrate that incorporation of vesicles into viscosity calculations can improve model fits. The F20/22 flow was best fit by those viscosity-limited equations, both LK and CEA, that incorporate vesicles as solid spheres (Fig. 4.6). Even the early propagation of the F17 flow was fit well visually by the LK equations using a constant effusion rate and including vesicles in the viscous flow calculation. Considering the vesicles in these lavas are relatively spherical (Fig. 4.5), this observation is consistent with previous studies of vesicle impacts on lava viscosity (e.g., Manga et al., 1998; Rust and Manga, 2002; Soldati et al., 2020).

For the LK calculations with constant effusion rate, we find that treating the average crystal content as spheres produces the best results. Incorporating the parallelepiped shape of the crystals overestimates their impact on both the EF8 and F17 flows, with viscous-limited flow calculations predicting a much shorter flow length than was measured at each time point. For these crystal-rich flows, the combination of higher crystal content at early stages of the flow imposed by using the average crystal content and the greater impact of elongate particles on viscosity (Mueller et al., 2011) creates a serious overestimation of viscosity. However, the lesser impact of spherical particles (Mueller et al., 2011) balances out the higher crystal content.

4.5.4 Simple versus complex models: conditions for usage

The complexity of calculation needed to reproduce accurately the measured time-length curves varies based on the state of the fissure itself during the window of time modeled. The timing of both flows from EF8 and F17 includes both the waxing and waning of effusion rate. Conversely, the flow emanating from F20/22 was active during a period of quasi-stability. The

flow did not begin until after the fissure had been active for >24 hours, and the window of time that we are considering in our modeling does not include the effusion waning phase. Thus, the studied time interval for the F20/22 flow was within a period of relatively stable lava effusion, whereas the EF8 and F17 flows were active within a period of significant variation in lava effusion at short-lived fissures (Neal et al., 2019; Houghton et al., 2021a). We conclude that simplified models and average input values work well during periods of steady-state effusion, but tend to underestimate flow advance rate if effusion rate varies.

For crystal-rich lavas and lavas that experience significant crystallization during flow emplacement, using average crystal content tends to underestimate lava propagation rate, particularly if crystals are parallelepipeds. However, our results are somewhat complicated by the fact that the flows that were crystal-rich were also typically stopped by the crust (Fig. 4.6). The thermal history of these flows that promoted crystallization, increasing from ~25 vol. % at eruption to >40 vol. % at flow terminus (Table 4.2), also promoted the growth of crust, which ultimately impacted the flows before a significant proportion of crystals formed (Fig. 4.6). Thus, we cannot reliably define an optimal crystal content and crystal shape to use with our studied flows; however, our results indicate that modeling crystals as parallelepipeds does not produce any systematic improvement over treating crystals as spheres.

4.5.5 Extrinsic effects on flow propagation

The implementation of the equation sets that we have studied represents a simplified treatment of all the possible complexities in nature. Additionally, the flows from EF8 and F17 were essentially single lobes, though the flow from F20/22 had significant branching (Fig. 4.1). Underlying surface roughness (e.g., Rumpf et al., 2018), interactions with trees (e.g., Chevrel et al., 2019; Biren et al., 2020), and terrain that diverts lava flows (e.g., Hamilton et al., 2013;

Dietterich and Cashman, 2014; Dietterich et al., 2015) are all potential complexities that can influence lava flow propagation and branching.

The impact of all of these factors combined can qualitatively be seen in the outlines of the EF8 propagation (Fig. 4.3). While the flow was propagating in an area that had paved roads, offshoot lobes from the main flow traveled down the roads. Although the bulk of the flow propagated along the path of steepest descent through trees and homes, there was clearly a secondary preferential path along the paved roads. At least two of these lobes are readily apparent in our aerial observations (Fig. 4.3), and they correspond to when the flow encountered a road, even when the road is at an oblique angle to flow direction. Similar propagation patterns were observed during the 1973 eruption on Heimaey, Iceland (Williams and Moore, 1983). Smoother surfaces allow for easier flow spreading (Rumpf et al., 2018; Richardson and Karlstrom, 2019), so paved roads represent routes of faster flow propagation. This phenomenon presents a somewhat unique hazard in populated areas; these rapidly advancing lobes oblique to the main flow advance are a risk to people attempting to evacuate a lava inundation area.

The other two flows, emanating from F17 and the F20/22 complex, propagated primarily through sparsely inhabited, densely forested land. As demonstrated by Chevrel et al. (2019) and Biren et al. (2020), lava-tree interactions can enhance cooling and, if the trees are densely packed, lava trees can become obstacles. Their results pertain to pāhoehoe flows, however, as ʻaʻā flows do not typically leave behind lava trees to study. For the dense coverage of trees through which both these flows propagated, it is certainly possible to imagine that the base of the flow was influenced by the increased surface roughness imposed by bulldozed trees. This is coupled with the results of Rumpf et al. (2018), which indicate that rough surfaces (such as those produced by bulldozed trees) also enhance cooling and subsequent crystallization by increasing

the surface area available for conductive cooling. Rumpf et al. (2018) find a complex relationship between surface roughness and apparent lava viscosity, with a maximum increase in apparent viscosity by a factor of four. Thus, the viscosities used in our calculations may be underestimates as we do not account for any surface roughness.

4.5.6 Utility of UAS for critical lava flow measurements

Lava flow monitoring has improved greatly in the past few years with the use of aerial observations to track lava flow evolution (e.g., Patrick et al., 2017; Turner et al., 2017; De Beni et al., 2019). UAS have gained increasing use in volcanological monitoring due to their utility for monitoring hazardous phenomena with exceptional resolution as compared to space-based observations (James et al., 2020), and without the risks and higher costs associated with piloted aviation. Additionally, UAS are not impacted by cloud cover, which can make satellite observations challenging to use. UAS were utilized to monitor the 2018 eruption with great success, accomplishing many tasks such as aiding ground crews, monitoring flow propagation direction, and conducting gas emission measurements (Zoeller et al., 2018). Although UAS were primarily utilized for qualitative observations in the early, chaotic phases of the eruption, the reactivated fissure 8 and its corresponding lava flow were observed extensively with UAS to determine changes in flow velocity and channel dynamics (Patrick et al., 2019; Dietterich et al., 2021). These parameters were used to calculate effusion rate at variable time intervals to constrain the effusion rate variations through time (Dietterich et al., 2021). Many of the early qualitative UAS observations are also used now for more quantitative analysis, as in this study. Incorporating UAS monitoring earlier in an eruption crisis can help provide better constraints on effusion rate variations. As noted in our study and many others (e.g., Walker et al., 1973; Harris et al., 2007; Tarquini and de' Michieli Vitturi, 2014; Harris and Rowland, 2015), constraints on

effusion rate are critical for accurate lava flow propagation forecasting, and UAS are the tools needed for future eruptive crises. Although thermal observations from UAS were not quantitatively used in this study, these observations would be useful for models that use 2D and 3D characterizations of thermo-rheologic evolution of lava flows. UAS are flexible tools that can be used to collect many critical data streams for lava flow hazard mitigation, and should be deployed at the start of an eruption crisis.

4.6 Conclusion

We present analyses of three lava flows from the 2018 eruption of Kīlauea and model the length vs. time evolution of the flows. We used two equation sets that utilize simple physics of three potential flow-stopping forces, viscosity, yield strength, and crust strength. Our strategy pursues two goals: (1) to test the versatility of simple equations to provide a useful analysis for future eruptive crises and (2) to infer the dominant rheological parameters for the studied flows. Based on the equations of Lyman and Kerr (2006) and Castruccio et al. (2013), we find that the simpler calculation of Lyman and Kerr (2006) is reasonably accurate for steady-state flows, such as the flow from F20/22. For the data that includes both the waxing and waning phases of a fissure, like EF8 and F17, neither set of equations can reasonably reproduce the measured length vs. time relationship without *a posteriori* information about the temporal evolution of effusion rate. Our calculations suggest the evolution of both the EF8 and F17 flows were predominantly controlled by the crust; by contrast, the evolution of the flow from F20/22 was predominantly controlled by a combination of viscosity and crust. However, general fits to the data were poor for EF8 and F17 when using an average effusion value. Modeling fits were greatly improved when reasonable variations in effusion rate trends were incorporated, *a posteriori*. The sensitivity of flow propagation rate on effusion rate emphasizes the need for such data in accurate lava flow

propagation forecasting. Future effusion rate measurements can potentially be conducted with greater temporal resolution with the utilization of UAS, as has been demonstrated by recent studies.

Chapter 5. Conclusions

5.1 Summary

Accurate modeling of volcanic processes has important ramifications for hazard preparedness and mitigation. In this dissertation, I examine two properties that influence the hazards associated with high silica magmas and low silica magmas – the rates of silicic magma decompression and basaltic lava flow propagation. An overarching dilemma that is present in all modeling situations is what is the level of model complexity needed to accurately represent the process of interest? The results from each dissertation chapter address this dilemma for a given situation and offer guidance for future researchers.

Chapter 2 demonstrates that certain simplifications to diffusion models used to quantify volatile diffusion in melt embayments are acceptable, while others introduce significant errors to the calculated decompression timescale. Specifically, decompression can be treated as isothermal in all cases with little impact on calculated decompression timescales. However, using 1D diffusion profiles when significant (>40% constriction) exists at the embayment mouth can introduce non-negligible error into calculated timescales if the diffusion front is out of the necked region of the embayment. Additionally, simplifying the degassing behavior to equilibrium conditions can introduce significant error to calculated timescales when disequilibrium conditions are present.

Chapter 3 provides a first experimental comparison of two decompression rate meters as an initial step towards quantifying the decompression rate variation within an eruption. Constraining decompression rate variations within a given eruption in natural systems offers the benefit of better understanding of the conditions that can cause shifts in eruptive behavior. In this initial test of the experiments, both studied decompression rate meters, bubble number density

and diffusion of water, are able to produce useful decompression rates. However, the results are sensitive to assumptions made about bubble nucleation style. Experimental studies have the advantage of knowing the input parameters, but application of models to natural systems becomes complicated when many parameters are unknown.

Chapter 4 examines sloping viscous theory as a method for predicting lava flow propagation with flows from the 2018 eruption of Kīlauea. Various levels of calculation complexity are examined, including the time-dependence of flow material properties (e.g., viscosity and yield strength) and external properties (e.g., ground slope), the assumed crystal shape and down-flow increase in crystal concentration, and the temporal resolution of variations in lava effusion rate. The results suggest that the largest source of error in reproducing the propagation of the studied lava flows is associated with poor temporal resolution of effusion rate variations. Steady-state or quasi-steady-state effusion can be well approximated by using average values for all other properties, but no amount of complexity in the other studied parameters can produce observed lava propagation if an average effusion rate value is applied to highly variable effusion.

5.2 Future directions

The results from this dissertation have highlighted areas where additional work can be conducted to great benefit of the geologic community. For Chapter 2, although certain 3D embayment geometries are not suited for current 1D studies, additional 3D modeling can be utilized to create correction factors that will allow researchers to correct 1D-derived decompression rates to account for non-ideal geometries. Embayments can be rare in nature, so expanding the usable geometries is important to ensure melt embayment modeling continues to be a useful petrologic tool. For Chapter 3, additional experiments are needed to test fully the

utility of the coordinated decompression rate meter approach. Ideally, these additional experiments would use a two-step decompression to test whether the different decompression rate meters are recording the expected rates. An important remaining question for both Chapters 2 and 3 is the question of bubble nucleation style. Resolving the conditions under which homogeneous versus heterogeneous nucleation are predominant is critical to leveraging correctly both bubble number density and volatile diffusion to calculate decompression rate. The results of Chapter 4 highlight the need for high temporal resolution of lava effusion rate measurements to forecast accurately lava flow propagation. Flows that are fed by sources with highly variable effusion rate cannot be accurately forecasted without knowledge of the effusion rate variations. Unoccupied aircraft systems (UAS) were utilized to great effect at the end of the 2018 Kīlauea eruption to quantify effusion rates, so they are an ideal tool for future eruptive crises. These types of effusion rate measurements should be high priority for hazard managers, particularly in rapidly changing crises when it is unknown whether effusion rate will vary at a given vent.

Appendix A: Chapter 2 Supplementary Material

Numerical vs. analytical solution, stability criterion, and profile fitting

Analytical vs numerical solution of 3D diffusion

Numerical solutions for diffusion are approximations that need to be checked against analytical solutions. However, analytical solutions are limited in their applicability because they cannot easily deal with the geometric complexity of objects like embayments (Fig. 2.1). Nevertheless, we can show that our numerical solution is a reasonable approximation for the

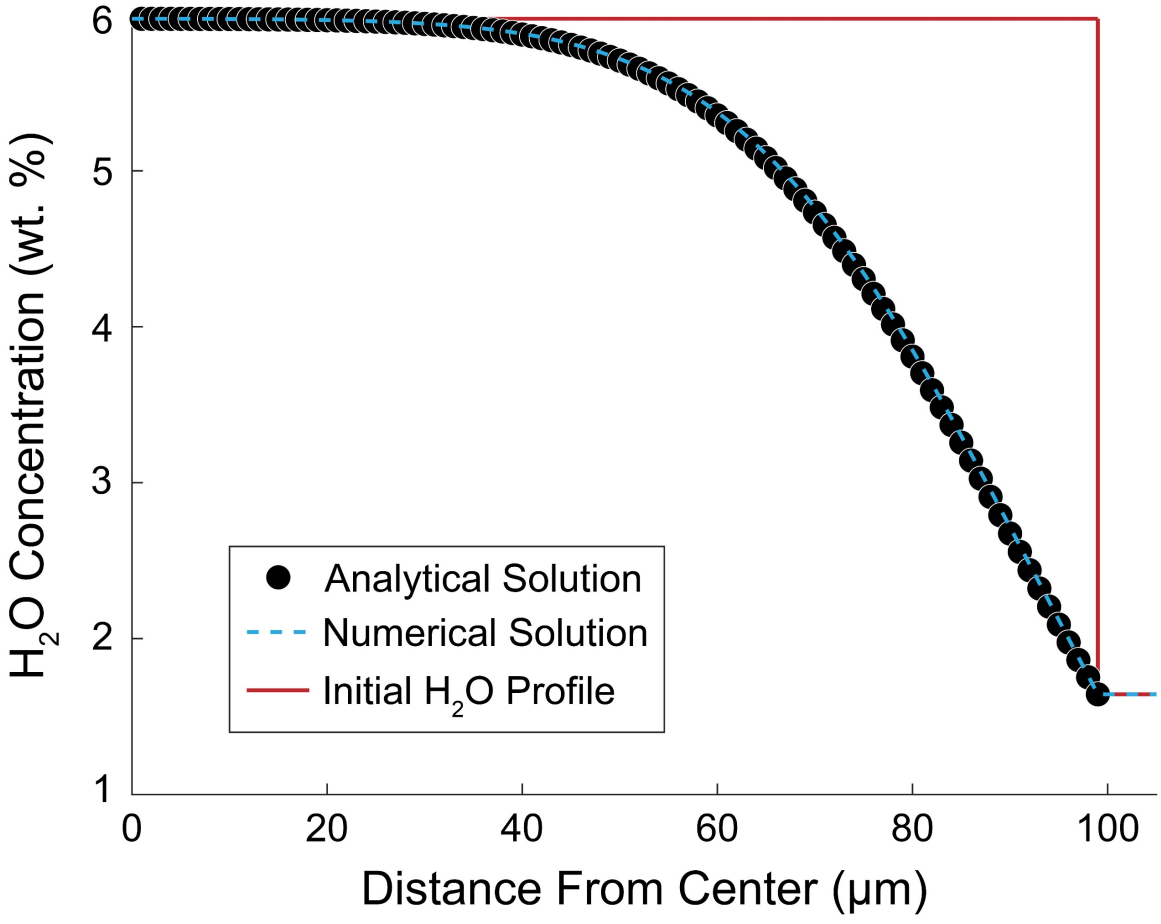

Figure A-S1. Comparison of profiles produced by solving for diffusion in a sphere using an analytical and numerical solution. The two are in excellent agreement, so the numerical solution is considered to be an acceptable approximation in subsequent analysis.

analytical solution, though, by comparing our 3D numerical solution for a sphere to the analytical solution for a radial profile through a sphere. We use the solution of Crank (1975) for diffusion in a sphere:

$$\frac{C - C_1}{C_0 - C_1} = 1 + \frac{2a}{\pi r}\sum_{n=1}^{\infty}\frac{(-1)^n}{n}\sin\frac{n\pi r}{a}exp(-Dn^2\pi^2 t/a^2) \qquad (A1)$$

And the concentration at the center of the sphere is given by:

$$\frac{C - C_1}{C_0 - C_1} = 1 + 2\sum_{n=1}^{\infty}(-1)^n exp(-Dn^2\pi^2 t/a^2) \qquad (A2)$$

In these equations, C is the concentration at time t at a given distance from the center r, C_1 is the initial water content, C_0 is the final water content, a is the total radius of the sphere, and D is diffusivity. Although this solution is not explicitly 3D, it was derived such that it accounts for complex flux pathways in the other dimensions. Thus, it is an appropriate comparison to our 3D numerical solution.

For the main 3D embayment diffusion model, we use the solubility relationship of Liu et al. (2005) to relate pressure and water content. The initial pressure is 200 MPa, and the final pressure is 20 MPa. For diffusivity we used the maximum diffusivity, calculated using the model of Ni and Zhang (2008) at 200 MPa and 800 °C. The test sphere was made with a total radius of 100 μm with a step size of 2 μm. The summation was evaluated over 20 iterations (n=20), sufficient to converge on a solution.

We ran the two models for a total duration of 30 seconds and compared the profiles produced. The difference between the numerical and analytical solutions is negligible (Fig. A-S1), so we consider our numerical solution to be a good approximation. Our 3D numerical

solution was also previously tested against a 3D analytical solution for diffusion in a parallelepiped by Shea et al. (2015), using the derivation of Crank (1975). However, a limitation of the applicability of both of these analytical solutions is that they do not allow for concentration-dependent diffusivity.

Explicit finite differences solution and its stability

The centered finite differences solution to 1D diffusion, accounting for concentration-dependent diffusivity can be written as:

$$C_i^{t+1} = C_i^t + \Delta t \left[\left(\frac{C_{i+1} - C_{i-1}}{2\Delta x} \right) \left(\frac{D_{i+1} - D_{i-1}}{2\Delta x} \right) \right] + D_i \Delta t \left(\frac{C_{i+1} - 2C_i + C_{i-1}}{\Delta x^2} \right) \qquad (A3)$$

In this case, C is is concentration in wt. %, D is diffusivity in $\mu m^2\ s^{-1}$, Δx is the spacing between grid points in the x-dimension in μm, Δt is the time step between calculation points in s, i is the index position in x, and t is the index position in time. To expand this solution to 3D, additional terms for y- and z-dimensions (j and k indices, respectively) were added to each section. For the fictitious points boundary conditions, the finite differences solution for each boundary pixel was evaluated on a case-by-case basis. In order to "reflect" the flux so that it does not enter the host crystal during modeling, the finite differences solution for each boundary pixel was modified. Either the forwards (i+1) or backwards (i-1) concentration was set to equal to each other (i.e., $C_{i+1} = C_{i-1}$) and the finite differences solution simplified using that substitution. This could be applied to 3D by incorporating terms for y and z as well.

Stability of explicit finite differences solutions can be ensured using the following criterion:

$$R = \frac{D \times \Delta t}{\Delta x^2} \qquad (A4)$$

where D is diffusivity in μm2/s, Δt is the change in time between each calculation iteration in seconds, and Δx is the grid spacing between points. To ensure stability, R must be less than 0.5. In our models, we calculate Δt such that the solution is stable at the starting D and Δx conditions (R=0.3 for 1D models and R=0.125 for 3D models).

Profile fitting methods

Profile fitting was conducted as an iterative process (Fig. A-S2). The duration range for each subsequent fitting step was selected to completely bracket the duration with the minimum RMSD. Fitting iterations were conducted until the best-fitting duration was determined to the

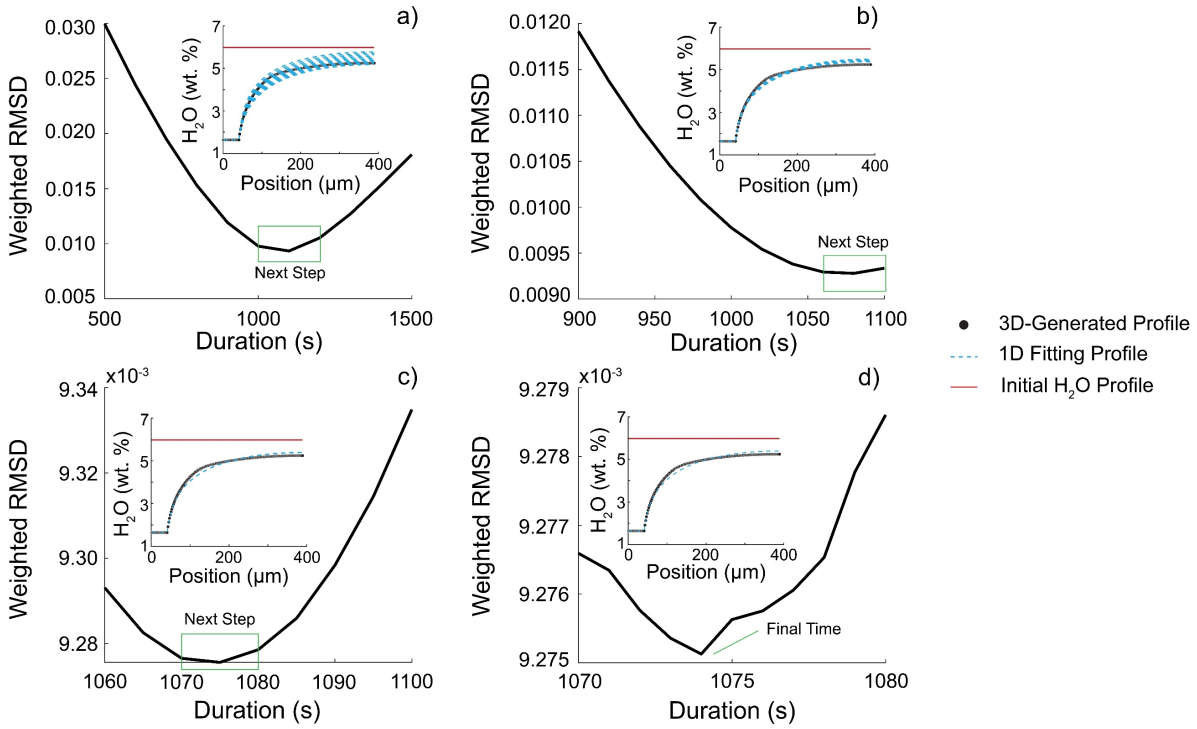

Figure A-S2. Plots of steps to search for best-fitting time, using an example from the 40% necked geometry, with an imposed decompression rate of 0.1 MPa/s. Moving from *a* to *d*, the search range becomes more fine scale. The box labeled "Next Step" in each panel shows the extent of the subsequent panel. Insets in each panel shows the 3D-generated profile, along with the 1D-generated profiles at each tested time. In this case, the final time determined as the 1D best-fitting time is 1074 seconds, compared to the 3D imposed time of 1800 seconds.

nearest second. As seen in the example profile in Fig. A-S2, the 1D fitting model cannot reproduce the exact shape of the 3D profile for the more necked geometries.

Influence of catch-up decompression rate exponent in disequilibrium degassing

The "catch-up" rate of water loss from the melt after a homogeneous nucleation event is poorly constrained. For the purposes of our modeling, we chose a value that produced curves similar to those in the schematic representation of Mangan and Sisson (2000); however, that value has little physical constraint. Here, we demonstrate the impact of varying the catch-up exponent by an order of magnitude on the disequilibrium degassing modeling results.

The models were run with the same parameters as those described in the main text, except the "catch-up" exponent was varied by either increasing by an order of magnitude to 0.03

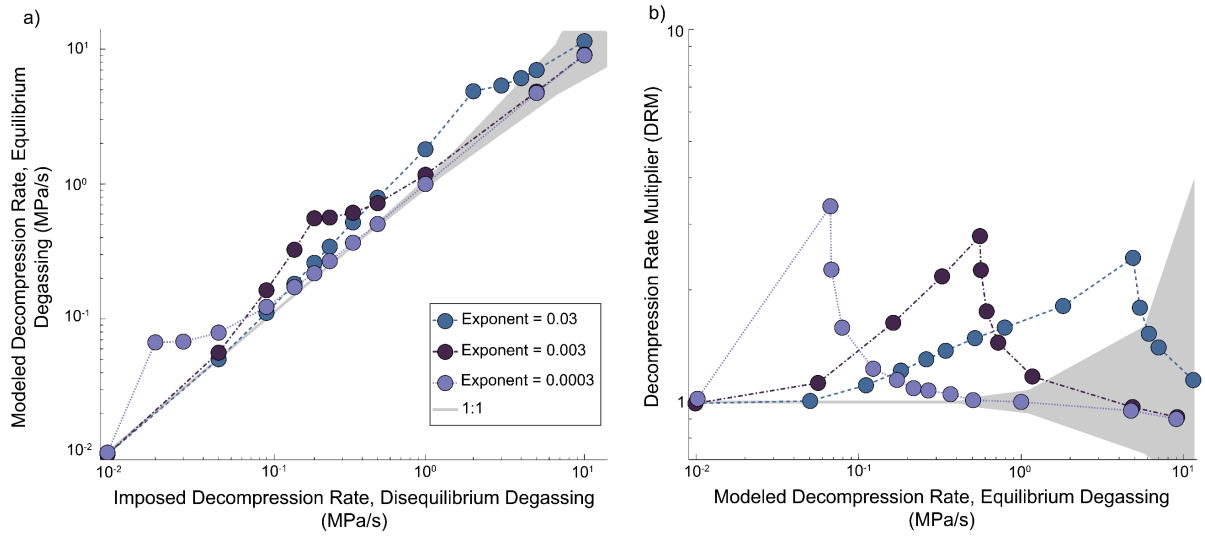

Figure A-S3. Discrepancy in decompression rates calculated assuming equilibrium degassing when degassing occurs under disequilibrium conditions, using different values for the catch-up exponent (Eq. 2.4). All of these models used an initial pressure of 200 MPa and ΔP_N of 100 MPa. Shaded region shows numerical fitting uncertainties estimated to be within ±3 seconds of the imposed decompression rate (where it is larger than the 1:1 line). This ±3 seconds is calculated relative to the apparent final pressure when it is different from the imposed final pressure so that it matches the calculation method of the decompression rate. *a)* Comparison between decompression rates imposed in disequilibrium degassing models and best-fit decompression rates obtained assuming equilibrium degassing. *b)* Best-fit decompression rate obtained by assuming equilibrium degassing against the DRM for each model.

or decreasing by an order of magnitude to 0.0003. The range of imposed decompression rates in the models is comparable to those described in the main text, spanning from 0.01 MPa/s to 10 MPa/s, with extra runs conducted where finer temporal resolution was necessary (Table A-S5).

We find that the value of the catch-up exponent has a significant effect on model results (Fig. A-S3). The position of peak DRM is shifted towards faster modeled decompression rates for larger catch up exponents; conversely, the peak DRM is shifted towards slower modeled decompression rates for smaller catch up exponents. The peak location varies over two orders of magnitude for the three exponent values tested, so the exponent has a strong influence on model results. There also appears to be a dependence of the magnitude of peak DRM on catch up exponent, though it varies by less than one between the three orders of magnitude of exponent tested. Thus, the primary effect of the different catch up exponent is controlling the modeled decompression rate at which the maximum DRM occurs.

Table A-S1. Full summary of geometry model conditions and results

Geometry[a]	Imposed dP/dt (MPa/s)	Imposed Timescale (s)	Modeled Timescale (s)	Modeled dP/dt (MPa/s)	Weighted RMSD	DRM[b]
Cylinder	6	30	30	6.00	0.0001	1.00
Cylinder	1.8	100	100	1.80	0.0003	1.00
Cylinder	1	180	183	0.984	0.0007	0.98
Cylinder	0.5	360	376	0.479	0.0012	0.96
Cylinder	0.1	1800	1936	0.093	0.0012	0.93
Cylinder	0.01	18000	19574	0.009	0.0008	0.92
Cylinder (Flat Back)	0.1	1800	1806	0.100	0.0005	1.00
Cylinder (Flat Sides)	0.1	1800	1940	0.093	0.0012	0.93
20% Necked	6	30	31	5.81	0.0003	0.97
20% Necked	1.8	100	96	1.88	0.0011	1.04
20% Necked	0.75	240	211	0.853	0.0015	1.14
20% Necked	0.5	360	309	0.583	0.0019	1.17
20% Necked	0.3	600	513	0.351	0.0028	1.17
20% Necked	0.1	1800	1572	0.115	0.0036	1.15
20% Necked	0.01	18000	15625	0.012	0.0035	1.15
40% Necked	6	30	31	5.81	0.0009	0.97
40% Necked	1.8	100	84	2.14	0.0028	1.19
40% Necked	0.75	240	157	1.15	0.0035	1.53
40% Necked	0.5	360	216	0.833	0.0042	1.67
40% Necked	0.3	600	340	0.529	0.0061	1.76
40% Necked	0.1	1800	1074	0.168	0.0090	1.68
40% Necked	0.01	18000	11005	0.016	0.0087	1.64
60% Necked	6	30	31	5.81	0.0020	0.97
60% Necked	1.8	100	70	2.57	0.0051	1.43
60% Necked	0.5	360	127	1.42	0.0066	2.83
60% Necked - C.R.[c]	0.5	360	133	1.35	0.0066	2.71
60% Necked	0.35	514	156	1.15	0.0075	3.30
60% Necked	0.25	720	197	0.914	0.0091	3.65
60% Necked	0.2	900	239	0.753	0.0106	3.77
60% Necked	0.15	1200	321	0.561	0.0127	3.74
60% Necked	0.1	1800	519	0.347	0.0150	3.47
60% Necked - C.R.[c]	0.1	1800	483	0.373	0.0211	3.73
60% Necked	0.01	18000	5665	0.032	0.0180	3.18
80% Necked	6	30	34	5.29	0.0048	0.88
80% Necked	1.8	100	59	3.05	0.0091	1.69
80% Necked	0.5	360	77	2.34	0.0119	4.68
80% Necked	0.25	720	89	2.02	0.0112	8.09
80% Necked	0.2	900	96	1.88	0.0114	9.38

80% Necked	0.1	1800	122	1.48	0.0130	14.75
80% Necked	0.08	2250	141	1.28	0.0142	15.96
80% Necked	0.05	3600	216	0.833	0.0180	16.67
80% Necked	0.03	6000	325	0.554	0.0289	18.46
80% Necked	0.01	18000	1334	0.135	0.0314	13.49
80% Necked	0.005	36000	2785	0.065	0.0289	12.93

[a]All listed models were run at a temperature of 800°C, initial pressure of 200 MPa, and final pressure of 20 MPa

[b]Decompression Rate Multiplier

[c]C.R. indicates coarse resolution (spacing of 4 μm) comparison model

Table A-S2. Full summary of disequilibrium model conditions and results

P_i (MPa)[a]	ΔP (MPa)	Apparent Melt P_f (MPa)[b]	Imposed dP/dt (MPa/s)	Expected Timescale (s)	Modeled Timescale (s)	Modeled dP/dt (MPa/s)	Weighted RMSD	DRM[c]
200	100	109	10	9	10	9.10	0.0011	0.91
200	100	108	5	18	19	4.84	0.0009	0.97
200	100	97	1	103	88	1.17	0.0005	1.17
200	100	81	0.5	238	165	0.721	0.0004	1.44
200	100	64	0.35	389	222	0.613	0.0005	1.75
200	100	38	0.25	648	287	0.565	0.0005	2.26
200	100	10	0.2	950	341	0.557	0.0040	2.79
200	100	10	0.15	1267	583	0.326	0.0087	2.17
200	100	10	0.1	1900	1165	0.163	0.0054	1.63
200	100	10	0.05	3800	3380	0.056	0.0015	1.12
200	100	10	0.01	19000	19173	0.010	0.0001	0.99
200	150	160	10	4	5	8.00	0.0005	0.80
200	150	160	5	8	9	4.44	0.0003	0.89
200	150	158	1	42	41	1.02	0.0005	1.02
200	150	155	0.5	90	78	0.577	0.0002	1.15
200	150	152	0.35	137	109	0.440	0.0002	1.26
200	150	149	0.25	204	147	0.347	0.0004	1.39
200	150	145	0.2	275	178	0.309	0.0003	1.55
200	150	139	0.15	407	224	0.272	0.0003	1.82
200	150	123	0.1	770	298	0.258	0.0005	2.58
200	150	94	0.07	1514	366	0.290	0.0007	4.14
200	150	33	0.05	3340	432	0.387	0.0010	7.73
200	150	10	0.03	6333	1684	0.113	0.0069	3.76
200	150	10	0.01	19000	16640	0.011	0.0005	1.14
300	150	157	10	14	15	9.53	0.0014	0.95
300	150	154	5	29	28	5.21	0.0011	1.04
300	150	126	1	174	130	1.34	0.0003	1.34
300	150	81	0.5	438	230	0.952	0.0002	1.90
300	150	29	0.35	774	297	0.913	0.0014	2.61
300	150	10	0.25	1160	542	0.535	0.0110	2.14
300	150	10	0.2	1450	834	0.348	0.0082	1.74
300	150	10	0.15	1933	1387	0.209	0.0052	1.39
300	150	10	0.1	2900	2614	0.111	0.0024	1.11
300	150	10	0.05	5800	5874	0.049	0.0007	0.99
300	150	10	0.01	29000	29255	0.010	0.0001	0.99

[a]All models were run with an imposed final pressure of 10 MPa and temperature of 850 °C

[b]Apparent final pressure based on far field melt water concentration

[c]Decompression Rate Meter

Table A-S3. Full summary of isentropic model conditions and results

Imposed P_f (MPa)[a]	Apparent P_f (MPa)[b]	Imposed dP/dt (MPa/s)	Imposed Timescale (s)	Modeled Timescale (s)	Modeled dP/dt (MPa/s)	Weighted RMSD	DRM[c]
20	21	10	18	19	9.42	0.0058	0.94
10	11	10	19	21	9.00	0.0074	0.90
5	6	10	20	22	8.82	0.0077	0.88
20	21	5	36	37	4.84	0.0059	0.97
10	11	5	38	40	4.73	0.0074	0.95
5	6	5	39	40	4.85	0.0081	0.97
20	21	1	180	170	1.05	0.0035	1.05
10	11	1	190	179	1.06	0.0052	1.06
5	6	1	195	182	1.07	0.0064	1.07
20	23	0.5	360	336	0.527	0.0024	1.05
10	13	0.5	380	348	0.537	0.0036	1.07
5	8	0.5	390	356	0.539	0.0045	1.08
20	21	0.1	1800	1564	0.114	0.0006	1.14
10	11	0.1	1900	1614	0.117	0.0014	1.17
5	6	0.1	1950	1632	0.119	0.0026	1.19
20	21	0.02	9000	7252	0.025	0.0004	1.23
10	11	0.02	9500	7372	0.026	0.0009	1.28
5	6	0.02	9750	7363	0.026	0.0018	1.32

[a]All models were run with initial pressure of 200 MPa and initial temperature of 800 °C

[b]Apparent final pressure is based on far field melt water concentration and an isothermal solubility relationship

[c]Decompression Rate Multiplier

Table A-S4. Full summary of different starting conditions models

Geometry[a]	Max Embayment Water (wt. %)	P_i (MPa)	Imposed dP/dt (MPa/s)	Expected Timescale (s)	Modeled Timescale (s)	Modeled dP/dt (MPa/s)	Weighted RMSD	DRM[b]
Cylinder	5.94	198	1.8	99	94	1.89	0.0014	1.05
Cylinder	5.83	192	1	172	143	1.20	0.0034	1.20
Cylinder	5.55	175	0.5	310	202	0.767	0.0061	1.53
Cylinder	4.36	115	0.1	950	466	0.204	0.0061	2.04
Cylinder	2.73	50	0.01	3000	1408	0.021	0.0045	2.13
20% Necked	5.94	198	0.75	237	198	0.899	0.0018	1.20
20% Necked	5.87	193	0.5	346	247	0.700	0.0030	1.40
20% Necked	5.71	184	0.3	547	320	0.513	0.0040	1.71
20% Necked	5.07	150	0.1	1300	539	0.241	0.0046	2.41
20% Necked	3.27	69	0.01	4900	1669	0.030	0.0043	3.00
40% Necked	5.95	198	0.75	237	147	1.21	0.0036	1.61
40% Necked	5.89	195	0.5	350	182	0.962	0.0039	1.92
40% Necked	5.77	188	0.3	560	226	0.743	0.0042	2.48
40% Necked	5.24	159	0.1	1390	348	0.399	0.0042	3.99
40% Necked	3.47	77	0.01	5700	1112	0.051	0.0030	5.13
60% Necked	5.93	197	0.5	354	117	1.51	0.0065	3.03
60% Necked	5.88	194	0.35	497	127	1.37	0.0067	3.91
60% Necked	5.82	191	0.25	684	142	1.20	0.0066	4.82
60% Necked	5.76	187	0.2	835	147	1.14	0.0067	5.68
60% Necked	5.66	182	0.15	1080	159	1.02	0.0067	6.79
60% Necked	5.50	173	0.1	1530	180	0.850	0.0065	8.50
60% Necked	3.89	94	0.01	7400	482	0.154	0.0057	15.4
80% Necked	5.96	199	0.5	358	75	2.39	0.0111	4.77
80% Necked	5.93	197	0.25	708	81	2.19	0.0114	8.74
80% Necked	5.91	196	0.2	880	85	2.07	0.0114	10.35
80% Necked	5.81	190	0.1	1700	89	1.91	0.0114	19.10
80% Necked	5.76	188	0.08	2100	92	1.83	0.0113	22.83
80% Necked	5.63	180	0.05	3200	98	1.63	0.0111	32.65
80% Necked	5.50	173	0.03	5100	104	1.47	0.0126	49.04
80% Necked	4.88	140	0.01	12000	148	0.812	0.0112	81.10
80% Necked	4.35	115	0.005	19000	202	0.470	0.0096	94.06

[a]All models have the same final pressure of 20 MPa

[b]Decompression Rate Multiplier

Table A-S5. Summary of model runs with a different catch up exponent

Catch Up Exponent[a]	Apparent Melt P_f (MPa)[b]	T (°C)	Imposed dP/dt (MPa/s)	Expected Timescale (s)	Modeled Timescale (s)	Modeled dP/dt (MPa/s)	Weighted RMSD	DRM[c]
0.03	97	850	10	10	9	11.44	0.0011	1.14
0.03	81	850	5	24	17	7.00	0.0004	1.40
0.03	72	850	4	32	21	6.10	0.0009	1.52
0.03	55	850	3	48	27	5.37	0.0018	1.79
0.03	10	850	2	95	39	4.87	0.0062	2.44
0.03	10	850	1	190	105	1.81	0.0162	1.81
0.03	10	850	0.5	380	240	0.792	0.0115	1.58
0.03	10	850	0.35	543	366	0.519	0.0089	1.48
0.03	10	850	0.25	760	554	0.343	0.0068	1.37
0.03	10	850	0.2	950	730	0.260	0.0055	1.30
0.03	10	850	0.15	1267	1044	0.182	0.0040	1.21
0.03	10	850	0.1	1900	1714	0.111	0.0024	1.11
0.03	10	850	0.05	3800	3777	0.050	0.0009	1.01
0.03	10	850	0.01	19000	19173	0.0099	0.0001	0.99
0.0003	110	850	10	9	10	9.00	0.0010	0.90
0.0003	110	850	5	18	19	4.74	0.0007	0.95
0.0003	109	850	1	91	91	1.00	0.0006	1.00
0.0003	108	850	0.5	184	182	0.506	0.0008	1.01
0.0003	106	850	0.35	269	256	0.367	0.0008	1.05
0.0003	105	850	0.25	380	354	0.268	0.0001	1.07
0.0003	104	850	0.2	480	441	0.218	0.0006	1.09
0.0003	101	850	0.15	660	576	0.172	0.0000	1.15
0.0003	97	850	0.1	1030	839	0.123	0.0005	1.23
0.0003	81	850	0.05	2380	1504	0.079	0.0006	1.58
0.0003	54	850	0.03	4867	2149	0.068	0.0001	2.26
0.0003	10	850	0.02	9500	2835	0.067	0.0013	3.35
0.0003	10	850	0.01	19000	18630	0.0102	0.0002	1.02

[a]All models had an initial pressure of 200 MPa, ΔP of 100 MPa, and imposed final pressure of 10 MPa

[b]Apparent final pressure based on far field melt water concentration

[c]Decompression Rate Multiplier

Appendix B: Chapter 4 Supplementary Material

Capillary number calculations

Capillary number (Ca) controls whether bubbles increase or decrease relative viscosity in a silicate melt (Mader et al., 2013; Rust and Manga, 2002). It can be calculated as:

$$Ca = \frac{\eta r \dot{\gamma}}{\Gamma} \qquad (B1)$$

where η is the melt viscosity in Pa s, r is the bubble radius in m, $\dot{\gamma}$ is strain rate in s^{-1}, and Γ is melt-vapor surface tension in N m^{-1}. Here, melt viscosity for each flow is taken from Table 4.2, and surface tension is taken to be 0.3 N m^{-1}, the value for anhydrous silicate melts (Bagdassarov et al., 2000). We used values that would produce the maximum reasonable Ca so as to demonstrate the most likely influence of bubbles in our calculations. Thus, r is taken to be either the mean bubble radius (converting bubble area into the radius of an equivalent sphere), or modal bubble radius, whichever is larger. Strain rate is approximated by dividing the maximum flow front velocity by the average thickness for each flow (Tables 4.3-4.5). Our calculated Ca for each flow is <0.1, so bubbles are predicted to have increased viscosity in our flows (Mader et al., 2013; Table B-S1).

Table B-S1. Capillary number estimations for EF8, F17, and F20/22

Flow	Surface Tension (N/m)	Bubble Radius (μm)	Melt Viscosity (Pa s)	Strain Rate (s^{-1})	Ca
EF8	0.3	8.4	791	0.034	0.0008
F17	0.3	45.4	8031	0.011	0.0134
F20/22	0.3	94.2	657	0.041	0.0085

Image georeferencing

The images captured from helicopter overflights needed to be corrected for the look angle so as to minimize length distortions. Key features in images were correlated with the same features in satellite imagery from DigitalGlobe using QGIS. Only images with sufficient identifying points (e.g., road intersections, houses, distinctive structures) around the flow front were used in data collection and subsequent modeling. Fissure locations in still-shots were correlated with the same features in both the drone and thermal imagery. Offset here refers to the error in locating a feature on the base satellite image and was quantified by measuring the distance between a feature in the satellite image and the same feature's apparent location in the captured image. The EF8 flow was within the Leilani Estates subdivision, so many identifying features are present. Maximum offset between a georeferenced image and the base satellite image is 2-3 meters near the flow front and ~4 meters at the edges of the image. The F17 flow started in and propagated through a more sparsely populated location, so offset around the flow is ~3 meters for the images captured on May 13, and up to 7 meters for the images captured on May 14. The flow field associated with F20/22 covered a large area, and images that included a large area tended to be difficult to georeference, so images that focused only on the flow front were preferentially selected. The path from the vent to the image was measured using the thermal orthomosaic for F20/22. Maximum offset in images around the flow front was ~6 meters.

Start time of F20/22 flow

The start time of lava effusion from F20/22 is relatively well-constrained by ground crews as 18:30 HST on May 17 (C. Parcheta, pers. comm.). However, during the first ~24 hours of the fissure's lifespan, lava predominantly ponded around the fissure, with a small flow extending to the north. The flow that we model was not observed to be heading towards the coast until early in the morning on May 19. Constraints on the true start time of the flow are sparse, so

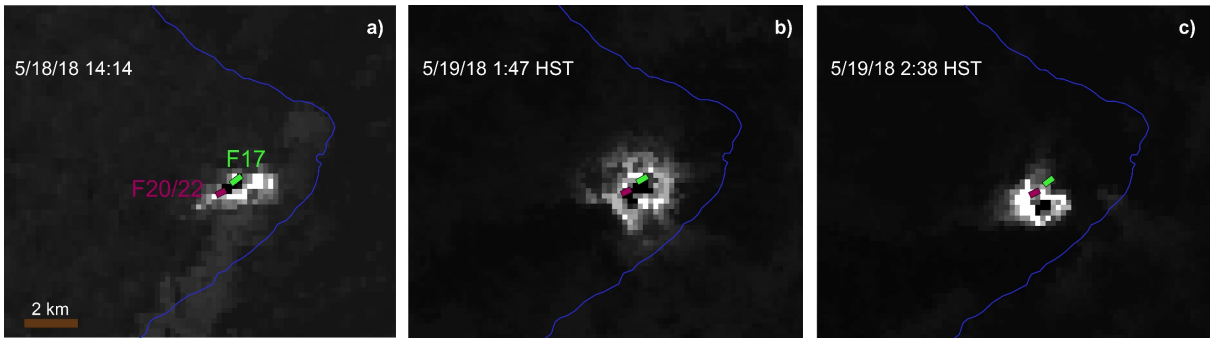

Figure B-S1. Thermal images captured from the VIIRS (Visible Infrared Imaging Radiometer Suite) instrument on two satellites (Suomi National Polar-orbiting Partnership and NOAA-20) overnight between May 18th and 19th. Data were downloaded from NOAA CLASS (Comprehensive Large Array-data Stewardship System), are located in WGS84 UTM Zone 5N, and were processed with satpy, a Python library. Fissure locations of the important active flows are labeled, and the island coastline is shown in blue. Brighter pixels indicate greater heat flow, except for the black pixels in the middle of bright pixels; these pixels are high enough temperature that they saturate the grayscale. Thus, the hottest parts of flows are indicated by black pixels. Over the course of the 12 hours shown, the main locus of activity shifts from the vicinity of F17 to near F20/22 and then farther down the slope as the flow advances.

we approximate a start time based on thermal satellite images captured during the night and estimates of flow front velocity. Two start times are possible based on flow front velocity, as the average velocity of the flow or the flow velocity calculated from the first two length measurements can be used. Using the average flow velocity of 0.066 m/s (Table 4.5), the flow would have initiated at ~19:00 HST on May 18. Using the flow velocity calculated from the first two length measurements of 0.122 m/s, the flow would have initiated at approximately 0:00 HST on May 19. The natural choice is to use the start time associated with the flow velocity that captures the ground slope most similar to the start of the flow, but other data sources were available to corroborate this choice. We also use thermal images captured by the Visible Infrared Imaging Radiometer Suite (VIIRS) during the night (Fig.B- S1). In the image captured at 1:47 HST on May 19, the hottest part of the flow is still relatively close to the fissure source, which would indicate the flow had not been active for long. Thus, we adopt the start time of the flow as 0:00 HST on May 19.

Thickness of F17 flow

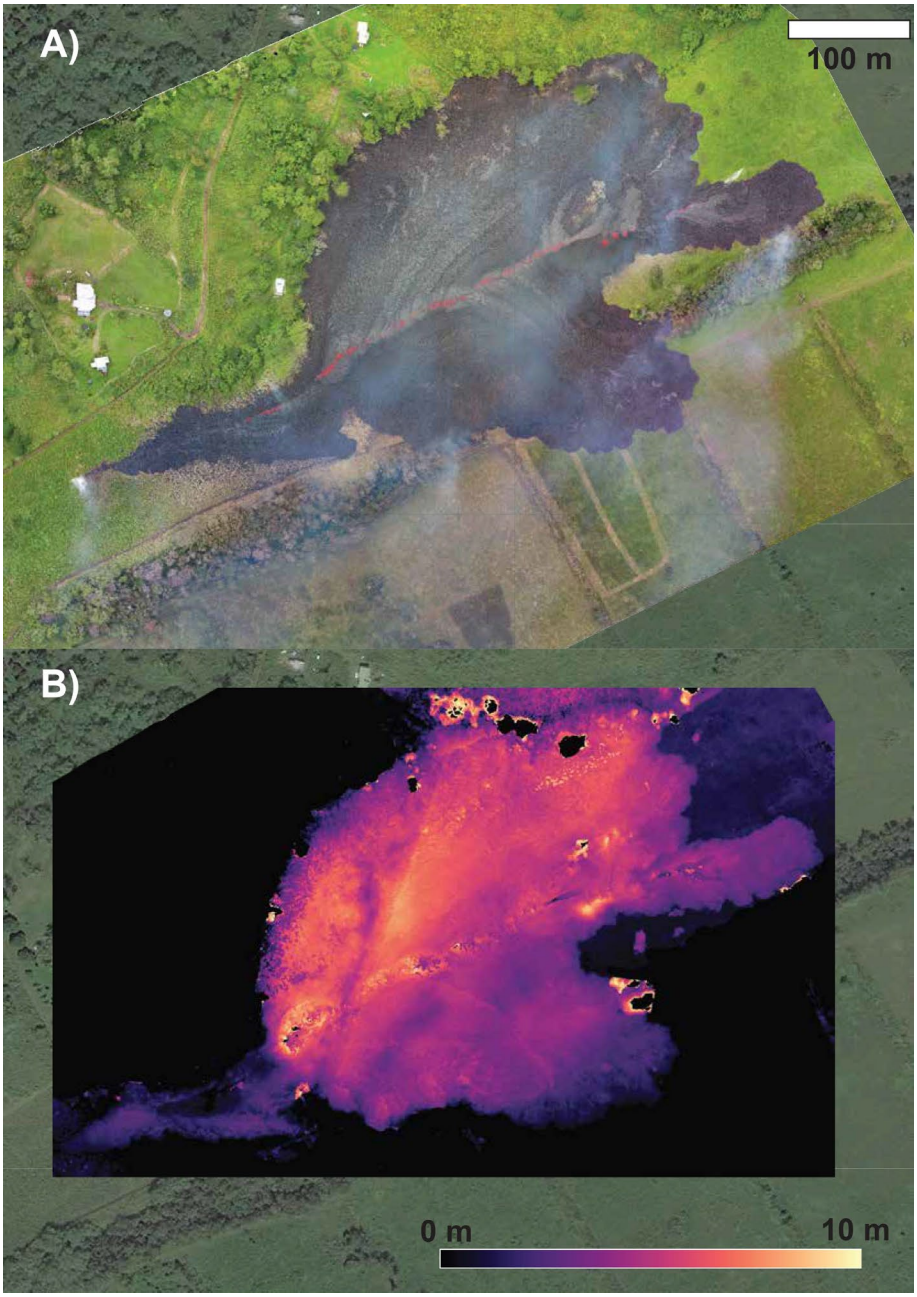

Figure B-S2. Visible light image (A) and corresponding thickness map (B) of the F17 flow at 13:51 HST on May 13th, 2018. Other topographic features in the area have been masked out where possible without obscuring the edges of the flow. Anomalously high points and areas of zero elevation within the margins of the flow correspond to trees.

Drone imagery of the early stages of the F17 flow was used to construct a digital surface model (DSM), following the method of Turner et al. (2017). Lava flow thickness was calculated by subtracting the elevation of the DSM from a DEM of the pre-existing topography (Fig. B-S2).

We use a 1 m resolution DEM constructed from airborne lidar conducted in November 2011, provided to the USGS by Ormat Technologies, Inc.

Variable effusion rate curve construction

Effusion rate measurements were not made in the field for any of the three flows of interest. Thus, our variable effusion rate curves represent only a reasonable possibility based on qualitative observations of differences between the various fissures. An initial key difference between EF8/F17 and F20/22 is the state of lava effusion at calculation initiation. The flows from both EF8 and F17 initiated as soon as lava extruded from the fissures, whereas the flow from F20/22 initiated after a period of sustained activity at the fissure. Therefore, effusion rate started at low values for EF8 and F17, and started at a high value for F20/22. In the same vein, at the conclusion of modeling, both F17 and F20/22 were still erupting lava; thus, effusion rate did not end at zero for either flow. In terms of maximum effusion rate, we assumed that EF8 had the smallest flux as the flow was the smallest, the fissure was the shortest, and the fountain height was the shortest (HVO Staff, 2018). Thus, both F17 and F20/22 should have greater maximum fluxes than EF8. F17 was the longest fissure, thus maximum flux from the entire fissure should be large, though fountain heights rapidly decreased (USGS eruption chronology sheet). Constraints were not placed on the relative magnitude of maximum effusion rate between F17 and F20/22 as their relationship is complex. Although F20/22 produced an exceptionally voluminous flow, not all of the volume fed the flow of interest; our volume flux only fed the flow of interest.

The shape of the effusion rate curves through time were informed by the results of the initial modeling and previously established relationships of effusion rate with time. We assign EF8 and F17 “Wadge-type” effusion rate patterns of linear increase in effusion rate to a

maximum, followed by an exponential decay (Wadge, 1981). All of the variables associated with this type of relationship (slope of linear increase, time of maximum effusion rate, and exponent of exponential decay) were changed iteratively until a qualitatively good fit to the data was achieved. A solution was considered realistic as long as the maximum volume emitted did not exceed the upper limit of estimated flow volume and the previously described relationships between magnitudes of effusion rate were followed. For F20/22, we used an essentially constant effusion rate as it worked well in the initial modeling. However, we incorporated a slight exponential decrease in effusion rate to account for the inflection in the measured data that the constant effusion rate calculations did not emulate. The magnitude of the parameters and the timing of the switch between constant effusion and exponential decrease was determined iteratively until a qualitatively good fit to the data was achieved.

The final equations used to construct the variable effusion rate curves are as follows. For EF8 we use:

$$for\ t = 1\ to\ 54{,}000: Q = 0.000543345t$$

$$for\ t = 54{,}001\ to\ 138{,}600: Q = 29.14e^{-6*10^{-5}*(t-54{,}000)}$$

For F17 we use:

$$for\ t = 1\ to\ 8{,}300: Q = 8$$

$$for\ t = 8{,}301\ to\ 77{,}400: Q = 0.0009501359t$$

$$for\ t = 77{,}401\ to\ 180{,}900: Q = 73.54e^{-2*10^{-5}*(t-77{,}400)}$$

For F20/22 we use:

$$for\ t = 1\ to\ 61{,}200: Q = 55.37$$

$$for\ t = 61{,}201\ to\ 99{,}600: Q = 55.37e^{1*10^{-6}*(t-61{,}200)}$$

In all cases, *t* is time in seconds.

Additional supplementary figures

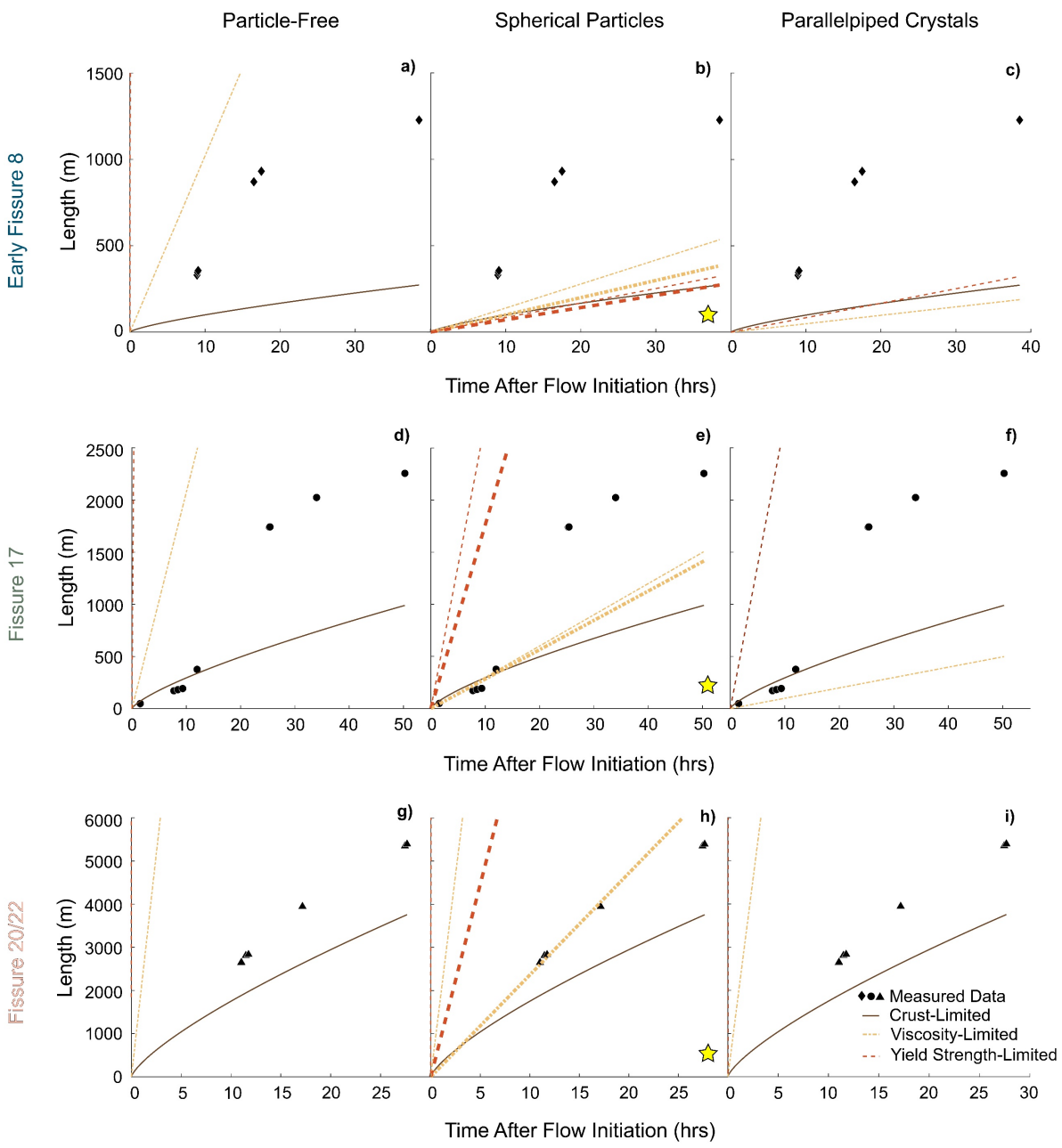

Figure B-S3. All calculation scenario results from the LK equation sets. Thicker lines in the spherical particle scenarios (middle column) indicate calculations that include bubbles. The stars are the sets of calculations that are deemed best fitting for each flow and are also presented in the main text.

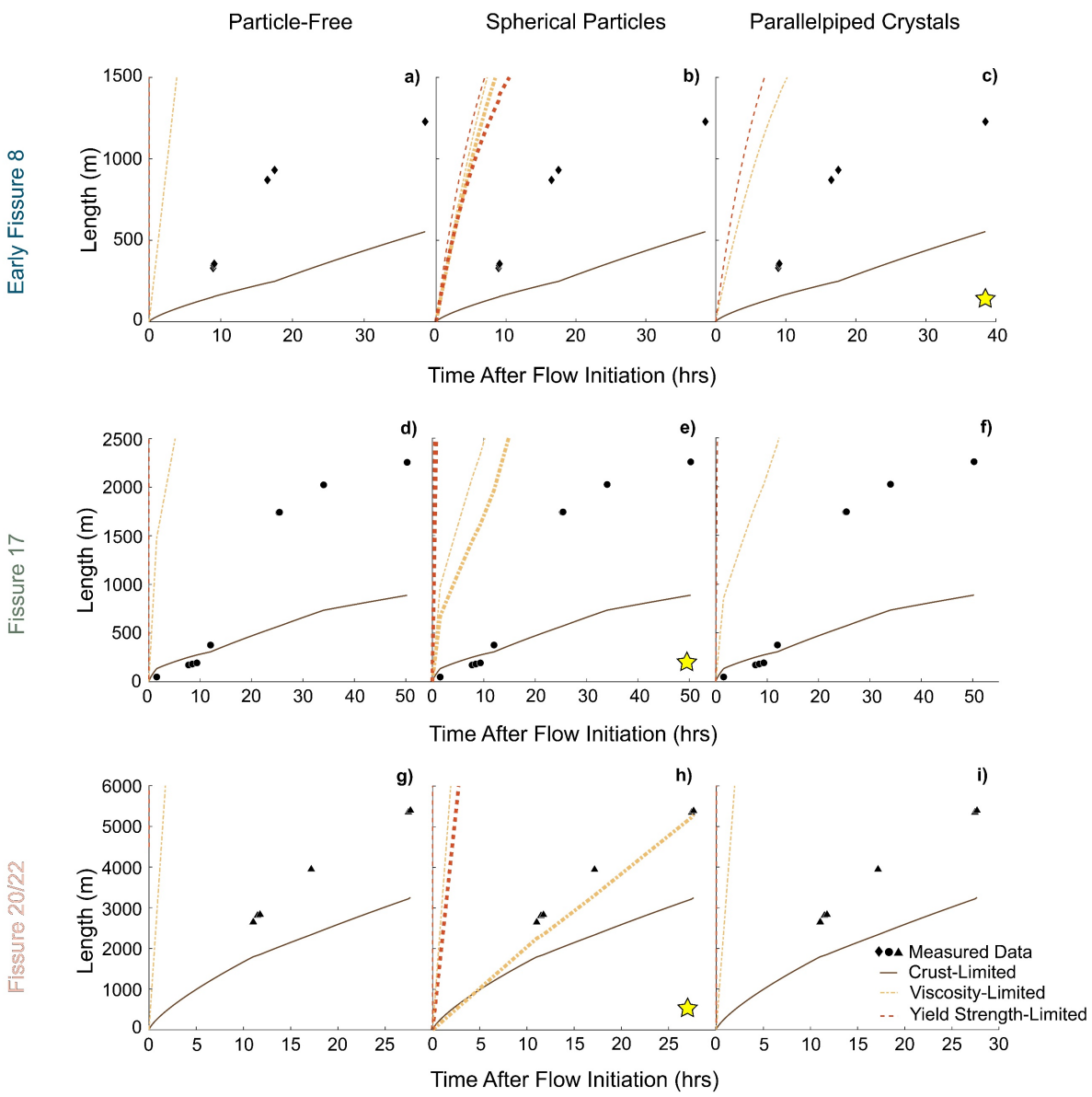

Figure B-S4. All calculation scenario results from the CEA equation sets. Thicker lines in the spherical particle scenarios (middle column) indicate calculations that include bubbles. The stars are the sets of calculations that are deemed best fitting for each flow and are also presented in the main text.

References

Anderson, A. T. (1991). Hourglass inclusions: theory and application to the Bishop Rhyolitic Tuff. *American Mineralogist*, *76*(3-4), 530-547.

Anderson, K. R., & Poland, M. P. (2016). Bayesian estimation of magma supply, storage, and eruption rates using a multiphysical volcano model: Kīlauea Volcano, 2000–2012. *Earth and Planetary Science Letters*, *447*, 161-171.

Anderson, K. R., Johanson, I. A., Patrick, M. R., Gu, M., Segall, P., Poland, M. P., ... & Miklius, A. (2019). Magma reservoir failure and the onset of caldera collapse at Kīlauea Volcano in 2018. *Science*, *366*(6470).

Andrews, B. J. (2014). Magmatic storage conditions, decompression rate, and incipient caldera collapse of the 1902 eruption of Santa Maria Volcano, Guatemala. *Journal of volcanology and geothermal research*, *282*, 103-114.

Bagdassarov, N., Dorfman, A., & Dingwell, D. B. (2000). Effect of alkalis, phosphorus, and water on the surface tension of haplogranite melt. *American Mineralogist*, *85*(1), 33-40.

Barbee, O., Chesner, C., & Deering, C. (2020). Quartz crystals in Toba rhyolites show textures symptomatic of rapid crystallization. *American Mineralogist: Journal of Earth and Planetary Materials*, *105*(2), 194-226.

Barberi, F., Brondi, F., Carapezza, M. L., Cavarra, L., & Murgia, C. (2003). Earthen barriers to control lava flows in the 2001 eruption of Mt. Etna. *Journal of Volcanology and Geothermal Research*, *123*(1-2), 231-243.

Barth, A., Newcombe, M., Plank, T., Gonnermann, H., Hajimirza, S., Soto, G. J., ... & Hauri, E. (2019). Magma decompression rate correlates with explosivity at basaltic volcanoes—Constraints from water diffusion in olivine. *Journal of Volcanology and Geothermal Research*, *387*, 106664.

Beattie, P. (1993). Olivine-melt and orthopyroxene-melt equilibria. *Contributions to Mineralogy and Petrology*, *115*(1), 103-111.

Befus, K. S., & Manga, M. (2019). Supereruption quartz crystals and the hollow reentrants. *Geology*, *47*(8), 710-714.

Bilotta, G., Hérault, A., Cappello, A., Ganci, G., & Del Negro, C. (2016). GPUSPH: a Smoothed Particle Hydrodynamics model for the thermal and rheological evolution of lava flows. *Geological Society, London, Special Publications*, *426*(1), 387-408.

Bonny, E., & Wright, R. (2017). Predicting the end of lava flow-forming eruptions from space. *Bulletin of Volcanology*, *79*(7), 52.

Burgisser, A., Arbaret, L., Martel, C., Forien, M., & Colombier, M. (2020). The role of oxides in the shallow vesiculation of ascending magmas. *Journal of Volcanology and Geothermal Research*, *406*, 107072.

Cáceres, F., Wadsworth, F. B., Scheu, B., Colombier, M., Madonna, C., Cimarelli, C., ... & Dingwell, D. B. (2020). Can nanolites enhance eruption explosivity?. *Geology*.

Cashman, K. V., Kerr, R. C., & Griffiths, R. W. (2006). A laboratory model of surface crust formation and disruption on lava flows through non-uniform channels. *Bulletin of Volcanology*, *68*(7-8), 753-770.

Cashman, K. V., & Rust, A. (2016). Causes and implications of suppressed vesiculation and crystallization in phenocryst embayments. *AGUFM*, *2016*, V13G-02.

Cashman, K. V., & Sparks, R. S. J. (2013). How volcanoes work: A 25 year perspective. *GSA Bulletin*, *125*(5-6), 664-690.

Cashman, K. V., Sparks, R. S. J., & Blundy, J. D. (2017). Vertically extensive and unstable magmatic systems: a unified view of igneous processes. *Science*, *355*(6331).

Cassidy, M., Manga, M., Cashman, K., & Bachmann, O. (2018). Controls on explosive-effusive volcanic eruption styles. *Nature Communications*, *9*(1), 1-16.

Castro, J. M., & Gardner, J. E. (2008). Did magma ascent rate control the explosive-effusive transition at the Inyo volcanic chain, California?. *Geology*, *36*(4), 279-282.

Castruccio, A., Rust, A. C., & Sparks, R. S. J. (2013). Evolution of crust-and core-dominated lava flows using scaling analysis. *Bulletin of Volcanology*, *75*(1), 681.

Castro, J. M., Schipper, C. I., Mueller, S. P., Militzer, A. S., Amigo, A., Parejas, C. S., & Jacob, D. (2013). Storage and eruption of near-liquidus rhyolite magma at Cordón Caulle, Chile. *Bulletin of Volcanology*, *75*(4), 702.

Chakraborty, S. (2008). Diffusion in solid silicates: A tool to track timescales of processes comes of age. *Annu. Rev. Earth Planet. Sci.*, *36*, 153-190.

Cichy, S. B., Botcharnikov, R. E., Holtz, F., & Behrens, H. (2011). Vesiculation and microlite crystallization induced by decompression: A case study of the 1991–1995 Mt Unzen eruption (Japan). *Journal of Petrology*, *52*(7-8), 1469-1492.

Cimarelli, C., Costa, A., Mueller, S., & Mader, H. M. (2011). Rheology of magmas with bimodal crystal size and shape distributions: Insights from analog experiments. *Geochemistry, Geophysics, Geosystems*, *12*(7).

Clarke, A. B., Stephens, S., Teasdale, R., Sparks, R. S. J., & Diller, K. (2007). Petrologic constraints on the decompression history of magma prior to Vulcanian explosions at the Soufrière Hills volcano, Montserrat. *Journal of Volcanology and Geothermal Research*, *161*(4), 261-274.

Cluzel, N., Laporte, D., Provost, A., & Kannewischer, I. (2008). Kinetics of heterogeneous bubble nucleation in rhyolitic melts: implications for the number density of bubbles in volcanic conduits and for pumice textures. *Contributions to Mineralogy and Petrology*, *156*(6), 745-763.

Colombier, M., Wadsworth, F. B., Scheu, B., Vasseur, J., Dobson, K. J., Cáceres, F., ... & Dingwell, D. B. (2020). In situ observation of the percolation threshold in multiphase magma analogues. *Bulletin of volcanology*, *82*(4), 1-15.

Costa, A., Caricchi, L., & Bagdassarov, N. (2009). A model for the rheology of particle-bearing suspensions and partially molten rocks. *Geochemistry, Geophysics, Geosystems*, *10*(3).

Costa, F., Shea, T., & Ubide, T. (2020). Diffusion chronometry and the timescales of magmatic processes. *Nature Reviews Earth & Environment*, 1-14.

Couch, S., Sparks, R. S. J., & Carroll, M. R. (2003). The kinetics of degassing-induced crystallization at Soufriere Hills Volcano, Montserrat. *Journal of Petrology*, *44*(8), 1477-1502.

Crameri, F. (2018), Scientific colour maps. Zenodo. http:// doi.org/10.5281/zenodo.1243862

Crank, J. (1975) The Mathematics of Diffusion, 2nd edition, 414 p. Oxford Science Publication, Oxford.

Crisci, G. M., Rongo, R., Di Gregorio, S., & Spataro, W. (2004). The simulation model SCIARA: the 1991 and 2001 lava flows at Mount Etna. *Journal of Volcanology and Geothermal Research*, *132*(2-3), 253-267.

Crisp, J., & Baloga, S. (1994). Influence of crystallization and entrainment of cooler material on the emplacement of basaltic aa lava flows. *Journal of Geophysical Research: Solid Earth*, *99*(B6), 11819-11831.

De Beni, E., Cantarero, M., & Messina, A. (2019). UAVs for volcano monitoring: A new approach applied on an active lava flow on Mt. Etna (Italy), during the 27 February–02 March 2017 eruption. *Journal of Volcanology and Geothermal Research*, *369*, 250-262.

Di Genova, D., Brooker, R. A., Mader, H. M., Drewitt, J. W., Longo, A., Deubener, J., ... & Miyajima, N. (2020). In situ observation of nanolite growth in volcanic melt: A driving force for explosive eruptions. *Science Advances*, *6*(39), eabb0413.

Di Genova, D., Caracciolo, A., & Kolzenburg, S. (2018). Measuring the degree of "nanotilization" of volcanic glasses: Understanding syn-eruptive processes recorded in melt inclusions. *Lithos*, *318*, 209-218.

deGraffenried, R. L., Larsen, J. F., Graham, N. A., & Cashman, K. V. (2019). The influence of phenocrysts on degassing in crystal-bearing magmas with rhyolitic groundmass melts. *Geophysical Research Letters*, *46*(10), 5127-5136.

Dietterich, H. R., & Cashman, K. V. (2014). Channel networks within lava flows: Formation, evolution, and implications for flow behavior. *Journal of Geophysical Research: Earth Surface*, *119*(8), 1704-1724.

Dietterich, H. R., Cashman, K. V., Rust, A. C., & Lev, E. (2015). Diverting lava flows in the lab. *Nature Geoscience*, *8*(7), 494-496.

Dietterich, H. R., Lev, E., Chen, J., Richardson, J. A., & Cashman, K. V. (2017). Benchmarking computational fluid dynamics models of lava flow simulation for hazard assessment, forecasting, and risk management. *Journal of Applied Volcanology*, *6*(1), 9.

Dietterich, H. R., Diefenbach, A. K., Soule, S. A., Zoeller, M. H., Patrick, M. P., Major, J. J., & Lundgren, P. R. (2021). Lava effusion rate evolution and erupted volume during the 2018 Kīlauea lower East Rift Zone eruption. *Bulletin of Volcanology*, *83*(4), 1-18.

Diller, K., Clarke, A. B., Voight, B., & Neri, A. (2006). Mechanisms of conduit plug formation: Implications for vulcanian explosions. *Geophysical Research Letters*, *33*(20).

Dingwell, D. B. (1996). Volcanic Dilemma--Flow or Blow?. *Science*, *273*(5278), 1054-1055.

Donaldson, C. H. (1979). An experimental investigation of the delay in nucleation of olivine in mafic magmas. *Contributions to Mineralogy and Petrology*, *69*(1), 21-32.

Dragoni, M. (1989). A dynamical model of lava flows cooling by radiation. *Bulletin of Volcanology*, *51*(2), 88-95.

Edmonds, M., Cashman, K. V., Holness, M., & Jackson, M. (2019). Architecture and dynamics of magma reservoirs. *Phil. Trans. R. Soc. A* 377: 20180298.

Favalli, M., Pareschi, M. T., Neri, A., & Isola, I. (2005). Forecasting lava flow paths by a stochastic approach. *Geophysical Research Letters*, *32*(3).

Favalli, M., Tarquini, S., & Fornaciai, A. (2011). DOWNFLOW code and LIDAR technology for lava flow analysis and hazard assessment at Mount Etna. *Annals of Geophysics*, *54*(5).

Ferguson, D. J., Gonnermann, H. M., Ruprecht, P., Plank, T., Hauri, E. H., Houghton, B. F., & Swanson, D. A. (2016). Magma decompression rates during explosive eruptions of Kīlauea volcano, Hawaii, recorded by melt embayments. *Bulletin of Volcanology*, *78*(10), 71.

Fink, J. H., & Griffiths, R. W. (1992). A laboratory analog study of the surface morphology of lava flows extruded from point and line sources. *Journal of Volcanology and Geothermal Research*, *54*(1-2), 19-32.

Fink, J. H., & Zimbelman, J. (1990). Longitudinal variations in rheological properties of lavas: Puu Oo basalt flows, Kilauea Volcano, Hawaii. In *Lava Flows and Domes* (pp. 157-173). Springer, Berlin, Heidelberg.

Gansecki, C., Lee, R. L., Shea, T., Lundblad, S. P., Hon, K., & Parcheta, C. (2019). The tangled tale of Kīlauea's 2018 eruption as told by geochemical monitoring. *Science*, *366*(6470).

Gardner, J. E., Hilton, M., & Carroll, M. R. (1999). Experimental constraints on degassing of magma: isothermal bubble growth during continuous decompression from high pressure. *Earth and Planetary Science Letters*, *168*(1-2), 201-218.

Ghiorso, M. S., & Gualda, G. A. (2015). An H 2 O–CO 2 mixed fluid saturation model compatible with rhyolite-MELTS. *Contributions to Mineralogy and Petrology*, *169*(6), 53.

Giordano, D., Russell, J. K., & Dingwell, D. B. (2008). Viscosity of magmatic liquids: a model. *Earth and Planetary Science Letters*, *271*(1-4), 123-134.

Gonnermann, H. M., & Manga, M. (2007). The fluid mechanics inside a volcano. *Annual Review of Fluid Mechanics*, *39*, 321-356.

Gonnermann, H. M., & Manga, M. (2005). Nonequilibrium magma degassing: results from modeling of the ca. 1340 AD eruption of Mono Craters, California. *Earth and Planetary Science Letters*, *238*(1-2), 1-16.

Griffiths, R. W. (2000). The dynamics of lava flows. *Annual Review of Fluid Mechanics*, *32*(1), 477-518.

Grove, T. L., Donnelly-Nolan, J. M., & Housh, T. (1997). Magmatic processes that generated the rhyolite of Glass Mountain, Medicine Lake volcano, N. California. *Contributions to Mineralogy and Petrology*, *127*(3), 205-223.

Gualda, G. A., Ghiorso, M. S., Lemons, R. V., & Carley, T. L. (2012). Rhyolite-MELTS: a modified calibration of MELTS optimized for silica-rich, fluid-bearing magmatic systems. *Journal of Petrology*, *53*(5), 875-890.

Guest, J. E., Kilburn, C. R. J., Pinkerton, H., & Duncan, A. M. (1987). The evolution of lava flow-fields: observations of the 1981 and 1983 eruptions of Mount Etna, Sicily. *Bulletin of Volcanology*, *49*(3), 527-540.

Hajimirza, S., Gonnermann, H. M., & Gardner, J. E. (2021). Reconciling bubble nucleation in explosive eruptions with geospeedometers. *Nature Communications*, *12*(1), 1-8.

Hamilton, C. W., Glaze, L. S., James, M. R., & Baloga, S. M. (2013). Topographic and stochastic influences on pāhoehoe lava lobe emplacement. *Bulletin of Volcanology*, *75*(11), 756.

Hammer, J. E., Cashman, K. V., Hoblitt, R. P., & Newman, S. (1999). Degassing and microlite crystallization during pre-climactic events of the 1991 eruption of Mt. Pinatubo, Philippines. *Bulletin of Volcanology*, *60*(5), 355-380.

Hammer, J. E., & Rutherford, M. J. (2002). An experimental study of the kinetics of decompression-induced crystallization in silicic melt. *Journal of Geophysical Research: Solid Earth*, *107*(B1), ECV-8.

Harris, A. J. L., Murray, J. B., Aries, S. E., Davies, M. A., Flynn, L. P., Wooster, M. J., ... & Rothery, D. A. (2000). Effusion rate trends at Etna and Krafla and their implications for eruptive mechanisms. *Journal of Volcanology and Geothermal Research*, *102*(3-4), 237-269.

Harris, A. J., Dehn, J., & Calvari, S. (2007). Lava effusion rate definition and measurement: a review. *Bulletin of Volcanology*, *70*(1), 1.

Harris, A. J., & Rowland, S. K. (2015). FLOWGO 2012: an updated framework for thermorheological simulations of channel-contained lava. *Hawaiian Volcanoes: From Source to Surface, Geophysical Monograph Series*, *208*, 457-481.

Harris, A. J. L., Carn, S., Dehn, J., Del Negro, C., Guđmundsson, M. T., Cordonnier, B., ... & Zakšek, K. (2016). Conclusion: recommendations and findings of the RED SEED working group. *Geological Society, London, Special Publications*, *426*(1), 567-648.

Hidaka, M., Goto, A., Umino, S., & Fujita, E. (2005). VTFS project: Development of the lava flow simulation code LavaSIM with a model for three-dimensional convection, spreading, and solidification. *Geochemistry, Geophysics, Geosystems*, *6*(7).

Hirth, J. P., Pound, G. M., & Pierre, G. S. (1970). Bubble nucleation. *Metallurgical Transactions*, *1*(4), 939-945.

Houghton, B. F., Carey, R. J., Cashman, K. V., Wilson, C. J., Hobden, B. J., & Hammer, J. E. (2010). Diverse patterns of ascent, degassing, and eruption of rhyolite magma during the 1.8 ka Taupo eruption, New Zealand: evidence from clast vesicularity. *Journal of Volcanology and Geothermal Research*, *195*(1), 31-47.

Houghton, B. F., Tisdale, C. M., Llewellin, E. W., Taddeucci, J., Orr, T. R., Walker, B. H., & Patrick, M. R. (2021a). The birth of a Hawaiian fissure eruption. *Journal of Geophysical Research: Solid Earth, 126*, e2020JB020903. https://doi.org/10.1029/2020JB020903

Houghton, B. F., Cockshell, W. A., Gregg, C. E., Walker, B. H., Kim, K., Tisdale, C. M., & Yamashita, E. (2021b). Land, lava, and disaster create a social dilemma after the 2018 eruption of Kīlauea volcano. *Nature Communications*, *12*(1), 1-4.

Humphreys, M. C., Menand, T., Blundy, J. D., & Klimm, K. (2008). Magma ascent rates in explosive eruptions: Constraints from H_2O diffusion in melt inclusions. *Earth and Planetary Science Letters*, *270*(1-2), 25-40.

Huppert, H. E. (1982a). Flow and instability of a viscous current down a slope. *Nature*, *300*(5891), 427-429.

Huppert, H. E. (1982b). The propagation of two-dimensional and axisymmetric viscous gravity currents over a rigid horizontal surface. *Journal of Fluid Mechanics*, *121*, 43-58.

Hurwitz, S., & Navon, O. (1994). Bubble nucleation in rhyolitic melts: Experiments at high pressure, temperature, and water content. *Earth and Planetary Science Letters*, *122*(3-4), 267-280.

HVO Staff (2018). Kīlauea Volcano – 2018 Summit and Lower East Rift Zone (LERZ), Brief Overview of Events April 17 to October 5, 2018. https://volcanoes.usgs.gov/vsc/file_mngr/file-179/Chronology%20of%20events%202018.pdf. Accessed 14 April 2021.

Iacono Marziano, G., Schmidt, B. C., & Dolfi, D. (2007). Equilibrium and disequilibrium degassing of a phonolitic melt (Vesuvius AD 79 “white pumice”) simulated by decompression experiments. *Journal of Volcanology and Geothermal Research*, *161*(3), 151-164.

Iacovino, K., & Till, C. B. (2019). DensityX: A program for calculating the densities of magmatic liquids up to 1,627 C and 30 kbar. *Volcanica*, *2*(1), 1-10.

James, M. R., Carr, B., D'Arcy, F., Diefenbach, A., Dietterich, H., Fornaciai, A., ... & Smets, B. (2020). Volcanological applications of unoccupied aircraft systems (UAS): Developments, strategies, and future challenges. *Volcanica*, *3*(1), 67-114.

Kaminski, É., & Jaupart, C. (1997). Expansion and quenching of vesicular magma fragments in Plinian eruptions. *Journal of Geophysical Research: Solid Earth*, *102*(B6), 12187-12203.

Kauahikaua, J., Sherrod, D. R., Cashman, K. V., Heliker, C., Hon, K., Mattox, T. N., & Johnson, J. A. (2003). Hawaiian lava-flow dynamics during the Puu Oo-Kupaianaha eruption: A tale of two decades. *The Puu Oo-Kupaianaha Eruption of Kilauea Volcano, Hawaii, the First 20*, 63-87.

Kelfoun, K., & Vargas, S. V. (2016). VolcFlow capabilities and potential development for the simulation of lava flows. *Geological Society, London, Special Publications*, *426*(1), 337-343.

Kerr, R. C., Griffiths, R. W., & Cashman, K. V. (2006). Formation of channelized lava flows on an unconfined slope. *Journal of Geophysical Research: Solid Earth*, *111*(B10).

Kerr, R. C., & Lyman, A. W. (2007). Importance of surface crust strength during the flow of the 1988–1990 andesite lava of Lonquimay Volcano, Chile. *Journal of Geophysical Research: Solid Earth*, *112*(B3).

Klug, C., & Cashman, K. V. (1994). Vesiculation of May 18, 1980, Mount St. Helens magma. *Geology*, *22*(5), 468-472.

Komorowski, J.-C., Tedesco, D., Kasereka, M., Allard, P., Papale, P.,…& Wafula, M. (2002). The January 2002 flank eruption of Nyiragongo Volcano (Democratic Republic of Congo): chronology, evidence for a tectonic rift trigger, and impact of lava flows on the city of Goma. *Acta Vulcanologica 14*(1-2), 27-62.

Krimer, D., & Costa, F. (2017). Evaluation of the effects of 3D diffusion, crystal geometry, and initial conditions on retrieved time-scales from Fe–Mg zoning in natural oriented orthopyroxene crystals. *Geochimica et Cosmochimica Acta*, *196*, 271-288.

Larsen, J. F., & Gardner, J. E. (2000). Experimental constraints on bubble interactions in rhyolite melts: implications for vesicle size distributions. *Earth and Planetary Science Letters*, *180*(1-2), 201-214.

Le Gall, N., & Pichavant, M. (2016a). Experimental simulation of bubble nucleation and magma ascent in basaltic systems: Implications for Stromboli volcano. *American Mineralogist*, *101*(9), 1967-1985.

Le Gall, N., & Pichavant, M. (2016b). Homogeneous bubble nucleation in H_2O-and H_2O-CO_2-bearing basaltic melts: results of high temperature decompression experiments. *Journal of Volcanology and Geothermal Research*, *327*, 604-621.

Le Losq, C., Neuville, D. R., Moretti, R., & Roux, J. (2012). Determination of water content in silicate glasses using Raman spectrometry: Implications for the study of explosive volcanism. *American Mineralogist*, *97*(5-6), 779-790.

Leonhardi, T. C., Hammer, J. E., & First, E. (2015, December). Effect of Superheating on Olivine Nucleation and Growth in a Silica-Undersaturated Melt: An Experimental Study. In *AGU Abstract V41B-3071, Fall Meeting*.

Lindoo, A., Larsen, J. F., Cashman, K. V., & Oppenheimer, J. (2017). Crystal controls on permeability development and degassing in basaltic andesite magma. *Geology*, *45*(9), 831-834.

Lister, J. R. (1992). Viscous flows down an inclined plane from point and line sources. *Journal of Fluid Mechanics*, *242*, 631-653.

Liu, Y., Anderson, A. T., & Wilson, C. J. (2007). Melt pockets in phenocrysts and decompression rates of silicic magmas before fragmentation. *Journal of Geophysical Research: Solid Earth*, *112*(B6).

Liu, Y., Zhang, Y., & Behrens, H. (2005). Solubility of H_2O in rhyolitic melts at low pressures and a new empirical model for mixed H_2O–CO_2 solubility in rhyolitic melts. *Journal of Volcanology and Geothermal Research*, *143*(1-3), 219-235.

Lloyd, A. S., Ruprecht, P., Hauri, E. H., Rose, W., Gonnermann, H. M., & Plank, T. (2014). NanoSIMS results from olivine-hosted melt embayments: magma ascent rate during explosive basaltic eruptions. *Journal of Volcanology and Geothermal Research*, *283*, 1-18.

Lockwood, J. P., & Torgerson, F. A. (1980). Diversion of lava flows by aerial bombing—lessons from Mauna Loa volcano, Hawaii. *Bulletin Volcanologique*, *43*(4), 727-741.

Loewen, M. W., Bindeman, I. N., & Melnik, O. E. (2017). Eruption mechanisms and short duration of large rhyolitic lava flows of Yellowstone. *Earth and Planetary Science Letters*, *458*, 80-91.

Lyman, A. W., & Kerr, R. C. (2006). Effect of surface solidification on the emplacement of lava flows on a slope. *Journal of Geophysical Research: Solid Earth*, *111*(B5).

Mader, H. M., Llewellin, E. W., & Mueller, S. P. (2013). The rheology of two-phase magmas: A review and analysis. *Journal of Volcanology and Geothermal Research*, *257*, 135-158.

Manga, M., Castro, J., Cashman, K. V., & Loewenberg, M. (1998). Rheology of bubble-bearing magmas. *Journal of Volcanology and Geothermal Research*, *87*(1-4), 15-28.

Mangan, M., & Sisson, T. (2000). Delayed, disequilibrium degassing in rhyolite magma: decompression experiments and implications for explosive volcanism. *Earth and Planetary Science Letters*, *183*(3-4), 441-455.

Mangan, M. T., Sisson, T. W., & Hankins, W. B. (2004). Decompression experiments identify kinetic controls on explosive silicic eruptions. *Geophysical Research Letters*, *31*(8).

Mastin, L. G., & Ghiorso, M. S. (2001). Adiabatic temperature changes of magma–gas mixtures during ascent and eruption. *Contributions to Mineralogy and Petrology*, *141*(3), 307-321.

McCartney, K., Hammer, J. E., Shea, T., Giachetti, T., & Brachfeld, S. A. (2020). Nanometer scale titanomagnetite assisted bubble nucleation: a joint magnetic and textural characterization approach. *AGUFM*, *2020*, V003-0008.

Moore, G., Vennemann, T., & Carmichael, I. S. E. (1998). An empirical model for the solubility of H 2 O in magmas to 3 kilobars. *american Mineralogist*, *83*(1-2), 36-42.

Mourtada-Bonnefoi, C. C., & Laporte, D. (1999). Experimental study of homogeneous bubble nucleation in rhyolitic magmas. *Geophysical Research Letters*, *26*(23), 3505-3508.

Mourtada-Bonnefoi, C. C., & Laporte, D. (2002). Homogeneous bubble nucleation in rhyolitic magmas: an experimental study of the effect of H_2O and CO_2. *Journal of Geophysical Research: Solid Earth*, *107*(B4), ECV-2.

Mourtada-Bonnefoi, C. C., & Laporte, D. (2004). Kinetics of bubble nucleation in a rhyolitic melt: an experimental study of the effect of ascent rate. *Earth and Planetary Science Letters*, *218*(3-4), 521-537.

Myers, M. L., Druitt, T. H., Schiavi, F., Gurioli, L., & Flaherty, T. (2021). Evolution of magma decompression and discharge during a Plinian event (Late Bronze-Age eruption, Santorini) from multiple eruption-intensity proxies. *Bulletin of Volcanology*, *83*(3), 1-17.

Myers, M. L., Wallace, P. J., Wilson, C. J., Morter, B. K., & Swallow, E. J. (2016). Prolonged ascent and episodic venting of discrete magma batches at the onset of the Huckleberry Ridge supereruption, Yellowstone. *Earth and Planetary Science Letters*, *451*, 285-297.

Myers, M. L., Wallace, P. J., Wilson, C. J., Watkins, J. M., & Liu, Y. (2018). Ascent rates of rhyolitic magma at the onset of three caldera-forming eruptions. *American Mineralogist*, *103*(6), 952-965.

Myers, M. L., Wallace, P. J., & Wilson, C. J. (2019). Inferring magma ascent timescales and reconstructing conduit processes in explosive rhyolitic eruptions using diffusive losses of hydrogen from melt inclusions. *Journal of Volcanology and Geothermal Research*, *369*, 95-112.

Mueller, S., Llewellin, E. W., & Mader, H. M. (2011). The effect of particle shape on suspension viscosity and implications for magmatic flows. *Geophysical Research Letters*, *38*(13).

Muir, D. D., Blundy, J. D., & Rust, A. C. (2012). Multiphase petrography of volcanic rocks using element maps: a method applied to Mount St. Helens, 1980–2005. *Bulletin of Volcanology*, *74*(5), 1101-1120.

Neal, C. A., Brantley, S. R., Antolik, L., Babb, J. L., Burgess, M., Calles, K., ... & Dotray, P. (2019). The 2018 rift eruption and summit collapse of Kīlauea Volcano. *Science*, *363*(6425), 367-374.

Newcombe, M. E., Plank, T., Barth, A., Asimow, P., & Hauri, E. (2020a). Water-in-olivine magma ascent chronometry: Every crystal is a clock. *Journal of Volcanology and Geothermal Research*, 106872.

Newcombe, M. E., Plank, T. A., Zhang, Y., Holycross, M., Barth, A., Lloyd, A. S., ... & Hauri, E. (2020b). Magma Pressure-Temperature-time paths during mafic explosive eruptions. *Frontiers in Earth Science*.

Ni, H., & Zhang, Y. (2008). H_2O diffusion models in rhyolitic melt with new high pressure data. *Chemical Geology*, *250*(1-4), 68-78.

Nicholis, M. G., & Rutherford, M. J. (2004). Experimental constraints on magma ascent rate for the Crater Flat volcanic zone hawaiite. *Geology*, *32*(6), 489-492.

Okumura, S., Nakamura, M., & Tsuchiyama, A. (2006). Shear-induced bubble coalescence in rhyolitic melts with low vesicularity. *Geophysical Research Letters*, *33*(20).

Okumura, S., Nakamura, M., Tsuchiyama, A., Nakano, T., & Uesugi, K. (2008). Evolution of bubble microstructure in sheared rhyolite: Formation of a channel-like bubble network. *Journal of Geophysical Research: Solid Earth*, *113*(B7).

Papale, P., & Dobran, F. (1993). Modeling of the ascent of magma during the plinian eruption of Vesuvius in AD 79. *Journal of volcanology and geothermal research*, *58*(1-4), 101-132.

Papale, P., Neri, A., & Macedonio, G. (1998). The role of magma composition and water content in explosive eruptions: 1. Conduit ascent dynamics. *Journal of Volcanology and Geothermal Research*, *87*(1-4), 75-93.

Patrick, M. R., Houghton, B. F., Anderson, K. R., Poland, M. P., Montgomery-Brown, E., Johanson, I., ... & Elias, T. (2020). The cascading origin of the 2018 Kīlauea eruption and implications for future forecasting. *Nature Communications*, *11*(1), 1-13.

Patrick, M. R., Dietterich, H. R., Lyons, J. J., Diefenbach, A. K., Parcheta, C., Anderson, K. R., ... & Kauahikaua, J. P. (2019). Cyclic lava effusion during the 2018 eruption of Kīlauea Volcano. *Science*, *366*(6470).

Patrick, M., Orr, T., Fisher, G., Trusdell, F., & Kauahikaua, J. (2017). Thermal mapping of a pāhoehoe lava flow, Kīlauea Volcano. *Journal of Volcanology and Geothermal Research*, *332*, 71-87.

Pinkerton, H., & Stevenson, R. J. (1992). Methods of determining the rheological properties of magmas at sub-liquidus temperatures. *Journal of Volcanology and Geothermal Research*, *53*(1-4), 47-66.

Pistone, M., Caricchi, L., Ulmer, P., Burlini, L., Ardia, P., Reusser, E., ... & Arbaret, L. (2012). Deformation experiments of bubble-and crystal-bearing magmas: Rheological and microstructural analysis. *Journal of Geophysical Research: Solid Earth*, *117*(B5).

Preuss, O., Marxer, H., Ulmer, S., Wolf, J., & Nowak, M. (2016). Degassing of hydrous trachytic Campi Flegrei and phonolitic Vesuvius melts: Experimental limitations and chances to study homogeneous bubble nucleation. *American Mineralogist*, *101*(4), 859-875.

Pupier, E., Duchene, S., & Toplis, M. J. (2008). Experimental quantification of plagioclase crystal size distribution during cooling of a basaltic liquid. *Contributions to Mineralogy and Petrology*, *155*(5), 555-570.

Richardson, P., & Karlstrom, L. (2019). The multi-scale influence of topography on lava flow morphology. *Bulletin of Volcanology*, *81*(4), 1-17.

Robert, B., Harris, A., Gurioli, L., Médard, E., Sehlke, A., & Whittington, A. (2014). Textural and rheological evolution of basalt flowing down a lava channel. *Bulletin of Volcanology*, *76*(6), 824.

Roman, D. C., Soldati, A., Dingwell, D. B., Houghton, B. F., & Shiro, B. R. (2021). Earthquakes indicated magma viscosity during Kīlauea's 2018 eruption. *Nature, 592,* 237-241.

Rowland, S. K., Garbeil, H., & Harris, A. J. (2005). Lengths and hazards from channel-fed lava flows on Mauna Loa, Hawai 'i, determined from thermal and downslope modeling with FLOWGO. *Bulletin of Volcanology*, *67*(7), 634-647.

Rowland, S. K., & Walker, G. P. (1990). Pahoehoe and aa in Hawaii: volumetric flow rate controls the lava structure. *Bulletin of Volcanology*, *52*(8), 615-628.

Rumpf, M. E., Lev, E., & Wysocki, R. (2018). The influence of topographic roughness on lava flow emplacement. *Bulletin of Volcanology*, *80*(7), 63.

Rust, A. C., & Manga, M. (2002). Effects of bubble deformation on the viscosity of dilute suspensions. *Journal of non-newtonian fluid mechanics*, *104*(1), 53-63.

Rutherford, M. J. (2008). Magma ascent rates. *Reviews in Mineralogy and Geochemistry*, *69*(1), 241-271.

Rutherford, M. J., & Devine, J. D. (2003). Magmatic conditions and magma ascent as indicated by hornblende phase equilibria and reactions in the 1995–2002 Soufriere Hills magma. *Journal of Petrology*, *44*(8), 1433-1453.

Rutherford, M. J., & Hill, P. M. (1993). Magma ascent rates from amphibole breakdown: an experimental study applied to the 1980–1986 Mount St. Helens eruptions. *Journal of Geophysical Research: Solid Earth*, *98*(B11), 19667-19685.

Sable, J. E., Houghton, B. F., Del Carlo, P., & Coltelli, M. (2006). Changing conditions of magma ascent and fragmentation during the Etna 122 BC basaltic Plinian eruption: Evidence from clast microtextures. *Journal of Volcanology and Geothermal Research*, *158*(3-4), 333-354.

Sato, H. (1995). Textural difference between pahoehoe and aa lavas of Izu-Oshima volcano, Japan—an experimental study on population density of plagioclase. *Journal of Volcanology and Geothermal Research*, *66*(1-4), 101-113.

Seaman, C., Sherman, S. B., Garcia, M. O., Baker, M. B., Balta, B., & Stolper, E. (2004). Volatiles in glasses from the HSDP2 drill core. *Geochemistry, Geophysics, Geosystems*, *5*(9).

Shea, T. (2017). Bubble nucleation in magmas: a dominantly heterogeneous process?. *Journal of Volcanology and Geothermal Research*, *343*, 155-170.

Shea, T., Costa, F., Krimer, D., & Hammer, J. E. (2015). Accuracy of timescales retrieved from diffusion modeling in olivine: A 3D perspective. *American Mineralogist*, *100*(10), 2026-2042.

Shea, T., Hellebrand, E., Gurioli, L., & Tuffen, H. (2014). Conduit-to localized-scale degassing during Plinian eruptions: Insights from major element and volatile (Cl and H_2O) analyses within Vesuvius AD 79 pumice. *Journal of Petrology*, *55*(2), 315-344.

Shea, T., Houghton, B. F., Gurioli, L., Cashman, K. V., Hammer, J. E., & Hobden, B. J. (2010). Textural studies of vesicles in volcanic rocks: an integrated methodology. *Journal of Volcanology and Geothermal Research*, *190*(3-4), 271-289.

Soldati, A., Houghton, B. F., & Dingwell, D. B. (2021). Subliquidus rheology of basalt from the 2018 Lower East Rift Zone Kilauea eruption: isothermal vs. dynamic expression. *Chemical Geology*, 120363.

Soldati, A., Farrell, J. A., Sant, C., Wysocki, R., & Karson, J. A. (2020). The effect of bubbles on the rheology of basaltic lava flows: Insights from large-scale two-phase experiments. *Earth and Planetary Science Letters*, *548*, 116504.

Su, Y., & Huber, C. (2017). The effect of nonlinear decompression history on H_2O/CO_2 vesiculation in rhyolitic magmas. *Journal of Geophysical Research: Solid Earth*, *122*(4), 2712-2723.

Szramek, L. A. (2016). Mafic Plinian eruptions: Is fast ascent required?. *Journal of Geophysical Research: Solid Earth*, *121*(10), 7119-7136.

Takagi, D., & Huppert, H. E. (2010). Initial advance of long lava flows in open channels. *Journal of Volcanology and Geothermal Research*, *195*(2-4), 121-126.

Tarquini, S., & de' Michieli Vitturi, M. (2014). Influence of fluctuating supply on the emplacement dynamics of channelized lava flows. *Bulletin of Volcanology*, *76*(3), 1-13.

Toramaru, A. (1989). Vesiculation process and bubble size distributions in ascending magmas with constant velocities. *Journal of Geophysical Research: Solid Earth*, *94*(B12), 17523-17542.

Toramaru, A. (1995). Numerical study of nucleation and growth of bubbles in viscous magmas. *Journal of Geophysical Research: Solid Earth*, *100*(B2), 1913-1931.

Toramaru, A. (2006). BND (bubble number density) decompression rate meter for explosive volcanic eruptions. *Journal of Volcanology and Geothermal Research*, *154*(3-4), 303-316.

Toramaru, A., Noguchi, S., Oyoshihara, S., & Tsune, A. (2008). MND (microlite number density) water exsolution rate meter. *Journal of Volcanology and Geothermal Research*, *175*(1-2), 156-167.

Turner, N. R., Perroy, R. L., & Hon, K. (2017). Lava flow hazard prediction and monitoring with UAS: a case study from the 2014–2015 Pāhoa lava flow crisis, Hawai 'i. *Journal of Applied Volcanology*, *6*(1), 1-11.

Vicari, A., Alexis, H., Del Negro, C., Coltelli, M., Marsella, M., & Proietti, C. (2007). Modeling of the 2001 lava flow at Etna volcano by a cellular automata approach. *Environmental Modelling & Software*, *22*(10), 1465-1471.

Wadge, G. (1981). The variation of magma discharge during basaltic eruptions. *Journal of Volcanology and Geothermal Research*, *11*(2-4), 139-168.

Walker, G. P. L., Huntingdon, A. T., Sanders, A. T., & Dinsdale, J. L. (1973). Lengths of lava flows. *Philosophical Transactions of the Royal Society of London. Series A, Mathematical and Physical Sciences*, *274*(1238), 107-118.

Walker, D., Powell, M. A., Lofgren, G. E., & Hays, J. F. (1978). Dynamic crystallization of a eucrite basalt. In *Proceedings of the Ninth Lunar and Planetary Science Conference, Houston, Texas, March 13-17, 1978*. Pergamon Press.

Webb, S. L., & Dingwell, D. B. (1990). The onset of non-Newtonian rheology of silicate melts. *Physics and Chemistry of Minerals*, *17*(2), 125-132.

Williams, R.S., Moore, J.G., 1983. Man against the volcano: The eruption of Heimaey, Vestmannaeyjar, Iceland. U.S. Geological Survey Publication.

Zhang, Y., Ni, H., & Chen, Y. (2010). Diffusion data in silicate melts. *Reviews in Mineralogy and Geochemistry*, *72*(1), 311-408.

Zoeller, M. H., Patrick, M. R., & Neal, C. A. (2018). Crisis remote sensing during the 2018 lower East Rift Zone eruption of Kīlauea Volcano. *Photogrammetric Engineering & Remote Sensing*, *84*(12), 749-751.